Measurements of Λ, $\overline{\Lambda}$ and K^0_S from Pb-Pb Collisions at 158 GeV per nucleon in a Large Acceptance Experiment.

Lee Stuart Barnby

Submitted for the Degree of Doctor of Philosophy

The School of Physics and Astronomy,
Faculty of Science,
The University of Birmingham,
June 1999

Synopsis

The main reason for studying relativistic heavy-ion collisions is to discover the phase transition from nuclear matter to the Quark-Gluon Plasma. Such a transition is predicted to occur under conditions of high temperature and density. The predicted state features deconfined quarks and gluons as the relevant degrees of freedom instead of colour-singlet hadrons. These new degrees of freedom should lead to an enhanced production of strange quarks which has directly observable consequences on the composition of the final state hadrons detected in such a collision.

The NA49 experiment is able to measure hadronic production in central Pb+Pb collisions. It uses a Pb beam, of energy 158 GeV per nucleon, from the CERN SPS with a fixed Pb target. The experiment features four large tracking detectors which can measure the trajectories of charged particles.

In this thesis the method of reconstructing neutral strange particles, Λ,$\overline{\Lambda}$ and K^0_S from their charged decay products is described. The procedure for correcting the raw yields for losses due to the limited experimental acceptance and efficiency in reconstruction is explained. An estimate of some systematic errors is made. The resulting rapidity distributions, which span either side of mid-rapidity are peaked (with the possible exception of Λ) and the transverse momentum spectra fit the Hagedorn distribution. The inverse slope parameters, $T_\Lambda = 274 \pm 5$ MeV, $T_{\overline{\Lambda}} = 279 \pm 10$ MeV and $T_K = 238 \pm 5$ MeV are consistent with the picture of transverse flow observed in these collisions. These results are compared with other measurements.

Author's Contribution

The experiment which collected the data presented in this thesis is large and complex. The recording and analysis of data is necessarily a collaborative effort. As a member the NA49 Collaboration the author has participated in the running periods of the experiment during which data were collected. The author has contributed towards the development of the data analysis by testing and debugging new reconstruction software which was used in a re-designed scheme that best makes use of the multiple detectors in the experiment. There was a particular emphasis on the ability of the software to reconstruct Λ, $\overline{\Lambda}$ and K^0_S. The author has been responsible for the maintenance of the particular program module that reconstructs these particle decays and ensured its correct operation with the new p-Pb and p-p collision datasets.

The author has made substantial modifications to the software controlling the reconstruction programs so that the large volumes of data necessary for the calculation of corrections to the raw yields could be processed. This involved installing software onto a computer farm and interfacing the existing control software to the new software. Fully corrected yields of Λ, $\overline{\Lambda}$ and K^0_S have been extracted making use of these adaptations. The data presented in this thesis are an original analysis of Pb-Pb collision data which is the first to be attempted using the new reconstruction scheme and the consequent increase in the acceptance to cover both sides of mid-rapidity.

Acknowledgments

I would like to thank Professor John Nelson for affording me the opportunity to work in the Nuclear Physics Group here at the University of Birmingham and most importantly for acting as my supervisor throughout my Ph.D. The Engineering and Physical Sciences Research Council has provided me with a Studentship for three years for which I am also grateful.

During the course of my studies I have received help from many people and I would like to take this opportunity to thank them all collectively. In particular, I would like to thank Dr Peter Jones for the help and advice he has given me and for always having the time to discuss whatever it was that I was working on at the time. I also acknowledge all the members of the NA49 Collaboration, past and present, without whom there would be no experiment and no thesis. I am indebted to Dr Predrag Buncic for all his hard work in running the production of data at CERN and for his patience in answering my sometimes strange questions on the workings of the computers at CERN. Many thanks also go to those members of the Collaboration who made my times at CERN more interesting and enjoyable, especially those of you who showed me some of the “cheaper” bars in Geneva (you know who you are).

I am very appreciative of the work done by Jim Campbell in maintaining the computer systems upon which I relied heavily and his advice on many computing matters, even if I did not always follow it. I thank all the members of the Group for helping to provide a friendly atmosphere.

I have been fortunate enough to share an office with many people over the course of my time here and without them it would have been lonely work. I would like to thank all of you who were here at the start and welcomed me to Birmingham; Lachlan, Helen, Alex, Sam, Emma, Dave and last but not least Tim who managed to stay here longer than anyone and provided the most entertainment. I am grateful for the friendship of Colin and Dave who have been with me all the way along this long road and to those of you who remain; Matt, Rob, Peter and Richard. Thanks also to Steve for never refusing to go the bar and for being, probably, Birmingham's most generous landlord. I have also enjoyed the friendship (i.e. trips to the pubs in Moseley) of the many postgrads I met in the three years that I lived at Park Road.

I am very grateful indeed to my parents for all of their support throughout my times at University in Manchester and Birmingham. They have always taken an interest in my work and supported and encouraged me all along the way.

Finally, my girlfriend Helen, whom I met during my time in Birmingham, has recently had to put up with me during the time I have spent writing-up but she has usually managed to cheer me up for which I am very grateful. She has been my best friend and I love her very much.

Contents

List of Figures

List of Tables

Chapter 1

Introduction to Relativistic Heavy-ion collisions

The main motivation for the study of relativistic heavy-ion collisions is to probe nuclear matter under extreme conditions of temperature and density. Experiments are performed with the hope of creating an entirely new form of matter and observing it in the laboratory. This new form of matter is the Quark-Gluon Plasma (QGP), which according to predictions, will be created by combinations of high temperatures and densities. The QGP is the nuclear matter analogue of the plasma phase in ordinary atomic matter. In the QGP the quarks, which are the constituents of the nucleon, are no longer confined to the nucleon and exist as bulk quark matter. Experiments have been and are being performed at a range of energies in order to sample several different points on the phase diagram for strongly interacting matter and hopefully locate the phase transition between the quark and hadronic matter phases. It is believed that this transition must have occurred in the early universe. Phase transitions are many body effects and symmetries are restored on the higher temperature side of the transi-

Symbol	Name	Mass	Charge	Quantum no.
u	up	300 MeV	$+\frac{2}{3}$	$I_3 = +\frac{1}{2}$
d	down	300 MeV	$-\frac{2}{3}$	$I_3 = -\frac{1}{2}$
s	strange	500 MeV	$-\frac{2}{3}$	S=-1
c	charm	1.2 GeV	$+\frac{2}{3}$	C=+1
b	bottom	4.2 GeV	$-\frac{2}{3}$	B=-1
t	top	170 GeV	$+\frac{2}{3}$	T=+1

Table 1.1: The six quark flavours and their approximate constituent masses.

tion. For these reasons it is interesting to investigate QGP formation. This first chapter serves to introduce some of the concepts and terms used in the study of heavy-ion collisions and the QGP and review the signatures which may reveal its existence.

1.1 The Quark Model

The quark model describes nucleons and other hadrons as consisting of quarks. Baryons, of which the nucleons are two examples, are made up of three quarks whereas mesons, such as pions, consist of a quark and an anti-quark. All hadrons, particles which are affected by the strong force, are thought to be combinations of three quarks, three anti-quarks or a quark with an anti-quark. The hadron spectrum can be accounted for by six flavours of quarks, which are listed in table 1.1 with their quantum numbers. The two most massive quark flavours do not feature in heavy-ion collisions, at the energies presently available, due to their high masses.

Quarks are created in quark-anti-quark pairs of the same flavour. Flavour is conserved in the strong interaction but not in weak decays which occur on a much longer time-scale. Some mesons and baryons with their quark content are shown in figures 1.1 & 1.2.

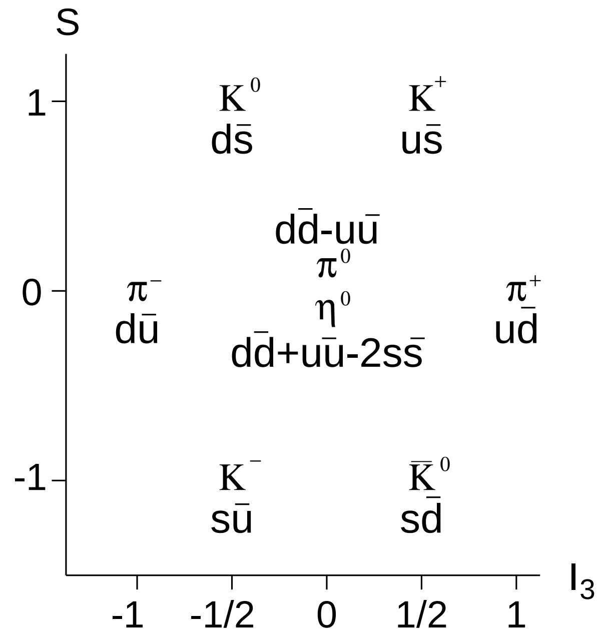

Figure 1.1: Meson octet with $J^P = 0^-$

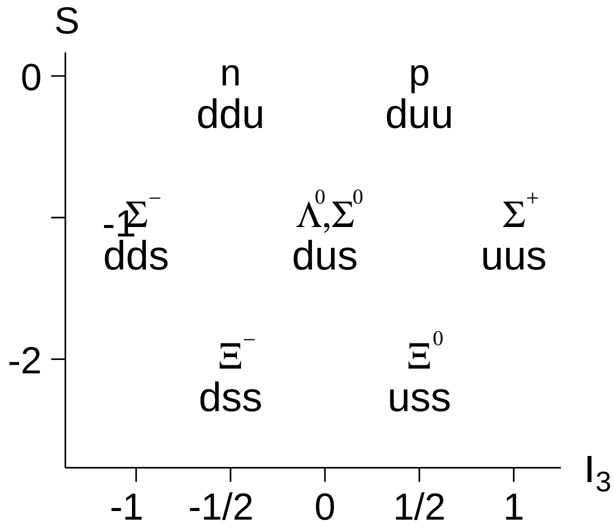

Figure 1.2: Baryon octet with $J^P = \frac{1}{2}^+$.

Even after taking into account the spin of the quarks it would appear that some hadronic states, such as the Δ^{++}, violate the Pauli exclusion principle. This resonance consists of three u quarks and has a spin of $\frac{3}{2}$ so all three quarks appear to be in identical quantum states. This leads to the introduction of a further quantum number which can take on three values for quarks (plus three opposite values for anti-quarks). This quantum number is labelled colour and the values have become known as red, green and blue. Thus, in the Δ^{++} resonance the three u quarks each have a different colour quantum number. The complete Standard Model also includes the leptons and the bosons which mediate the forces. One of these is the gluon which is exchanged in the strong interaction just as electromagnetic interactions exchange photons. However, unlike the photon, the gluon carries the quanta of the force it is mediating. That is to say gluons have colour charge whereas photons do not possess electromagnetic charge. This property means that the gluons can interact amongst themselves leading to qualitative differences between the strong and electromagnetic forces. There are in fact an octet of gluons carrying the different combinations of the colour charge, $r\bar{b}, r\bar{g}, b\bar{g}, b\bar{r}, g\bar{b}, g\bar{r}$ and the mixtures $(r\bar{r} - g\bar{g})/\sqrt{2}$, and $(r\bar{r} + g\bar{g} - 2b\bar{b})/\sqrt{6}$. This scheme allows a quark of any colour to interact with another by exchanging the appropriate gluon.

1.2 The Strong Interaction

A description of the interaction between quarks and gluons is provided by Quantum Chromodynamics (QCD). It is from the study of QCD that the interesting and novel features of strongly interacting matter are predicted. The strong interaction is in fact rather weak at short space-time intervals, or equivalently large momentum transfers, because the coupling "constant" decreases logarithmically. This property is called *asymptotic freedom*. At large distances, which in this case means distances larger than the order of 1 fm, the effective coupling becomes larger which leads to the phenomena of chiral symmetry breaking and *confinement*.

Quark confinement is modelled by the MIT Bag Model [1]. In this model the confinement results from the vacuum which provides a pressure to contain the quarks inside the hadron. Consequently the vacuum must have a non-zero energy density, ϵ, since for an ideal gas $P = \frac{1}{3}\epsilon$ where P is the pressure. Alternatively, one can look at this phenomenon from the point of view of energy required to separate two quarks. This energy increases linearly with the distance between the quarks so that an infinite amount of energy is required for full separation. However, if enough energy is put into separating them then this energy is used to create a new $q\bar{q}$ pair. The result is again quark confinement. Asymptotic freedom may be understood by two simple qualitative pictures. Firstly, a quark with a colour charge has its charge screened due to the polarization of the virtual quarks and gluons near it, which results in the reduction in the strength of the interaction between the quark and a nearby test colour charge. Secondly, at high densities the hadrons must begin to overlap and lose their distinct identities. Since on the one hand quarks are confined to hadrons but on the other they can be quasi-free these represent two distinct phases and it is to be expected that there must be some transition between them.

Analytical calculations of the properties of QCD are only possible in the high momentum transfer (Q^2) case where it is possible to utilize the methods of perturbation theory to obtain quantitive results. This approach is certainly not applicable to the energies available to current heavy-ion experiments although it has provided a successful route to calculating hard processes in high-energy elementary particle collisions. In the non-perturbative regime calculations are restricted to numerical simulations on a discrete space-time lattice and even these are limited in their applicability.

1.2.1 Lattice Calculations

These numerical calculations are based on a 4D space-time lattice. This is similar to the Ising Model for magnetization in that the simulation sets up particles at lattice sites and calculates the Hamiltonian or action between them. The difference is that lattice spacing can be varied since it does not correspond to a physical lattice. The numerical technique relies on importance sampling so that not all configurations must be calculated. The quarks are situated on lattice sites and the gluons link them. For non-zero T a 3+1D lattice is used. Calculations at zero chemical potential are the most successful. Parameters for the calculation include temperature, T, chemical potential $\mu = 0$, the number of quark degrees of freedom and the number of colours, which is set to the physical value of three for calculations at $\mu = 0$. For no quark degrees of freedom (the quenched approximation) a very precise result is possible giving a critical temperature for the phase transition to deconfinement, $T_c = 270$ MeV. For a finite number of light quarks, usually 2 or 4, a lower value of T_c of around 140-160 MeV [2] is obtained. Some systematic effects remain to be studied though, such as the effects of the size of lattice, the lattice spacing and quark masses. At finite chemical potential, which corresponds to the situation in present experiments, calculations are technically much more difficult. Work is at quite an early stage and involves using only two colours to try to obtain qualitative results. Only the point for the transition at a zero chemical potential is therefore well known. The order of the transition can also be found from calculations. A recent suggestion [3] has been to try to locate the tricritical point at which the order of the phase transition changes.

1.3 Conditions in Heavy-Ion Collisions

Having established, theoretically, the possible existence of a deconfined phase, it is necessary to have some idea whether the conditions achieved in a heavy-ion collision are at least approaching those necessary for its formation. In particular a way of selecting those collisions in which the largest amount of energy is transferred from the initial nuclei to the collision system is required. The energy density and temperature can then be estimated, making use of the kinematic variables defined in appendix A.

1.3.1 Centrality

The centrality is used to choose those collisions where the most energy is deposited in the reaction. For instance, a 10 $\%$ centrality cut means selecting the 10 $\%$ of the inelastic cross-section with the largest amount of energy deposited. There is a relationship with the impact parameter in that the most central collisions have an impact parameter approaching zero. The impact parameter is simply the geometrical distance between the centres of the nuclei in the collision. This leads on to estimating the amount of energy lost by the incoming nuclei in collisions.

1.3.2 Stopping and Energy Density

The maximum energy density achieved in collisions is linked to the stopping of the initial baryons. In the calculation by Bjorken [4] stopping is not assumed and the nuclei pass through one another leaving behind a region from which particles are produced. The calculation leads to an expression for the energy density, ϵ, of

$$\epsilon = \frac{\langle m_T \rangle}{\tau_0 A} \frac{dN}{d\mathrm{y}} \tag{1.1}$$

where A is the overlapping area of the colliding nuclei, $\langle m_T \rangle$ is the average transverse mass, $\frac{dN}{d\mathbf{y}}$ is the rapidity density, τ_0 is a proper time which is estimated to be 1 fm/c and corresponds to the formation time and natural units with $c = 1$ are used. Bjorken performed the calculation for p+p data from the Intersecting Storage Rings programme but it is now possible to substitute the experimentally determined values for Pb+Pb collisions at 158 A.GeV/c. An estimate for the energy density of 3 GeV/fm^3 has been obtained [5] by rewriting equation 1.1 in terms of the transverse energy, E_T per unit rapidity,

$$\epsilon = \frac{N}{\tau_0 A}\frac{dE_T}{d\mathbf{y}} \tag{1.2}$$

where $\frac{N}{A}$ is the number of incident nucleons per unit area.

The energy density for a system of quarks and gluons is calculated from the equation of state and is given by,

$$\epsilon = \left(\frac{T}{160MeV}\right)^4 GeV/fm^3 \tag{1.3}$$

which for critical temperatures of around 160 MeV yields 1 GeV/fm^3.

It seems likely then that the temperatures achieved in heavy-ion collisions, at least at SPS energies, are in the correct range for trying to observe the phase transition between hadronic and quark matter.

1.4 Experimental Programmes

The main experimental programmes investigating quark-gluon plasma formation via heavy-ion collisions are at the AGS at BNL and the SPS at CERN. Recently attempts have been made to include analyses of the data from the lower energy SIS at GSI. These programmes have used heavy-ion beams with fixed targets. In the very near future collider experiments, beginning with the RHIC programme at BNL will commence. They will increase the available energy in the centre-of-mass by an order of magnitude.

Site	Accelerator	Beam Energy GeV	Beam Species	$\sqrt{s}_{nn}$ GeV
GSI	SIS	0.8-1.9	Ni,Au	1.5-2.1
BNL	AGS	14.6	Si	5.4
		2.0-11.6	Au	2.2-4.8
CERN	SPS	200	S,O	19
		158	Pb	17
		(40,80?)	Pb	(8.7,12)
BNL	RHIC	30-100	Au	60-200
CERN	LHC	3000	Pb	6000

Table 1.2: Current and planned experimental relativistic heavy-ion facilities with the centre-of-mass energy per nucleon-nucleon collision, $\sqrt{s}_{nn}$.

In the more distant future one heavy-ion experiment will run at the LHC at CERN. The energies and beams used in these programmes are summarized in table 1.2.

1.5 Thermal Models

In the previous sections the language of thermodynamics has been employed by the use of phrases such as phase transition, temperature and equation of state. Such terms are, strictly, only applicable to macroscopic systems. However, in relativistic heavy-ion collisions there are up to around 400 nucleons in the case of a Pb+Pb collision and, at most, thousands of produced particles so this condition is not fulfilled. The determination of a common temperature for the produced particles would imply that some kind of equilibrium has been achieved. Nevertheless, thermodynamic models are used for heavy-ion collisions.

It is hoped that by performing experiments with different energies and also, though perhaps less importantly, different collision systems, several

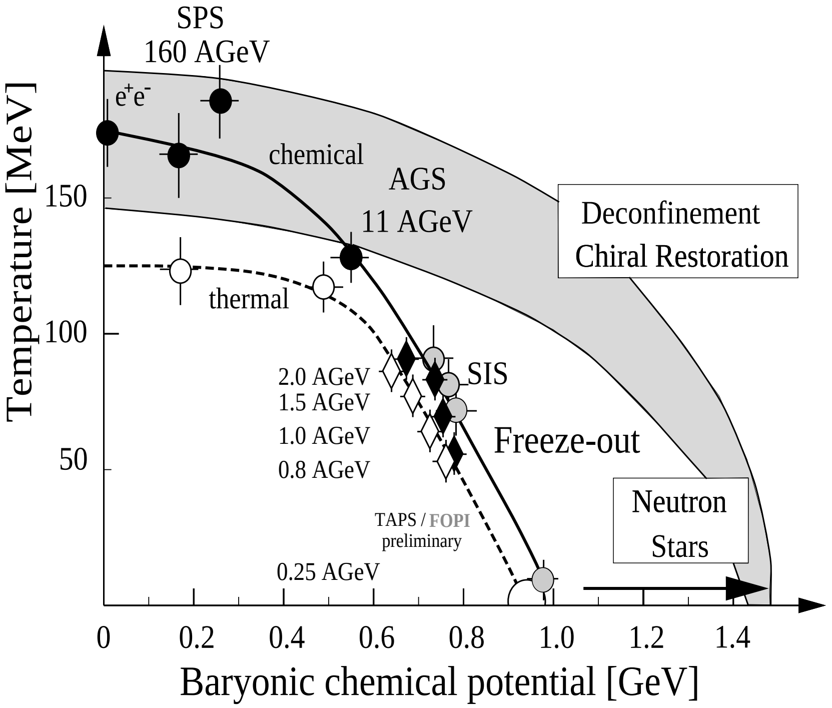

Figure 1.3: The phase diagram for QCD with experimental data points (taken from [6]).

points of the phase diagram for strongly interacting matter may be probed. It has become usual to show a phase diagram as a function of two variables, temperature T and chemical potential μ. Chemical potential is a less familiar thermodynamic variable because it is not used in the study of systems where the particle number is fixed, such as a gas confined to a box. In a quark-gluon plasma or hadron gas system particles can be created from energy, providing the relevant quantum numbers are conserved. In particular a quark-anti-quark pair can be created. The chemical potential is the difference between the energy required to introduce a particle and its antiparticle. Thus, in systems where there are equal numbers of quarks and anti-quarks there is no difference in the energy cost of introducing quarks or anti-quarks and the quark chemical potential is zero.

In nuclear collisions there are an excess of quarks so the chemical potential becomes non-zero. The amount of stopping in the collision determines the value of the chemical potential in the region near mid-rapidity from which the produced particles emerge. Higher energy collisions have less stopping, due to the onset of transparency, and so have a lower chemical potential. Figure 1.3 shows, schematically, the quark and hadron phases with some experimental points. In a thermal model particle distributions are governed by modified Fermi statistics. For an ideal gas of particles in thermal and chemical equilibrium the number, N_i of a particle species i, can be found using the equation,

$$N_i = \frac{g_i V}{(2\pi)^2} \int d^3p e^{-E_i/T+\mu_i/T} \tag{1.4}$$

where μ_i is the chemical potential of the species, V is the system volume, T is the temperature and g_i is a degeneracy factor. An analysis based on this has been applied to many collision systems from e^+e^- and $p\overline{p}$ to Pb+Pb with reasonable success by Beccatini [7]. This type of thermal behaviour may simply be the statistical filling of phase space at hadronization. The question is whether equilibrium is established in each collision system. The equilibria considered are thermal, governing particle momenta and chemical governing the fireball composition. Also, the equilibrium may be local, pertaining to part of the longitudinal phase space or, global.

A model has been developed by Rafelski [8] which includes the effects of non-equilibrium of quark flavours. Many particle yields and ratios can be reproduced by the model. It does, however, take advantage of being able to use data already gathered to find the parameters. However, the number of parameters is relatively low.

A thermal model analysis has also been done by Cleymans [9]. This model explicitly includes conservation laws so that quantum numbers are conserved. He finds that a common chemical and thermal freeze-out description can be used at energies from $\sqrt{s} = 2$ to $\sqrt{s} = 19$ GeV.

Another part of his work stresses the importance of using ratios of particles extrapolated over $y - p_t$ phase space to simplify the extraction of the T and μ parameters [10]. By doing this many of the effects which make the analysis more complicated, such as the excluded volume correction, superposition of fireballs and the effects of flow, cancel out in the ratio.

1.6 Signals for QGP formation

The problem of observing the quark-gluon plasma is that the final state products observed in the experiment have returned to the non-plasma phase via a hadronization process. Therefore, for any proposed signature of QGP formation to be detected experimentally it has to be able to survive the hadronization stage. It should therefore not solely involve the strong interaction otherwise it may well be obscured from observation. The proposed signatures rely on the fact that, once created, they are modified only in electromagnetic and weak interactions or are dynamical observables.

1.6.1 Electromagnetic Probes

Electromagnetic signals survive because they do not interact strongly and escape from the fireball during its evolution. Both photons and dilepton pairs are such signals. The rate of production and the momentum distribution of photons reflect the momentum distribution of quarks and gluons in the plasma. The difficulty comes in separating these thermal signals from the background processes. Dilepton pairs can be formed from the decay of virtual photons and these too have many competing backgrounds which make experiments difficult. The reason for this is that both photon and dilepton backgrounds are generated via mesonic resonances which may themselves exhibit unusual behaviour even in an hadronic scenario. Experiments looking at photons have reported a small excess signal [11] or set limits on the size of the excess [12].

1.6.2 Strangeness

The amount of strangeness produced in collisions is a promising signal for deconfinement [13]. The strangeness content survives because of the timescale for weak decay. Therefore, in terms of a collision, strange quarks are stable. The simplest argument is that there is a different threshold for strangeness production in the deconfined phase. This is because in this phase $s\overline{s}$ pairs can be directly produced at an energy cost of only twice the strange current quark mass, 300 MeV. These strange quarks are then contained in the hadrons at hadronization. However, creation of strange hadrons via hadronic channels requires more energy, for example;

$$p + p \rightarrow p + \Lambda + K^{+} \tag{1.5}$$

$$p + p \rightarrow p + p + \overline{\Lambda} + \Lambda \tag{1.6}$$

These processes require 675 MeV and 2230 MeV respectively which demonstrates that several times more energy is required to produce Λ and $\overline{\Lambda}$ in the final state if there is no intervening deconfined state. Later work focussed on contributions from $g \rightarrow s\overline{s}$ and related processes as a way of producing $s\overline{s}$ pairs more quickly. [14]. An enhancement over $e^{+}e^{-}$ and $p\overline{p}$ collisions is seen in nuclear collisions. However, the enhanced yield may be a consequence of the nature of nucleus-nucleus collisions with each nucleon suffering multiple collisions and there being collisions between them and the produced particles. This may well lead to more opportunities to increase the strangeness content via hadronic channels. The situation is not as clear cut as once thought and depends on the details of calculations. Particular interest has focussed on strange anti-baryons as these contain only the newly created anti-quarks. Models have been developed using novel production mechanisms such as colour ropes [15] and double string formation and fragmentation [16] as a way of reproducing anti-baryon yields. Within the thermal model yields of strange particles can be reproduced by the introduction of a new parameter, γ_s, the strangeness saturation factor. This takes account of the incomplete chemical equilibrium between strange and non-strange quarks. The parameter is incorporated into the thermal model such that the yield of a strange particle is proportional to $\gamma_s \exp\frac{\mu}{T}$ instead of $\exp\frac{\mu}{T}$, as in equation 1.4. The distribution of strange quarks amongst the different hadronic species is however at the equilibrium value, a condition known as *relative* chemical equilibrium. This is due to the fact that strangeness exchanging reactions are relatively quick.

Parameters in the thermal model may be determined experimentally by taking the ratio of particle yields. Many of the factors which determine the yield cancel in the ratio leaving only the various fugacities, defined by $\lambda = \exp\frac{\mu}{T}$. The saturation factor, γ_s also remains if the ratio is between particle species with different $|S|$. For example the ratio, $\frac{\Lambda}{\Xi}$ is given by,

$$\frac{\Lambda}{\Xi} = \frac{\gamma_s \lambda_q^2 \lambda_s}{\gamma_s^2 \lambda_q \lambda_s^2} = \frac{\lambda_q}{\gamma_s \lambda_s} \tag{1.7}$$

where λ_q is a generic fugacity used for both u and d quarks. By taking an appropriate number of different ratios all of the parameters can be determined. A value of $\gamma_s \approx 1$ is thought to favour a QGP interpretation whereas a lower value favours a purely hadronic explanation, since the equilibration time is much longer in a hadronic system.

There have been a large number of experiments which have collected data on strange hadron production. Rather than make detailed comparisons for each species it is simpler to look at the overall trends from the data. It is possible to get a good estimate of the overall strangeness content of the produced particles by looking at quantities derived from the total number of kaons. This is because the sum of the charged and neutral kaons contain $\approx 70\%$ of the total strange quarks and anti-quarks. Strangeness enhancement in heavy-ion collisions in comparison to p-p and p-nucleus collisions is shown in figure 1.4. The data were all acquired at SPS energies. The plotted quantity is the sum of all the kaon multiplicities, K^+, K^-, and $2K_S^0$ to

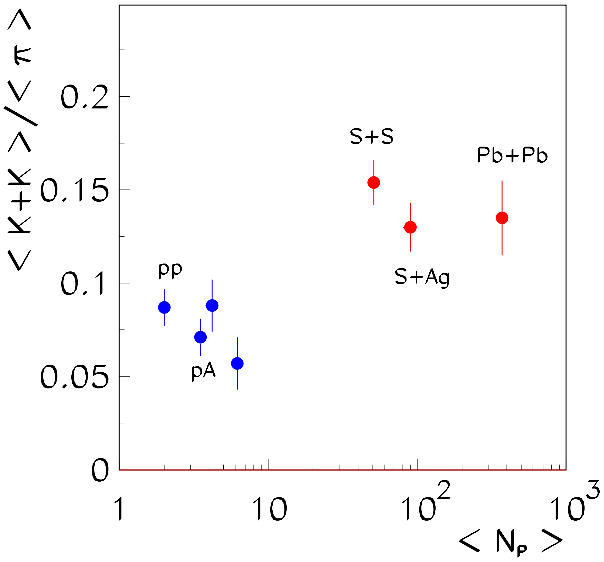

Figure 1.4: The dependence of the $\frac{K}{\pi}$ ratio, defined as the sum of multiplicities of all kaons divided by all pions, on the number of participants (taken from [18] which contains the references to the original data).

account for the unmeasured K_L^0, divided by the sum of the pion multiplicities, $\pi^{\pm}$ and π^0 against the number of participant nucleons. The value for A+A collisions is roughly twice that for p+p and p+A collisions. In a similar analysis [17] the quantity E_S is constructed using,

$$E_S = \frac{\langle K + \overline{K} \rangle + \langle \Lambda \rangle}{\langle \pi \rangle} \tag{1.8}$$

where $\langle K + \overline{K} \rangle$ is the sum of the kaon multiplicities, $\langle \pi \rangle$ is the sum of the pion multiplicities and $\langle \Lambda \rangle$ is the Λ multiplicity. This quantity is designed to account for most of the strangeness in the collision. It is shown to be enhanced in A+A collisions over N+N collisions at energies of 4.5 GeV, 11.6-14.6 GeV and 200 GeV. The dependence of E_S on the collision energy is also found to be qualitatively different. For heavy-ion collisions there is initially a steep increase on the ratio up to AGS energies after which it appears not to increase strongly with energy, whereas for p+p collisions the value is still rising at SPS energies (although it is still numerically lower). Location of the energy at which the behaviour changes would be interesting.

1.6.3 Charmonium Suppression

The yields of the bound $c\bar{c}$ states, J/Ψ and Ψ', have been predicted to be suppressed by the formation of a deconfined state [19]. This is due to them "dissolving" in the plasma, where the effects of colour charge screening cause disassociation. Experiments NA38 and NA50, have studied J/Ψ production in S-induced and Pb-induced reactions respectively, at SPS energies. The results from NA38 [20] show a suppression of the J/Ψ which can be accounted for by nuclear absorption in a continuation of the trend from lighter systems. However, results from NA50 Pb+Pb collision data [21] show an extra anomalous suppression. This result has created a great deal of interest and there have been attempts to model the data and explain the effect theoretically. Some models do not require the formation of a deconfined state in order to reproduce the data. As an example reference [23] models J/Ψ production by a nucleon-nucleon cascade followed by breakup whilst in the excited $c\bar{c}$ states (which have larger absorption cross sections) and a final state interaction with co-moving mesons. This is able to describe the experimental data. The development of these models does not rule out the existence of a QGP phase but removes the necessity of one in describing the data. The reported experimental effect remains and has been verified by a higher statistics analysis [22] showing the onset of the anomalous suppression moving from peripheral to central Pb+Pb collisions.

1.6.4 Event-by-Event Fluctuations

In the region of a phase transition, phenomena develop on a larger length scale than typifies the behaviour in the phases either side of the transition.

This type of behaviour may be compared with the boiling process in water where the bubbles formed are many orders of magnitude larger than the inter-molecular distances. Large fluctuations in certain observables might therefore be expected at the QCD phase transition. It is possible to search for these event-by-event fluctuations by looking for non-statistical deviations in distributions of events when compared to events constructed by combining particles from the event ensemble. The variation in mean p_t is one example of such an observable. This type of dynamical fluctuation is not necessarily removed by the hadronization process. It is essential that an experiment searching for event-by-event effects has a large acceptance in order to have a high sensitivity. There is however evidence for the absence of such effects [24]. The same experiment has also made a preliminary study of the $\frac{K}{\pi}$ ratio, presented in [25], which again failed to show any significant variation beyond that expected statistically.

1.7 Work Presented

In this thesis the work done in analyzing the data for $|S| = 1$ strange particle production within the NA49 experiment is presented. The NA49 experiment is a large acceptance hadron spectrometer which enables measurements of several strange and non-strange particles, emerging from the collision, to be made. It operates at the SPS at CERN. The strangeness content is of particular interest since this is newly created in collisions. The singly strange particles carry most of the strangeness produced in the collision so measurements of these give a good indication of the total strangeness content, which is an indirect signal of deconfinement, as was explained in section 1.6.2. Measurements of strange particle production also contribute to the wider set of data which are needed in order to place the collision system studied on the phase diagram by finding the ratios from which T and μ can be determined.

Chapter 2

The NA49 Experiment

2.1 Overview of the Experiment

The NA49 experiment operates at the CERN Super Proton Synchrotron (SPS) facility. It is a fixed target experiment designed to study heavy-ion collisions using a Pb beam, with energy 158 GeV per nucleon, on a Pb target. The main emphasis of the design is a large acceptance measurement of hadronic production in the collision system. The principal data taking effort is concentrated on central Pb-Pb collisions where QGP formation is most likely. Data taking started in the Autumn of 1994 when the experiment was partially assembled. The data presented in this thesis was collected in the Autumn 1995 run. Pb-Pb data has been taken each Autumn since, with the exception of 1997 when a fire caused a re-scheduling of the beam time, and is planned to continue until 2000. In addition to the main data taking effort, non-central Pb-Pb, proton-proton and proton-Pb collisions at a beam energy of 158 GeV have been studied and it is possible that other lighter nucleus-nucleus collision systems or lower beam energies may also be studied.

The experimental apparatus consists of several detectors (figure 2.1) which complement each other in their acceptances and the aspects of the collision which they allow to be studied. Of the main tracking systems, working downstream from the target, the first are the two Vertex Time Projection Chambers (TPCs) known as VTPC1 and VTPC2. They are situated within magnetic fields, provided by two large super-conducting magnets, of 1.5 T and 1.1 T respectively. Next are the two large Main TPCs (MTPCs), one either side of the beam, known as MTPC-L and MTPC-R. The TPCs are of a modular construction with the MTPCs each having 25 sectors arranged in a five by five grid and the VTPCs have six sectors arranged as shown (figure 2.1). Behind the MTPCs are the Time of Flight (TOF) walls and after these are the Ring Calorimeter (RCAL), which measures the transverse energy production and the Veto Calorimeter (VCAL) which forms part of the trigger. Upstream of the target are several smaller detectors used for triggering. In the NA49 coordinate system the z-axis is defined along the nominal beam direction with the beam particles travelling in the positive z direction. The y-axis is vertical with up being positive, and the x-axis forms a right-handed coordinate system with these two axes. The origin is at the centre of Vertex Magnet-2.

The basic idea of this layout is that the charged final state particles are separated in the magnetic field, which enables their charge and momentum to be determined by examination of the track curvature in the VTPCs. The MTPCs may be used for $\frac{dE}{dx}$ measurements in the relativistic rise region which, in conjunction with TOF measurements, allow particle identification to be performed. The MTPCs are also used to study charged particle production in the forward rapidity region. The momentum can be found if it is assumed that the tracks originate from the primary interaction vertex which defines their trajectory through the magnetic field. This assumption is not valid for secondary vertex tracks, the daughters of weakly decaying particles.

A large fraction ($\approx 80\%$) of the ~ 1500 charged particles produced in an

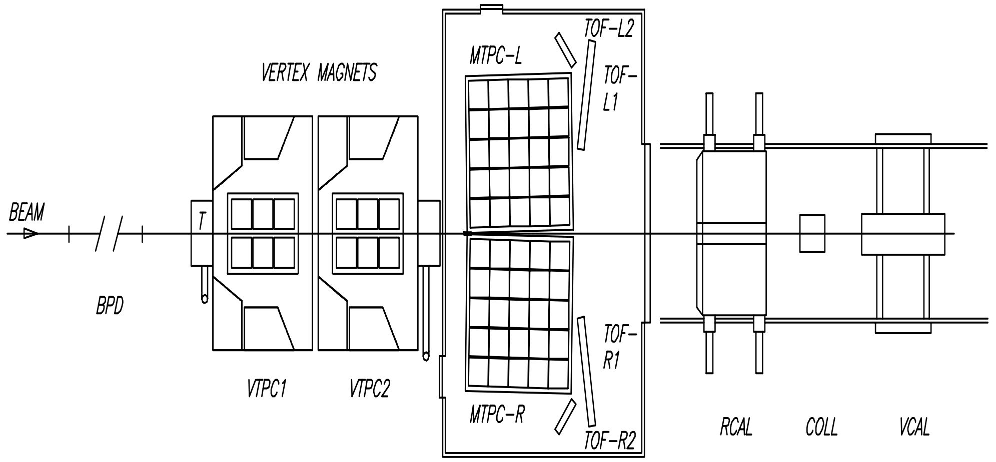

Figure 2.1: Schematic plan view of the positions of the various elements comprising the NA49 experiment.

event are detected by the NA49 detectors and this allows some properties of the collision system to be studied on an *event-by-event* basis. This was indeed one of the identified physics goals of the experiment. In relation to the study of the production of strange particles in the collision, the VTPCs can reconstruct secondary tracks and determine their momenta which allows neutral particles to be reconstructed from their decays to charged final states. An extension of this technique to two step decays means that doubly strange baryons can also be reconstructed. The MTPCs can reconstruct charged kaon decays, via the $K \rightarrow \mu\nu$ decay channel and charged kaons themselves can also be identified by either $\frac{dE}{dx}$ measurements or TOF information. It is sometimes necessary to use a combination of both, depending on their momentum, in order to achieve a better separation. It is thus possible with the NA49 detector system to measure the production of singly and doubly strange baryons and both neutral and charged kaons.

2.2 The SPS Facility

The NA49 experiment is situated in the SPS North Area experimental hall. The beam is extracted from the SPS and travels ≈ 1 km down the beam line. It is both split and collimated before delivery to the experiment. During the Autumn 1995 run beam was supplied to the Heavy Ion Programme experiments at the same time as the LEP Programme. There were three spills per minute and the spill for the lead beam had a duration of ≈ 5 s leaving a further 15 s before the next spill arrived. The event rate in the NA49 experiment is not limited by the amount of beam that can be supplied. The limiting factors are the readout time of the detector, the build up of charge in the TPCs and the DAQ system (see section 2.4.4.) which was designed with these factors in mind. This led to, typically, around 10^5 Pb ions per spill being delivered after selection by the upstream collimators.

2.3 Beam and Trigger Conditions

The NA49 experiment is principally concerned with measuring *central* Pb-Pb collisions. The experiment must be set up so that data is only recorded when a Pb beam particle undergoes a collision in the target. This is the function of the beam definition and trigger detectors. Specifically, the design must seek to eliminate the possibility of recording data from those interactions of beam particles which were not in the target and interactions of beam *fragments* with the target. Additionally, events from central collisions must be selected. It is also desirable to know the actual, as opposed to nominal, position of the beam on the target. The sub-systems used in the trigger have evolved over the lifetime of the experiment but this section describes the system that operated during the 1995 Pb-Pb data-taking run.

The beam definition and trigger detectors are in order of increasing z,

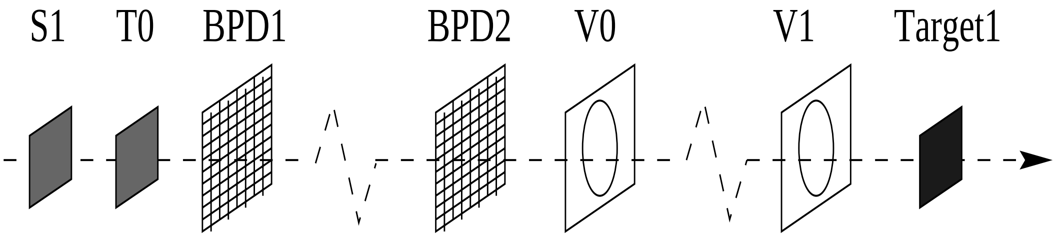

Figure 2.2: Trigger and beam definition detectors preceding target.

as they would appear travelling with the beam: S1 Quartz counter in vacuum, 50 × 30 × 0.2 mm^3, at z=-39.772 m; T0 Quartz counter in vacuum, 25 × 25 × 0.5 mm^3, the positive beam definition counter, at z=-39.507 m; beam position detector (BPD1), a Si strip detector in vacuum, at z=-39.113 m; BPD2 Si strip detector in vacuum at z=-16.426 m; V0 Scintillator in vacuum, of 80 mm diameter with a 10 mm diameter hole, at z=-15.441 m; Filament scanner (FISC), horizontally and vertically aligned wires, at z=-14.746 m; V1 large scintillator, covered with lead with a 40 mm hole, at z=-6.630 m; Target1, the Main production target, at z=-5.801 m; S4 Veto counter 20 × 20 × 1mm Quartz, at z=9.400 m; Veto Calorimeter at z=21.800 m. Those detectors upstream of the target are pictured in figure 2.2.

S1 and T0 are quartz Cerenkov counters which identify the beam particle species by the emitted Cerenkov light. They can reject beam contamination which may be present due to upstream interactions. S1 and T0 have an electronic discriminator window to reject beam fragments and pileup. V0 and V1 are veto counters and are used in anti-coincidence with S1 and T0 in order to reject interactions in the counters or the remaining gas. The FISC is used during beam tuning to provide beam profile information and is removed during data taking. It has two movable perpendicular thin plastic scintillator wires and each is read out by two photomultiplier tubes.

BPD1 and BPD2 provide measurements of the beam position in the x and y directions perpendicular to the beam. They have 2×192 Si strips each 200 microns wide. Additionally there are BPD3 and BPD4, as above, but with 2×48 strips, positioned downstream of the target. They are used for defining the beam when alternative target positions are being used.

The target itself is a 220 mg / cm^{-2} Pb foil. Detection of a Pb ion in the S4 counter means that no interaction took place in the target so a trigger signal is not sent. In fact, it is possible to have an interaction in the material between the target and the S4 counter and these events would also have been recorded. With this in mind a new integrated target and counter housing was produced with the veto counter only a few cm from the target. This was used for the 1996 and subsequent data taking.

The centrality trigger utilizes a calorimeter built for the NA5 experiment. This calorimeter (VCAL) is situated 27.4m downstream of the target. Less energy is deposited in the calorimeter in more central collisions as more of the nucleons participate in the collision. This is because in more central collisions more energy is used in particle production, resulting in more energy associated with transverse motion of particles. The signal from the calorimeter is compared to predictions from the independent microscopic hadronic cascade model VENUS [26]. This enables a correlation with impact parameter to be made. It is possible to set a discriminator to obtain a trigger corresponding to the desired centrality range. For the 1995 run the trigger was chosen so that the 5% of the inelastic cross-section with the highest centrality, corresponding to impact parameter $b<3$ fm, were selected.

2.4 Time Projection Chambers

The TPC operates as a tracking device by reconstructing the tracks left by charged particles as they pass through a volume of gas, causing ionization

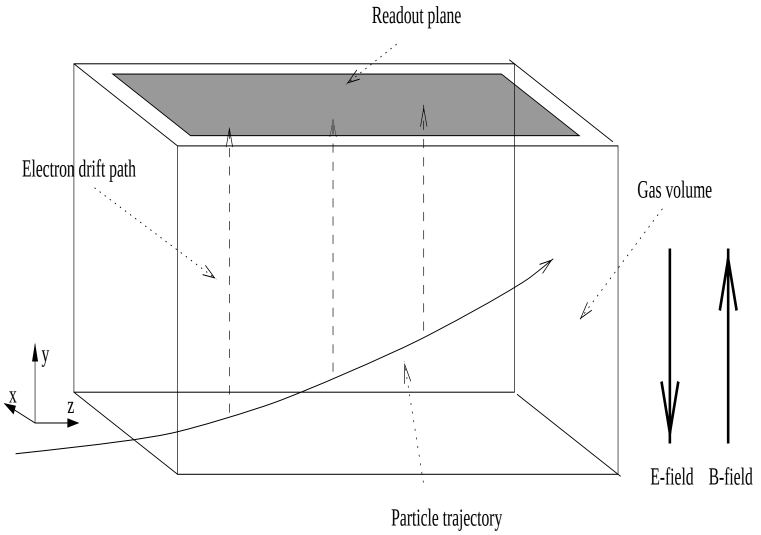

Figure 2.3: Schematic representation of TPC operation.

of the gas. This allows a unique 3D picture of the tracks to be built up at the readout plane (figure 2.3). All of the NA49 TPCs follow this basic pattern of operation although there are differences in the details of their construction and use. The reconstruction of neutral strange particles uses tracks reconstructed by the VTPCs as they are situated in magnetic fields and the momentum of tracks reconstructed by them can be determined. The two VTPCs differ from one another in the positioning of their readout pads which are optimized for the bending of the tracks which they reconstruct. The dimensions and mode of operation of the two detectors are basically the same. There are more substantial differences between the Main TPCs and VTPCs. The most obvious of these is that the MTPCs operate in a field free region. They are also of much larger volume. The arrangement of the readout pads is again optimized differently according to the track topology. The two MTPCs are mirror images of one another.

The reconstruction process begins with the passage of the charged particle through the gas, producing electrons by ionization along the particle

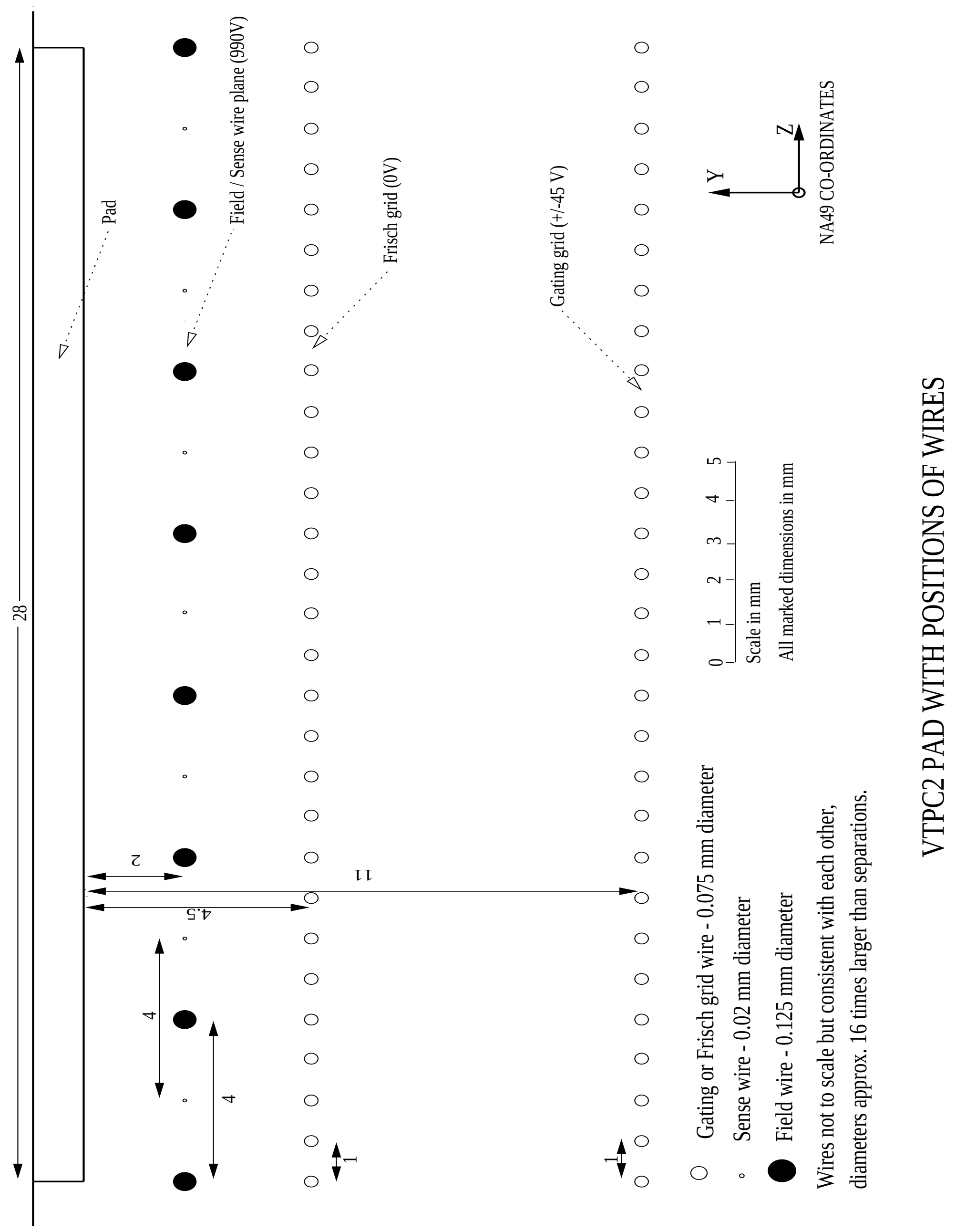

Figure 2.4: The arrangement of the wire elements at the readout plane.

trajectory. The electrons drift upwards to the readout region (figure 2.4) under the influence of a constant, vertically aligned electric field which is maintained in the TPC. Electrons enter the readout region and are accelerated, producing an avalanche effect. The positive ions produced by the avalanche induce a charge on the cathode pads. The pads are read out and the charge information stored in time bins, hence each time bin corresponds to a slice through the TPC at a different y-position. The conversion to determine the actual y-position is done using the drift velocity v_D.

2.4.1 Construction

There were several factors influencing the construction and situation of the TPCs. Firstly, the Pb ion beam cannot pass through the active gas volume, that which is read out, because of the very large amount of ionization it produces. This meant that the TPC modules in the VTPCs had to be situated on either side of the beam. The beam does pass through the gas volume but the electrons produced by ionization will, in the main, recombine as there is no electric field to separate the positive and negative charges. This is because there are two separate field cages which define the electric field. Details of the arrangement can be seen in figure 2.5. Some particularly energetic electrons are scattered into the active volume where they themselves produce ionization. These are seen as background tracks in the event.

There is a requirement that the TPC should be constructed from as little material as possible with low Z material being used in order to minimize multiple scattering and secondary interactions. Balanced against this is the requirement for mechanical stability and a geometry known to high precision, especially the readout plane which must be flat. There is also a need to minimize inhomogeneities in the electric and magnetic fields so the design should try to avoid introducing edge effects which may be dif-

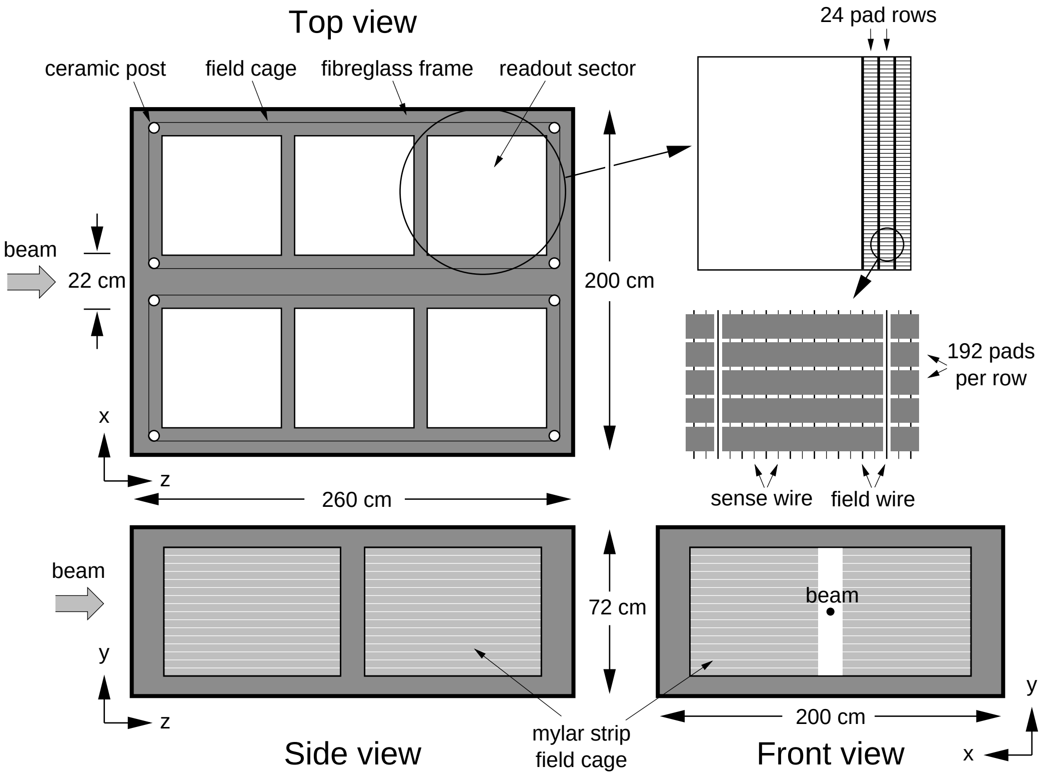

Figure 2.5: Sectional views showing TPC geometry and construction (taken from [31]).

ficult to take into account later. A solution using aluminized mylar strips suspended from ceramic posts was chosen. Details of the construction can be found in [27]. Gas purity has to be maintained to avoid contamination with oxygen which has an order of magnitude higher electron attachment. The envelope for gas containment surrounds the high-voltage cage but is completely separate from the drift field structure. The envelope is a double layer of mylar foil with a thin layer in between which is flushed with nitrogen gas. This protects the active volume against diffusion of impurities.

The construction of the readout region is shown in figure 2.4. The drifting electrons first pass through the gating grid. This is switched to a potential of -45 V by the trigger, for the duration of the readout, so that positive ions created by the avalanche do not re-enter the drift volume when they are repelled by the sense wires. The Frisch grid defines both the drift field and the field which causes the avalanche which has a large gradient. In the same plane are the sense and field wires. The avalanche electrons are collected on the sense wires. The field wires shape the field lines and ensure that they do not wrap around behind the sense wires. This would be undesirable as it would cause the electrons to have drift distances which vary with position in the x-z plane. The field wires also help to reduce repulsion between the sense wires which could lead to an effect whereby consecutive wires are staggered up and down.

2.4.2 Physics of detection

The behavior of the ionization electrons as they drift is important in determining the eventual resolution with which tracks can be reconstructed. The ionization electrons diffuse in both the directions transverse to the drift direction and the drift (vertical) direction during the drift. The drift length may be up to 66.6 cm in the VTPCs and 111.7 cm in the MTPCs. The eventual two track resolution depends on the pad response function which has several terms. The equation for determining the total width, σ is,

$$\sigma^2 = \sigma_0^2 + \sigma_D^2 \lambda (1 + tan^2\alpha) + \sigma_\alpha^2 tan^2\alpha \tag{2.1}$$

Where the intrinsic width, σ_0, is the width which would be observed if the charge emanated form a point source near to the wire. It depends on geometrical factors such as the distance of the sense wires from the pad plane. The pad crossing angle, α, which is the angle at which the track crosses the pad in the x-z plane, also introduces an extra width. There is also a term proportional to the drift length, λ which contributes to the width depending on the contribution from the diffusion coefficient for the gas, σ_D. The pad pitch was determined by minimizing the crossing angle of tracks in a simulation. An equation similar to equation 2.1 can be constructed for the width in the longitudinal (drift) direction. The equation for determining the single track resolution has a similar form but with numerically smaller coefficients.

Narrow charge distributions are desirable in order to resolve close (and almost parallel) tracks. The high track densities mean that a two track resolution of a few millimetres is required and so the gas mixture plays an important role. The drift velocities change approximately linearly with a change of the electric field (i.e. they are unsaturated.) The transverse diffusion coefficient is much reduced by the presence of the magnetic field which is another consideration in the eventual choice of gas for the different TPCs. In broad terms the choice is between a “fast gas” which has a high drift velocity but high diffusion coefficient and a “slow gas” which has a low diffusion coefficient but also a low drift velocity. An investigation [29] was performed so as to be able to choose the gases for the NA49 TPCs. For the VTPCs a mixture of Ne/CO_2 (91/9) was chosen which has low intrinsic transverse and longitudinal diffusion constants, of around 220 μm/cm$^{\frac{1}{2}}$ and gives a drift velocity of 1.4 cm/μs when the potential difference across the drift volume is 13 kV. For the MTPCs the mixture was 91/4.5/4.5 of Ar/CH_4/CO_2. This has a drift velocity $\approx 50\%$ higher, when combined with a potential difference of 19 kV across the chamber, so that the readout time matches that of the VTPC. The longitudinal diffusion constant is therefore also larger for this gas mixture. The effect of magnetic induction reduces the transverse diffusion coefficients to 95 μm/cm$^{\frac{1}{2}}$ in VTPC1 and 137 μm/cm$^{\frac{1}{2}}$ in VTPC2. The intrinsic term, σ_0, for the resolution is found to be 120 μm which results in a single track resolution in the region of 200 μm, for a track from the centre of the chamber, being achieved.

2.4.3 Magnetic field

The VTPCs are situated inside magnetic fields and ideally one would like an extremely homogeneous field precisely aligned with the electric field. In practice this is not available so it is necessary to have good measurement of the field strength and direction. Two approaches were taken to solve this problem. A calculation of the field was performed with a computer program [30] using knowledge of the construction of and currents in the magnet. Detailed measurements with Hall probes were taken over the large volume of the field. The two methods give good agreement for the magnetic field and a field map was constructed, which uses information from both methods, for use in the reconstruction of the data.

2.4.4 Readout Electronics and DAQ

The vast majority of the data volume for an event comes from the TPCs for which there are around 180000 electronics channels. This leads to a raw event size of around 100 MB before zero suppression. The data from several events must be transferred into the data acquisition (DAQ) system for zero suppression to be performed, along with the merging of the other smaller amounts of data from the TOF walls and beam detectors to form complete events before the events are passed to the tape controller. The TPC pad readout signals are sent to the DAQ receiver boards via Front End (FE) cards and Control and Transfer (CT) Boards for event building. The functions of these sub-systems is set out below. Each FE card is connected to 32 pads and houses two types of chip, one for preamplification and pulse shaping (PASA) and also an analog storage device, the switched capacitor array and analog to digital converter (SCA / ADC.) As there are 16 channels per chip two of each type are required. The preamp. is an integration circuit which, on receiving an event trigger, starts integration which continues for 50 μs. The pulse shaper creates a near-Gaussian pulse shape with a well defined width. The output from the shaper is recorded in amplitude and time. The analog information is stored in the SCA and each time bucket is digitized by an ADC. The SCA may be visualized as 512 capacitors in parallel. This SCA is slower than a flash ADC but this is acceptable because the event rate is rather low in NA49. The advantage is that the SCA is smaller and produces less heat, important considerations with the high channel density. The shaper signal is directed to the capacitors at 10 MHz, implying a 100 ns interval per capacitor which corresponds to a size of 1.3mm in the VTPCs. The charge from each capacitor is sent to the ADC at a rate of 100 kHz. The ADC itself is a "Wilkinson" style single slope ramp and counter. Conversion typically, since it depends on pulse height, takes 10 μs per pulse, so requires 5 ms for all 512 slices. The whole FE card produces 2W of heat so an elaborate cooling system is required to ensure that the TPC operating conditions remain stable.

The CT boards are situated close to the TPCs (a maximum distance of 1.8m for the VTPCs and 0.5m in the case of the MTPCs). Each board is connected to 24 FE cards and also supplies them with power. The CT board can generate simulated data and allow charge injection to the preamps. It provides signals to control the custom chips on the FE card. Data are sent from the CT boards to the receiver boards where it is read into VRAM. The board also transmits so-called "house keeping" data, for example, board identification, voltages and event numbers. The boards sense any over-currents which may develop and switch off the appropriate channels. Monitor data is sent to a computer in the counting house which runs a diagnostic program.

The receiver boards are each linked to four CT boards by an optical fibre link. The receiver board stores the data during the 5 s beam spill. A board contains enough memory for storage of 32 events. Data is received and sent through a field programmable gate array (FPGA) at 6.25 MB/s.

The FPGA reorders the pad data and performs the pedestal subtraction. Pedestal subtraction is the removal of the signal that would be obtained on average from an empty channel, and its purpose is to improve data compression and also reduce noise. A digital signal processor then does the zero suppression. The technique involves looking for pulses, above a threshold value, in the time direction and writing these out along with the immediately preceding and postpending information.

At this stage a complete event is about 8 MB in size. All of this must be accomplished and the data recorded before the next beam spill arrives. The tape drive used is a SONY DIR 1000M ID1 tape drive which uses 100 GB tapes. Its maximum speed of writing is 16MB/s if writing continuously which would place a limit on the event rate of about 40 per spill cycle.

2.5 Calorimeters and Time of Flight Detectors

The other detectors in the NA49 experiment are the Ring Calorimeter (RCAL in figure 2.1), Veto Calorimeter and the TOF systems. The TOF systems aid in particle identification. There were two types in operation in the 1995 run, a pixel scintillator system and a grid scintillator system, labelled TOF-L/R1 and TOF-L/R2 in figure 2.1. They have different designs as described in [27]. They are positioned behind the TPCs since it is necessary that a particle has been tracked before it hits the TOF wall and it would not be good to allow the electronics associated with the detector to shadow the TPCs.

The Ring and Veto Calorimeters were originally built for the NA5 experiment [28]. They are both photon-hadron calorimeters but they are constructed with different geometries. Each has a photon section at the front and a hadron section to the rear. Both of the detectors are constructed in segments. The Ring Calorimeter has 24 segments, each of which is a 15°

section, arranged in a ring with a diameter of approximately 3 m and a central hole of 0.5 m. The Veto Calorimeter is segmented into 4 cells with an octagonal sensitive area approximately 1×1 m^2. For both detectors the front photon section consists of layers of lead sandwiched between plastic scintillation material. The rear hadron sections are made from alternate layers of iron and scintillator. In the Ring Calorimeter each segment is subdivided into 10 pieces, each of which is readout by one or two wavelength shifter rods. There are a total of 14 rods per segment. The rods are doped with different wavelength shifter materials in the photon and hadron parts which enables the signal from each to be transmitted down the same rod. The light from each rod or pair of rods is split and fed into two photomultiplier tubes, with appropriate filters, to obtain a photon and hadron signal. Readout in the Veto Calorimeter is achieved using wavelength shifter bars with separate bars for the hadron and photon parts of each segment. Each has a triangular end glued to a photomultiplier tube.

In its present position the Ring Calorimeter covers the projectile rapidity region and is able to give information on transverse energy production and event anisotropy. The transverse energy production information is required for calculating the energy density achieved in the collisions. The Veto Calorimeter forms part of the trigger system as has been described in Section 2.3.

Chapter 3

Event Reconstruction

3.1 Introduction

Event reconstruction proceeds via several stages which include finding strange particle decays. The software that does this is in fact a chain of modular form rather than a single program. The raw event data, in the from of the ADC counts, is loaded into memory and each module operates on this data. The data is written out as a reconstructed event, including tracks and vertices, to the Data Summary Tape (DST) after the final module has run. The main stages, each consisting of a number of modules, are cluster-finding to produce space points, tracking, and for this analysis, the V0 search. There are also other modules which operate at various points in the chain providing functions which are not used in the V0 search such as reconstruction of hits in the TOF detectors, the fitting of tracks to the main vertex and calculation of the $\frac{dE}{dx}$. By having this software infrastructure the data can be organised so that the information pertaining to a physical object can be kept together in a single data object[1] or series of linked objects. These objects stay resident in the computer memory whilst different modules are run which can fill in or modify the data in the existing objects or

---

[1] actually a C structure

create new objects. It is also possible with this system to have objects filled with constant data which remain in memory between events such as the geometry information and program control parameters. The rest of this chapter describes the modules that are required when reconstructing V0s.

3.2 Clusters and Corrections

The modules which reconstruct space points can be divided into two classes; those which locate the clusters of charge in the TPCs, the cluster finders, and those which correct the position of these clusters in order to remove known distortions in the data, the correction clients. There are actually three different cluster finder program modules each of which reconstructs the space points in a particular detector.

They share several common features which will be described. The modules are `dipt` which finds clusters in VTPC1, `clus49` which examines VTPC2 data and `mtrac points` which finds clusters in the MTPCs. Each searches the data for a particular pad row in bins in the the time(y) and pad(x) directions. For the VTPCs this results in a set of space points which have fixed z co-ordinates at one of the 72 positions corresponding to the centres of the pad rows. The MTPCs are slightly different, because they are at an angle to the beam, so a conversion between co-ordinate systems needs to be done but the idea is the same. The cluster is found by examining the number of ADC counts in each pad-time bin and looking for bins with counts above a threshold value. The environment in which the cluster finder operates is illustrated in figure 3.1. This shows the large amount of noise in the chamber, caused mainly by spiralling electrons, and associated problem of charge saturation in the preamp. The program searches adjacent bins to build up an “island” of charge. The weighted mean in the pad and time direction is then determined. These are converted into the x and y coordinates which, for the time direction, requires a conversion using the drift velocity. Cuts are used to determine what are good clusters and it is here that the two VTPC codes differ. The `clus49` cluster model allows for charge to be collected on a number of pads but in fact cuts out those which are not 2 or 3 pad clusters. The width of a pad is 3.5 mm whereas a time bin corresponds to less than 1.5 mm. The model for VTPC1 employed by `dipt` on the other hand uses a series of so-called morphology measures. These are based on measuring the eccentricity of the cluster. This is done by finding the component of the quadrupole moment along axes rotated by 45° to the x and y directions and a component of the quadrupole moment perpendicular to this. This allows two perpendicular eccentricities to be defined. Clusters may then be categorized [32] by their radius in the newly created eccentricity space.

The correction clients follow the cluster finding modules and modify the positions of the space points in order to take out systematic distortions in the data. These may either be based on a correction derived from the physical equations describing the electron drift, or be based on phenomenological equations or tables. The most important correction, in the VTPCs, removes the charge transport distortion $\vec{E} \times \vec{B}$ which can be over 2 cm in magnitude close to the edges of the chamber. When charge arrives at the readout plane the time bin in which it arrived is recorded and this can be converted into a y co-ordinate by using the drift velocity. However, this procedure assumes a vertical drift path for the electrons and this is in general not correct due to the shape of the B field. The electron's motion in electric and magnetic fields, $\vec{E}$ and $\vec{B}$ respectively, is governed by the equation

$$m\frac{d\vec{v}}{dt} = q(\vec{E} + \vec{v} \times \vec{B}) + m\vec{A} \tag{3.1}$$

where m is the electron mass, q is the charge on the electron, and $m\vec{A}$ is a time varying force which effectively describes collisions with the gas. For

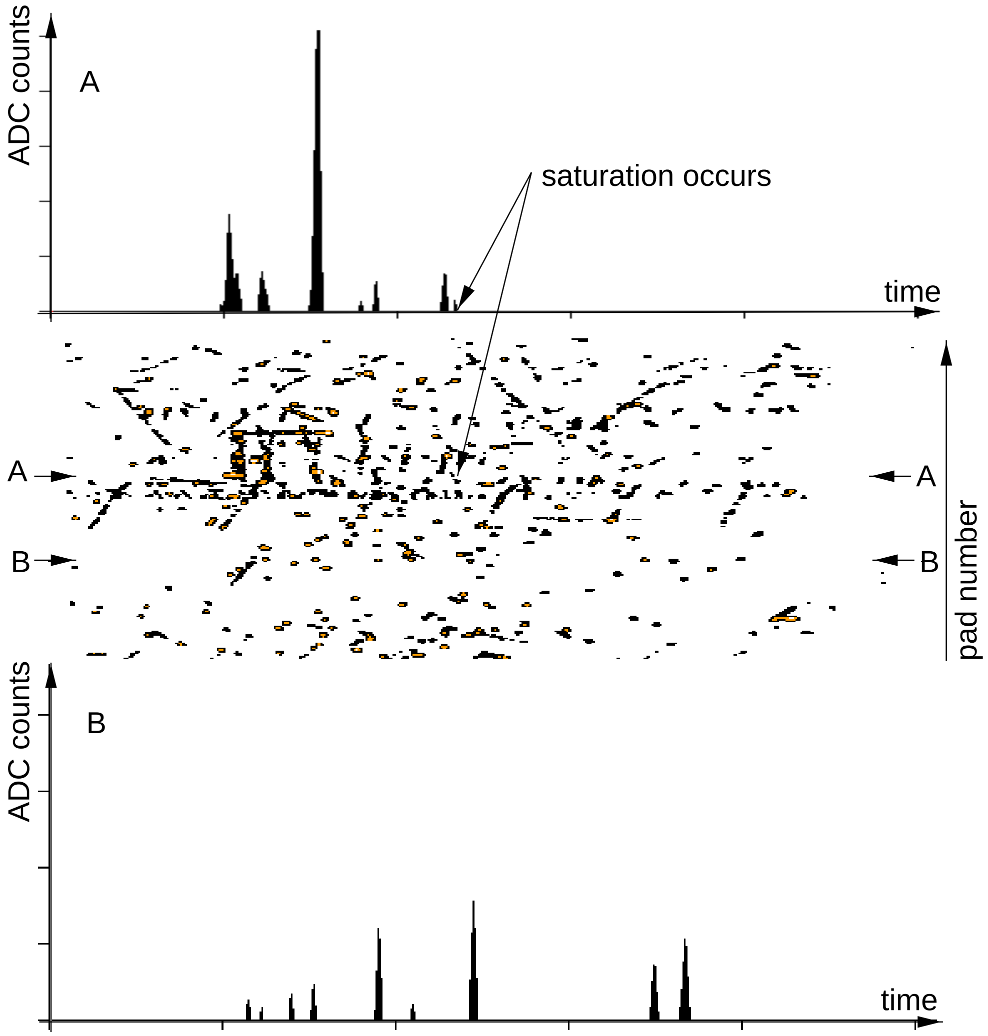

Figure 3.1: A projection in the pad-time (x-y) plane of the raw data for one of the VTPC2 sectors. Above (labelled A) is the ADC count versus time plot for a pad in which saturation occurs. Below (labelled B) is the same plot for a "normal" pad.

a solution with constant $\vec{v}$ (i.e. $\frac{d\vec{v}}{dt} = 0$) the restorative force $m\vec{A}$ can be replaced by $\frac{m\vec{v}}{\tau}$, where τ is the mean time between collisions. This leads to the following solution [33]

$$\vec{v} = \frac{\mu}{1 + \omega^2\tau^2}\left(\vec{E} + \frac{\vec{E} \times \vec{B}}{B}\omega\tau + \frac{(\vec{E}.\vec{B})\vec{B}}{B^2}\omega^2\tau^2\right) \tag{3.2}$$

where $\omega = \frac{qB}{m}$ and $\mu = \frac{q\tau}{m}$. When $\vec{E}$ and $\vec{B}$ are parallel the term in $\vec{E} \times \vec{B}$ is zero and $\vec{v}$ is along the direction of the fields. However, when there is an angle between the fields this term gives a velocity component perpendicular to both of the fields so the original straight line assumption is invalid. There is then, effectively, a distortion in the points which must be corrected. Its magnitude is largest near the edge of the drift volume where the $\vec{B}$ field is not parallel to the y-axis.

The method for correcting this involves following the path (backwards) in time, from the readout plane over the known time interval, for each point to find the true origin of the detected charge.

Other modules correct for mechanical distortions and inhomogeneities in the electric field.

3.3 Tracking

The next stages are concerned with joining the space points together to form tracks. In general, there are several ways to solve the track reconstruction problem and a comprehensive discussion of tracking methods can be found in Ref. [34]. The solution finally arrived at for the NA49 experiment combines elements of both the Track Following and Track Road methods. This became the most practical solution as it built upon earlier work within the Collaboration. A scheme was subsequently devised, known as Global Tracking, which aimed to improve the tracking by using information from all of the TPCs. This works by using the tracks found in one detector to look for tracks in another.

The first rounds of data production undertaken concentrated on reconstruction of the tracks in each detector separately. The methods initially chosen were those best suited to the tracking environments in those detectors and the aims of the analysis. For the VTPCs this meant adopting a Track Following method. The implementation used is described below.

3.3.1 Track Following in the VTPCs

Initially a seed is sought of five points in a row. This is achieved by taking a hit from the last row and making an extension to the hits in the next row. Several seeds may be grown from one hit. A linear extrapolation is made to find the third hit for a seed and a point assigned if it exists within the limits set for x and y. If no point exists the seed is rejected. The seed is grown until it has five hits in a row using a helical fit for extrapolation. This has the advantage that no information about the track direction is assumed so tracks not originating from the target will be found which is obviously important when searching for decay product tracks. The seed is now ready to be fully extrapolated into a track.

The seed is projected through the TPC to create a track. The assignment of a hit to a track continues row by row using the track following method. At each row the nearest hit is added to the track and fits performed in the y-z and x-z planes. The y-z fit is linear and the x-z fit to a circle. If either fit falls outside predetermined limits on the χ^2 probability, the added point is rejected. A point assigned to a particular track may not be used by another, in contrast to the seed forming stage where a hit may be used many times. Assignment of points to a track continues until it leaves the TPC or a gap of more than 9 rows is found. Allowance is made for the two inter-sector gaps. At this stage, if the track has less than 8 hits it is rejected and the points assigned to it are returned to the pool for future use.

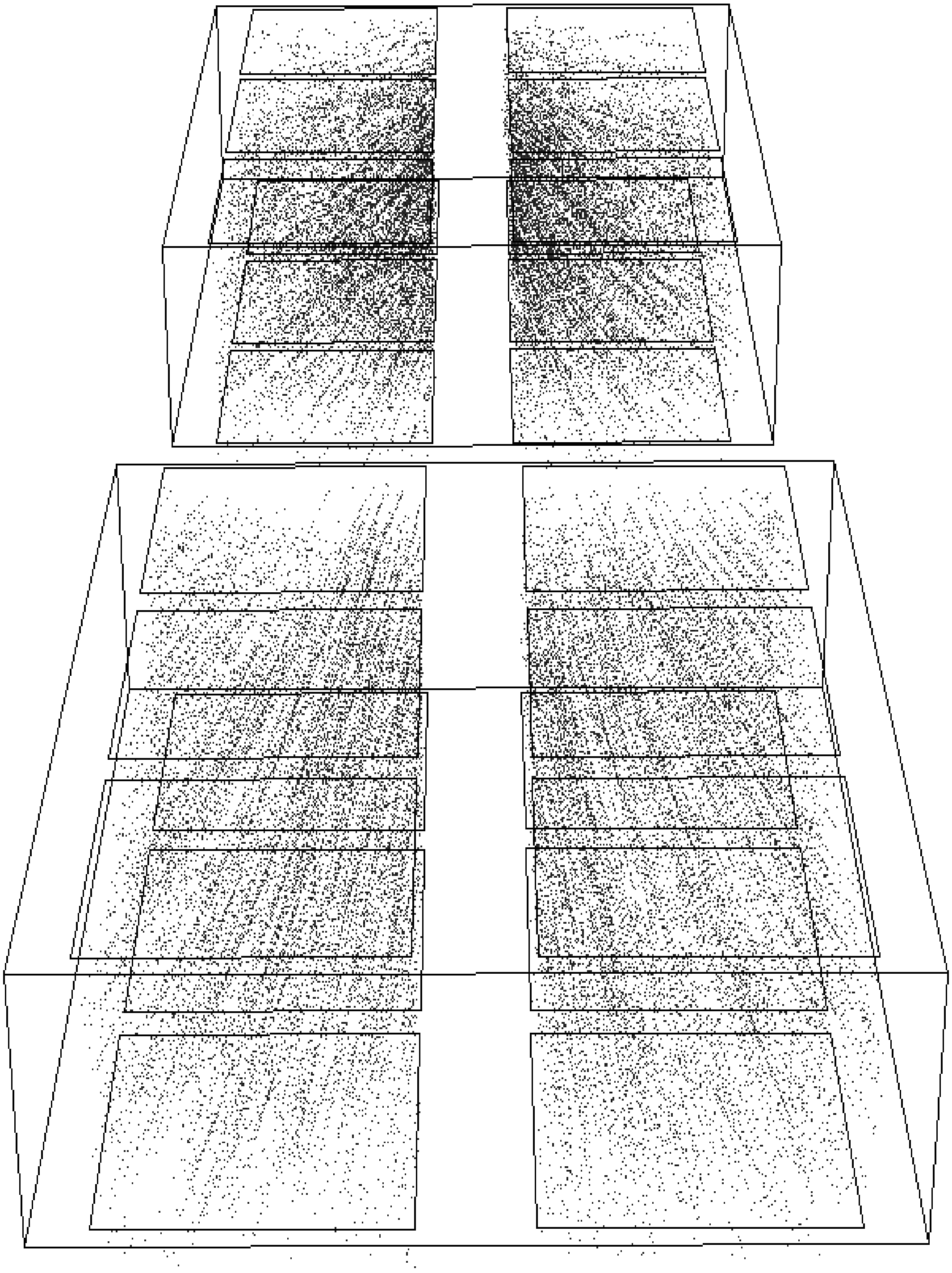

Figure 3.2: The set of reconstructed space points which serve as the input data for tracking. Only VTPC1 (back) and VTPC2 (front) are shown for clarity.

3.3.2 Global Tracking

Global tracking starts once the space points in all of the TPCs have been found, as pictured in figure 3.2. Tracking starts in the detectors furthest downstream, the MTPCs. Here there is no magnetic field and the tracks are straight lines. Each of these tracks can be assigned a momentum if one assumes that they originate from the primary (interaction) vertex. This assumption then gives them a known path through the magnetic field and each can be extrapolated towards the target to find out if they pass through VTPC2. Tracking can then be carried out in VTPC2 using the Track Road method employing the prior knowledge of where the track is expected to appear. This scheme is, in general, not suitable for finding the tracks from the daughter particles of weak decays as none of them come from the primary vertex, although some of them may appear to do so if the decay is close to the target. Clearly, those particles which do not leave tracks in the MTPC will also not be found by this method. A second step is therefore employed where a Track Following method, as described in section 3.3, is used which takes as its input those space points which remain unassigned after the first VTPC2 tracking stage. This strategy is now repeated for VTPC1. All tracks are extrapolated into VTPC1 and the two tracking stages are run. In the case of this TPC a substantial fraction of the tracks are only found by the second stage because they bend in the magnetic field and so do not reach VTPC2. Finally, it is possible to extrapolate tracks downstream, from VTPC2 to MTPC, in order to find track pieces which were missed by the first pass.

Tracks are passed to the next module in the reconstruction chain for a momentum fit to be performed. This fits the track to the points by varying the momentum components. The fourth order Runge-Kutta method [37] is employed to integrate the equation of motion requiring knowledge of the B field, provided by the magnetic field map, in order that the track may have a variable radius of curvature. During this stage there is no constraint that the track should point to the target. This would be undesirable as it would tend to distort the momentum of tracks from particles which are decay products. In fact, tracks are refitted assuming that they originate from the interaction vertex at a later stage, after the V0 search has been performed, as this can give an improved momentum. The results of the fits using different assumptions are stored separately when the data are written out. The set of reconstructed tracks for a single event are shown in figure 3.3.

3.4 V0 Reconstruction

The search for neutral strange particles, known as V0s because of the characteristic ’V‘ shape produced by the decay, takes place once all of the tracks have been reconstructed and fitted. The input data are the fitted global tracks which may pass through one or more of the TPCs. The basic idea is to extrapolate pairs of tracks consisting of one positive track and one negative track upstream to look for a distance of closest approach. Only those tracks passing a quality criterion of having 20 space points in at least one of the VTPCs are considered. This is because a track must pass through one of the VTPCs in order to have a measured momentum as opposed to the one provided by the MTPC tracking which assumes the path through the magnetic field in order to calculate the momentum. Also, track pairs must pass a cut requiring that both tracks start in the same half of the TPC if they are in VTPC1. This cut was chosen after studying the acceptance and the data which revealed that a large number of background pairs are added, by including combinations where the tracks are in opposite sides of VTPC1, without greatly increasing the number accepted. The tracks are extrapolated in the z-direction in 2cm steps and the distance between them

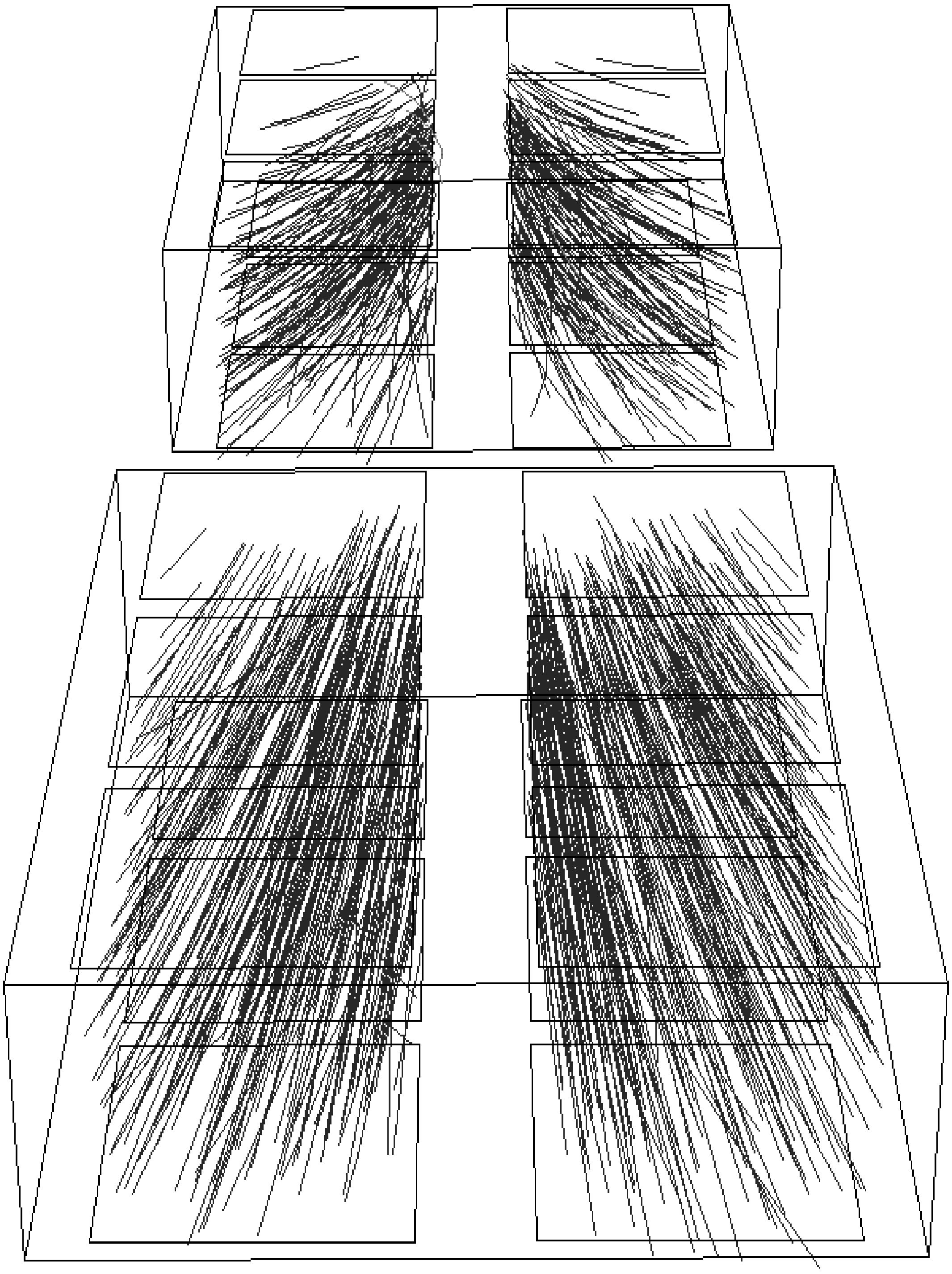

Figure 3.3: The set of reconstructed tracks for a single event. The view is as in figure 3.2.

in the x and y directions calculated. If the distance decreases and then becomes larger over 3 steps then a distance of closest approach (DCA) must have occurred somewhere in between. A DCA of less then 1cm in the x and y directions is required. Pairs of tracks satisfying this criterion become V0 candidates. These are then subject to a number of other cuts in order to obtain a reasonable signal to background ratio.

3.4.1 Cuts

It has been found that a cut on the separation in the x direction of the two daughters when extrapolated to the target plane [35] is useful for rejecting candidates formed from pairs of primary tracks. This is better than a simple cut which requires the daughters not to point to the primary vertex because in the case of $\Lambda(\overline{\Lambda})$ decay the (anti-)proton carries away most of the momentum and may then appear to come from the target. This is illustrated in figure 3.4. Also illustrated is the target cut, $|\mathrm{xtarg}|$ which is a cut on how well the reconstructed neutral particle points back to the target position.

A cut on the z co-ordinate of the decay vertex is required because the combinatorial background becomes larger with decreasing z (i.e. going upstream). This increase is due to the increasing tracking density approaching the target which means that more random track crossings appear to form V0 candidates. Since each VTPC has a different acceptance it makes sense to have a different cut for those candidates starting in either VTPC1 or VTPC2. The final choice for this cut was determined by looking at the data. Figure 3.5 shows the invariant mass, using the Λ hypothesis, plotted against the z position of the decay vertex for both VT1[2] and VT2 as an example of how the cuts are tuned. Calculation of invariant masses is dealt with in section 4.3.1. In practice, the z-cut can be applied before a DCA is found by not tracking upstream beyond the relevant z position. A balance

---

[2] VT1 and VT2 are synonymous with VTPC1 and VTPC2 respectively.

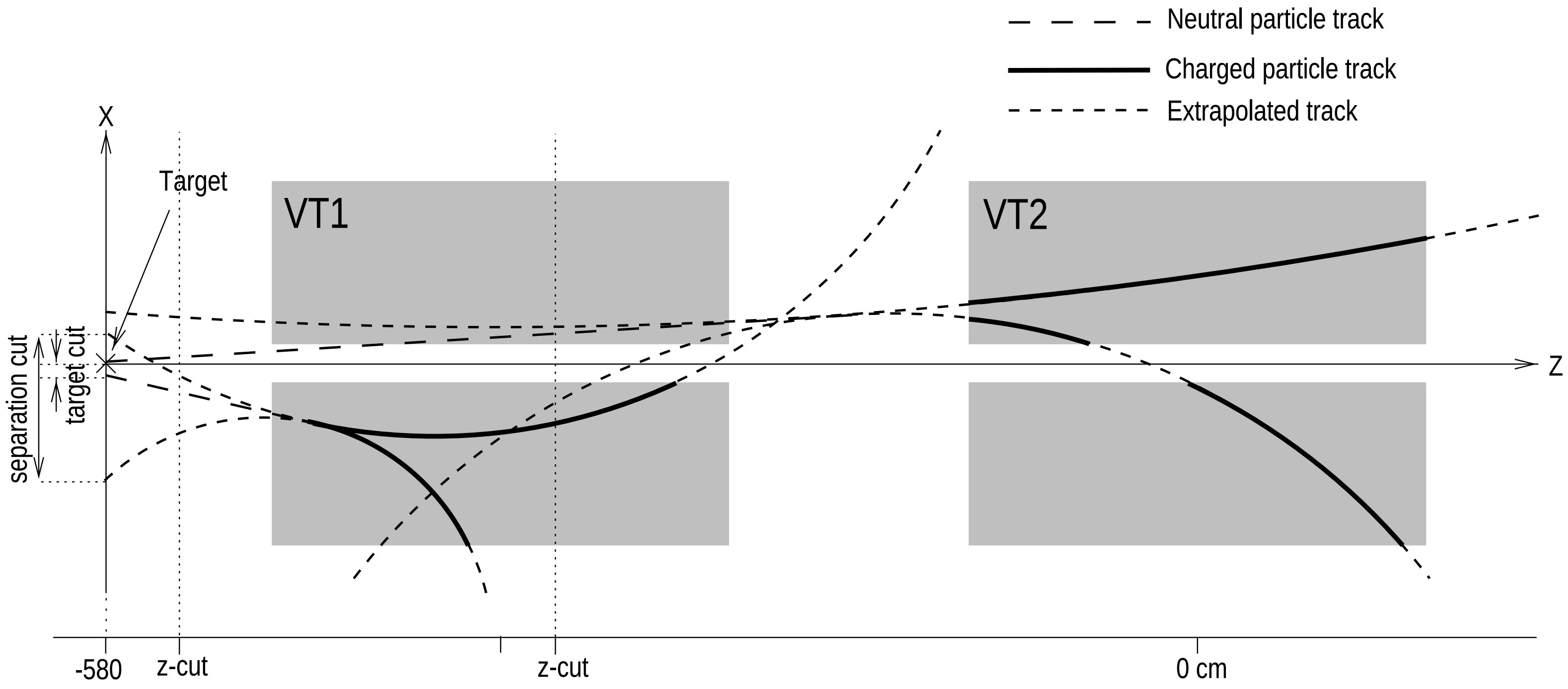

Figure 3.4: Plan view of neutral particles decaying into tracks crossing VT1 and VT2 showing the calculated cut quantities.

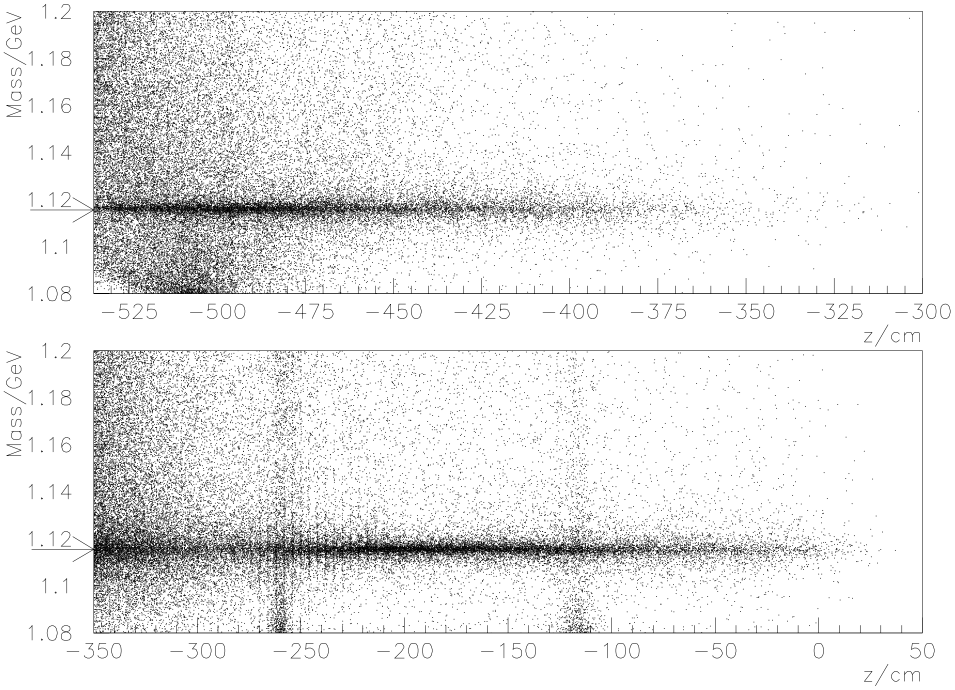

Figure 3.5: The invariant mass under the Λ hypothesis plotted against the z position of the decay vertex for VT1 candidates (top) and VT2 candidates (lower). The background increases going towards the target. The vertical bands are from background associated with the ceramic support posts. An arrow marks the nominal Λ mass.

Cut	Old VT2 value	New VT2 value	VT1 value
$x_+ - x_-$	5 cm	2 cm	2 cm
$\|xtarg\|$	3.0 cm	3.0 cm	3.0 cm
minimum z	-430 cm	-350 cm	-555 cm
ϕ angle	no cut	$0.2 <\|\phi\|< 2.9$	$0.2 <\|\phi\|< 2.9$

Table 3.1: Cuts implemented at the V0 finding stage.

must be sought between cutting too hard, in which case one is restricted to the candidates recorded on the DST, and allowing in too many background candidates which will lead to prohibitively long computing times for the next stage which is the fitting of the V0 candidates. A cut can of course always be tightened during the subsequent post-DST analysis. The cuts were originally tuned for data reconstructed from VTPC2 only [36]. The values decided upon are shown in the first column of table 3.1.

An angle ϕ is defined by constructing two vectors, y', which is normal to the momentum vector of the parent and lies in a plane defined by the trajectory of the parent and the y-axis of the NA49 co-ordinate system and n which is the normal to the decay plane. The angle ϕ is simply the angle between y' and n as illustrated in figure 3.6. A study in which this angle was calculated showed that the background preferentially appears with values of ϕ around $\pm\pi$ and zero as shown in figure 3.7. This is because for background tracks to combine to form a candidate they must cross due to bending in the magnetic field. If they are not approximately in the x-z plane they have a large separation in y at the crossing point and do not form a candidate. Thus, those appearing to form decays have values of ϕ close to those mentioned, as the normal to the “decay” plane is roughly (anti-)parallel to the y-axis. Cutting in ϕ close to this region reduces substantially the amount of background. This allowed some of the cuts for VTPC2 candidates to be relaxed slightly at the post-DST analysis stage (see section

4.2.) New values were chosen for the production of this dataset (table 3.1 column two). Additionally, cut values had to be found for the VTPC1 candidates and these are shown in table 3.1, third column.

3.5 V0 Fitting

All candidates passing the cuts are passed to the V0 fitting module. This performs a nine parameter fit, the parameters being the three momentum components of each of the daughter tracks and the three space co-ordinates of the decay vertex. It is assumed that the tracks in the V0 candidate come from a common decay vertex, equivalently their DCA is zero. The fit minimizes the χ^2 statistic by the Levenberg-Marquardt method [37]. The parameters are varied in turn and χ^2 recalculated after each alteration. If the alteration results in an improved χ^2 then the new parameter value is adopted otherwise the old one is retained. The step size, the amount by which a parameter is changed on each iteration, is variable which allows the efficient minimization of χ^2.

This completes the reconstruction chain for neutral strange particles and the candidates are written to the DST, from which they are extracted for further analysis.

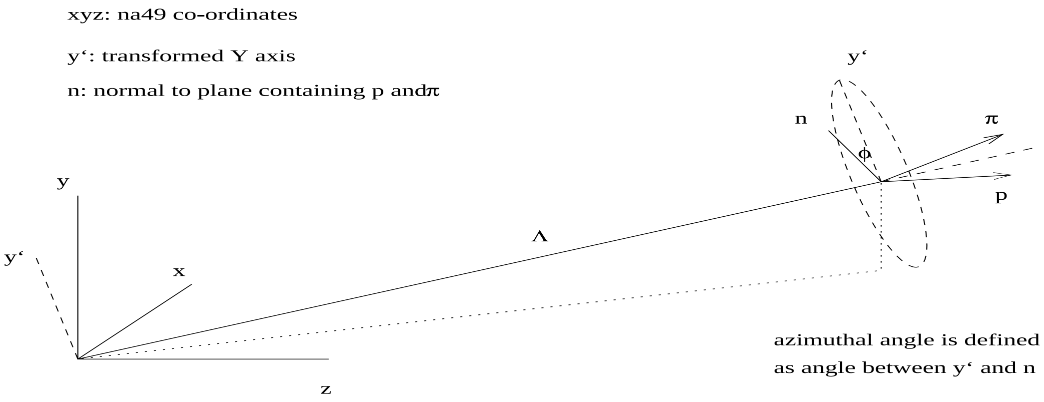

Figure 3.6: Definition of the ϕ variable used as a cut.

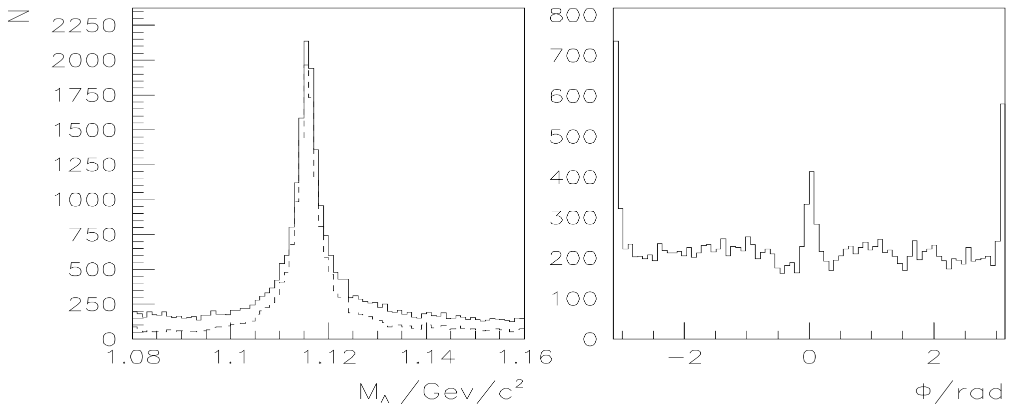

Figure 3.7: Left panel: lambda mass peak with (dashed line) and without (solid line) cut on ϕ variable. Right panel: ϕ distribution for candidates in a 30 MeV mass window.

Chapter 4

Analysis and Results

4.1 Introduction

This chapter describes the steps required in taking the set of fitted V0 candidates to produce the final corrected transverse momentum and rapidity distributions of neutral, singly-strange particles. This process starts with the extraction of the raw yield from the data and is followed by the calculation of corrections to take account of the geometrical acceptance of the detectors. Following on from this is the analysis of events with Monte Carlo (MC) generated particles embedded into them in order to calculate the efficiency of the software chain in finding the particles of interest. Checks were performed to estimate whether there had been any double counting in the data by looking at the properties of any pairs of particles in the same event. The Λ and $\overline{\Lambda}$ data also require an additional correction to allow for the fact that a significant fraction of the observed lambdas are the daughters of weakly decaying multi-strange particles. Finally, the method of combining the data with the various corrections to produce the final corrected distributions is described.

Cut	value in `v0find`	value at extraction
$\lvert xtarg \rvert$	3.0 cm	1.5 cm
minimum z (VT1)	-555 cm	-535 cm
minimum z (VT2)	-350 cm	-350 cm

Table 4.1: Cuts tightened during the extraction of data from the DST.

4.2 Extraction from the DST.

The Data Summary Tapes (DSTs) for this dataset were produced at CERN. The 10^5 events used in this analysis produced a data volume of order 100 GB so the first step was to extract the relevant quantities for V0 analysis and produce a more manageable dataset. This resulted in a reduction of the data volume by a factor of a few thousand. During this step several of the cuts were tightened to further reduce the contamination from background. The values used are listed in table 4.1 along with the original values used in `v0find`.

Files were produced with candidates from a single run which typically, if there were no problems during data taking, contained around 11000 events and 45000 v0 candidates. Data were extracted from the DSTs from several runs, with a total number of events of 104k. These events were recorded with the experiment set up with the magnetic fields in the standard minus (STD-) configuration where positively charged particles are bent towards the negative x direction. There were an additional 20k events extracted from the standard plus (STD+) configuration data. There were several hundred thousand more events recorded during the 1995 run but it was found that these events were reconstructed whilst there were problems with the reconstruction software so they were unsuitable for use in the final analysis. Events taken in subsequent years (over 1M) were not available for analysis at this time.

4.3 Classification of candidates

The extracted V0 candidates could be any one of the following; real Λ, $\overline{\Lambda}$ or K_S^0 decays, background from random track crossings, γ conversions and secondary interactions of produced particles. It is not possible to unambiguously classify each candidate but it can be done on a statistical basis utilizing the kinematic properties of the reconstructed decay. This principally relies on two methods, invariant mass calculations and the Armenteros-Podolanski plot.

4.3.1 Invariant mass analysis

The candidate could be any one of the decays, $\Lambda \to p\pi^-$, $\overline{\Lambda} \to \overline{p}\pi^+$ $K_S^0 \to \pi^+\pi^-$. It is possible to calculate the invariant mass, M, of the parent particle involved in a decay, under certain assumptions, using equation 4.1 which is derived from energy and momentum conservation considerations.

$$M(m_1, m_2) = \sqrt{m_1^2 + m_2^2 + 2(E_1 E_2 - \vec{p_1}.\vec{p_2})} \tag{4.1}$$

Here, m_i is the rest mass, $\vec{p_i}$ is the momentum and E_i is the energy of the daughter particle. The energy can be calculated from $E = \sqrt{m^2 + p^2}$. The assumptions which must be made are the rest masses of the charged daughter particles. By substituting the three possible combinations of the proton and pion masses for m_1 and m_2, one obtains the three possible invariant masses for each candidate. This allows invariant mass spectra to be plotted for each of the three parent species as in figure 4.1.

4.3.2 The Armenteros Plot

The Armenteros-Podolanski plot [38] is formed by plotting two kinematic variables against one another. One variable is p_{tarm}, defined as the momentum component of the daughter perpendicular to the momentum vector of

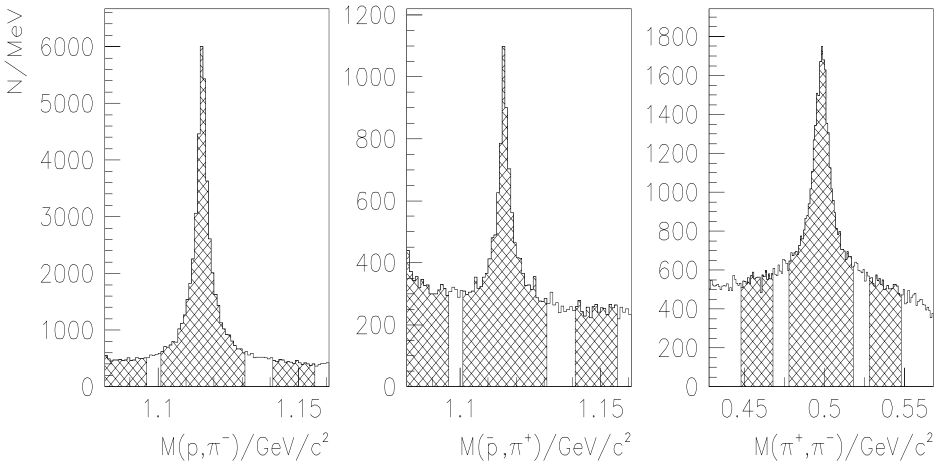

Figure 4.1: Invariant mass spectra for Λ (left), $\overline{\Lambda}$ (middle) and K^0_S (right). In each panel the central hatched region is taken as the signal plus background and the two hatched regions on either side used for background subtraction. Numerical values are given in table 4.2.

the parent. Due to conservation of momentum, p_{tarm} is identical for each daughter particle. The other variable, α, is defined as,

$$\alpha = \frac{p^+_{||} - p^-_{||}}{p^+_{||} + p^-_{||}} \tag{4.2}$$

where $p^{\pm}_{||}$ is the momentum component of the ±ve particle in a direction parallel to the momentum of the parent, measured in the laboratory frame. When this equation is rewritten in terms of variables in the rest frame of the parent it becomes,

$$\alpha = \frac{2p_{||} + \beta(E^+ - E^-)}{\beta m_0} \tag{4.3}$$

where $p_{||}$ is the component of the daughter momentum along the direction of motion of the parent, $E^{\pm}$ is the energy of the ±ve daughter, m_0 is the rest mass of the parent and β is the boost from the rest frame to the laboratory frame. Thus the α variable is approximately Lorentz invariant since β, given by the ratio $\frac{E}{p}$ for the parent in the laboratory frame, has a value of 0.92 at the lowest measured rapidity and tends toward 1 going to higher rapidities. It is relatively simple to calculate the loci of allowed values of α and p_{tarm} by considering the fraction of the momentum of the decay produced in the decay in the transverse directions. In the Λ and $\overline{\Lambda}$ decays the proton or anti-proton takes more of the momentum so the loci of allowed values for these decays have centres shifted away from zero. The K_S^0 decay has products of identical mass so the locus is symmetric around an α of zero. More momentum is available in the K_S^0 decay as reflected in the maximum value of p_{tarm}. The theoretical loci are shown in figure 4.2. This plot may be compared with that obtained from experiment in figure 4.3. The experimental plot is for 10000 events. From figure 4.2 it can be seen that there are points where the locus for K_S^0 decays crosses those for Λ and $\overline{\Lambda}$ decays. At these points it is not possible to distinguish between species. There is never any ambiguity between Λ and $\overline{\Lambda}$ decays. Since the mass resolution in the experiment is finite, the experimental points lie around the theoretical loci. Those with a higher invariant mass lie above the curve and vice versa. The point of overlap in the theoretical plot becomes an area of overlap in the experimental plot. This is shown in detail in figure 4.4 where the overlap between Λ and K_S^0 is shown when cuts are placed on the invariant Λ and K_S^0 masses of ± 15 MeV and ± 20 MeV respectively, around the data book values.

The actual extraction of the number of counts is done by background subtraction using the invariant mass spectra. For each particle species a window is defined which is considered to contain the signal plus background. To subtract the background, bands are defined on either side and the number of counts in these bands is subtracted from the number in the original window. This is illustrated in figure 4.1 where the windows and

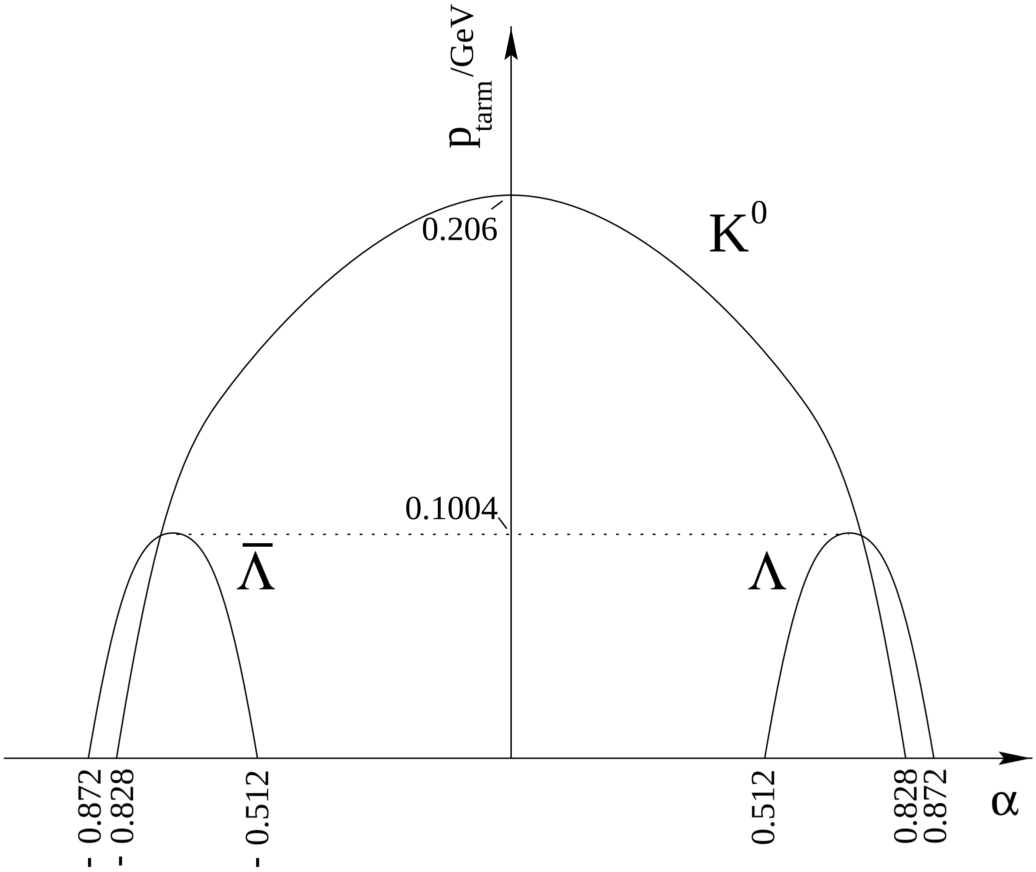

Figure 4.2: Theoretically allowed values of α and p_{tarm} for neutral strange particle decays.

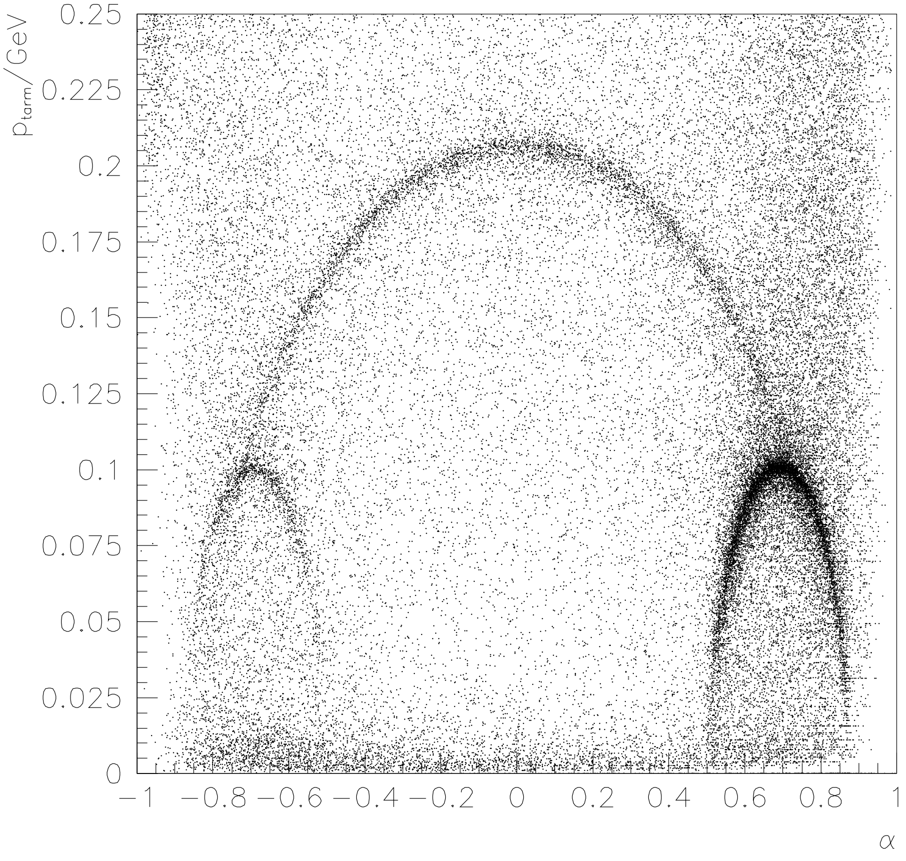

Figure 4.3: Plot of p_{tarm} versus α for a subset of the experimental data.

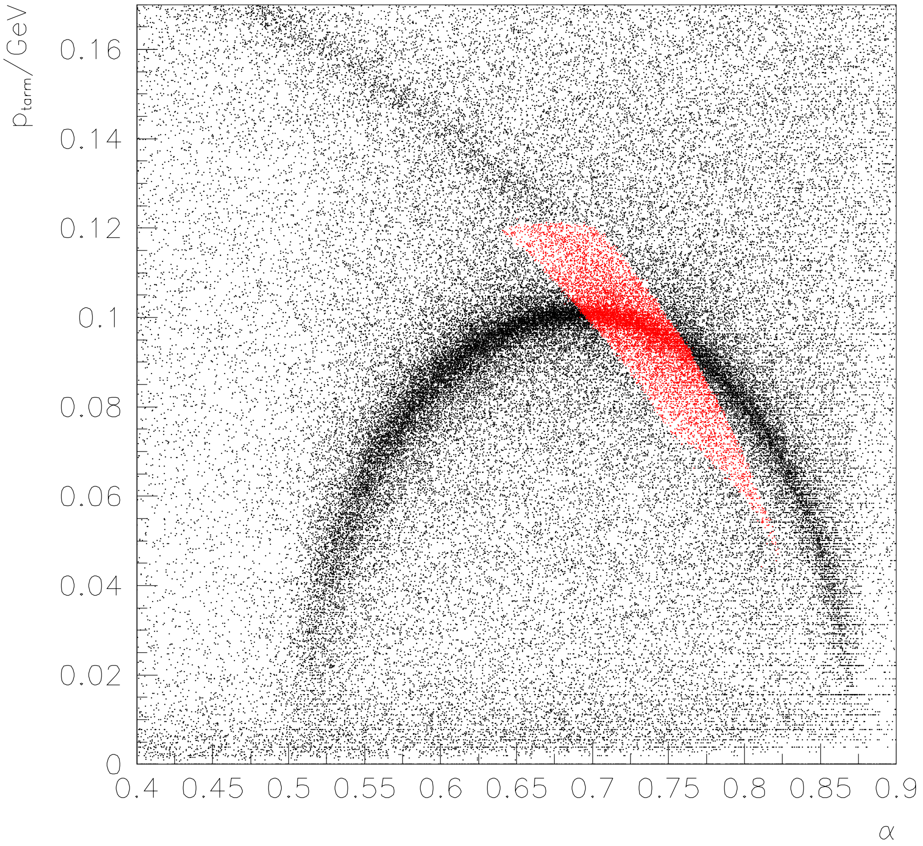

Figure 4.4: The overlap, shown in colour, between Λ and K_S^0 mass windows on the Armenteros plot.

Particle	Lower Band	Mass Window	Upper Band
Λ and $\overline{\Lambda}$	$1.081 < M < 1.096$	$1.101 < M < 1.131$	$1.141 < M < 1.156$
K^0_S	$0.448 < M < 0.468$	$0.478 < M < 0.518$	$0.528 < M < 0.548$

Table 4.2: Cuts in GeV/c^2 on invariant mass, M, used in the background subtraction procedure.

bands are shown. The numerical values used for the cuts on invariant mass, M, are listed in table 4.2. This method relies on the background being linear in the intervals chosen.

4.4 Corrections

To convert the distribution of particles measured by the detectors into the physical distribution that was emitted from the collision, a number of correction factors must be generated. The *acceptance* correction accounts for the geometrical coverage of the detectors. This correction can be large, varying from around five up to a factor of 100 in some part of phase space, but it can be calculated with high precision. This means that it does not contribute significantly to the error on the final result. Also, the factors involved in the calculation are well understood so it will not contribute to any systematic error. The *efficiency* correction takes account of both the efficiency of detecting particles in the detector and also the efficiency with which the particle decays are reconstructed by the software. The efficiency correction is not as large as the acceptance and is generally in the range of two to five. However, this correction is more difficult to generate and can more easily contain systematic biases. The extrapolation factor is used to extend a measurement, which has been corrected for acceptance and efficiency, from a limited region of $y - p_t$ phase space to the full phase space.

This correction is necessarily model dependent so discussion is deferred to later (section 5.1). The methods of generating the acceptance and efficiency corrections are described in more detail in the following sections.

4.4.1 Acceptance Calculation

It is necessary to generate a correction factor to take account of those particles which are not reconstructed because either their daughter particles do not traverse the active volume of the VTPCs, or they fail one of the cuts implemented in `v0find` or imposed during the extraction of the data. The distribution in y $-$ p_t phase space of particles emitted in collisions is *a priori* unknown. The proportion of particles falling within the acceptance is a function of this distribution. Therefore, the approach taken was to generate a distribution in y $-$ p_t phase space and produce a correction factor for each bin. There is no requirement to choose the bin size before starting as a smooth distribution is generated. The generated distribution was flat in rapidity. This was achieved by giving each particle a random value of **y** in a chosen range. Each particle is then assigned a value of p_t such that the particles randomly populate a distribution,

$$\frac{dN}{dp_t} \propto p_t \exp \frac{-m_t}{T} \tag{4.4}$$

This method is not the only one that would work, and generating the correction factors on a bin-by-bin basis means that any y$-p_t$ distribution could have been used provided the bin size is sufficiently small that the variation of the distribution across a single bin does not matter. Having been assigned values of **y** and p_t, the particle is given random emission angle consistent with those values. From these variables the momentum components in a Cartesian co-ordinate system are calculated and these are fed into the NA49 implementation of the GEANT program.

4.4.2 GEANT Simulation

The GEANT program [40] propagates the particles through a simulation of the detector system. This simulation is built up of volumes filled with materials accurately matched to the actual experimental setup. Each particle randomly interacts with the material in the simulated volumes according to the known cross-sections. The tracking is performed by using the magnetic field map. Some of the volumes in the simulation are designated as sensitive volumes to correspond with the active volumes of the detectors and simulated particles transported through these volumes leave hits where appropriate, for example, charged particles traversing the TPC active volumes. The position co-ordinates of the hits generated are stored. The level of detail in the simulation can be varied by turning some types of interactions on or off. The simulation was run including multiple scattering, energy loss, and decay of the particles. The particles decay according to the exponential decay law with the lifetimes given in the particle data book [39]. The particles are decayed isotropically in their rest frame. After a particle has decayed, or otherwise interacted, its daughters are followed by the simulation. Tracking ceases when the particle leaves the vicinity of the experiment. Some interactions were not included such as hadronic interactions, bremsstrahlung, Compton scattering and positron annihilation. Inclusion of all effects can lead to a large increase in the processing time for the simulation and this is particularly true if the particles are followed into the dense materials of the magnets and their yokes. The interactions which have been left out of the simulation would mostly occur after the particles had been tracked through the active detectors and their omission has a negligible effect on the acceptance calculation. The particle decay modes are redefined so that the charged decay mode of interest has a branching ratio of 100%. This saves time that would be spent simulating decays of particles that cannot by definition be reconstructed because they have neutral daughters. This well known factor can be explicitly included later using the particle data book values. The more complex drift paths resulting from the $\vec{E} \times \vec{B}$ effect as described in Section 3.2 mean that the charge deposited inside the active volume of the TPC may drift outside. Some hits registered in the simulation may not therefore actually be reconstructable. The converse can also be true and charge deposited in the volume slightly outside that which is directly below the readout plane could drift inwards and be reconstructed. This is due to the way that GEANT generates the hits using a simple projective geometry. It does not follow the drifting charge. The solution adopted was to extend the pad rows in the x-direction which allows extra hits to be generated. A separate program, run after GEANT, moves hits along the drift path using knowledge of the $\vec{E}$ and $\vec{B}$ fields. The hit is placed at a position such that it will be placed on the track when the$\vec{E} \times \vec{B}$ correction is applied, as in the real data. Finally, the program checks which of the generated hits are now actually reconstructable. This final step is part of a program which calculates whether each decay passes the cuts imposed in the treatment of the real data. Particle decays passing all cuts are defined as accepted. The acceptance in a particular bin is defined as the ratio, $\frac{no.accepted}{no.generated}$ in that bin.

Taking K_S^0 decays as an example the acceptance is shown in figure 4.5. It can be seen that the acceptance increases with p_t and covers a broad range of rapidity which corresponds to the rapidities at which VT1 and VT2 have good acceptance.The distribution of *accepted* particles depends on the distribution with which they were generated. A distribution of accepted K_S^0 is shown in figure 4.6. This distribution is clearly double peaked with the peak at higher rapidity corresponding mainly to those detected in VT2 and that at lower rapidity to those found in VT1. The peak is prominent in the figure showing the accepted decays because the acceptance at low p_t is less near mid-rapidity and it is this region of p_t which is much more populated

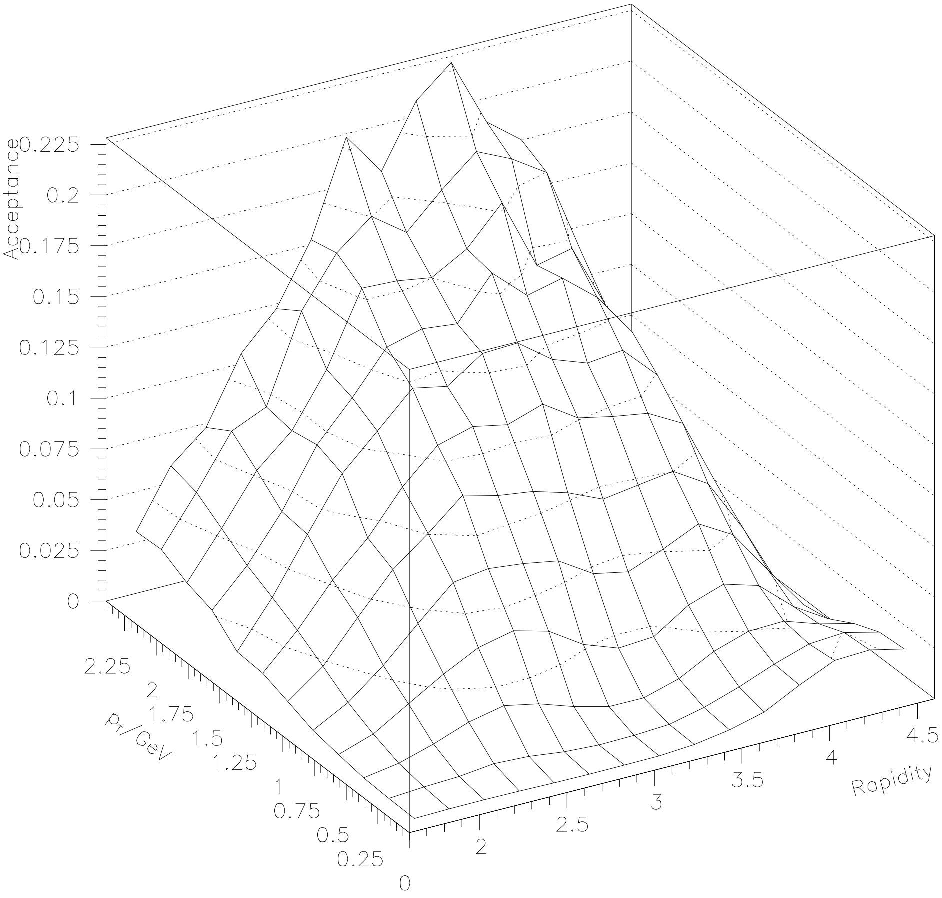

Figure 4.5: The fractional acceptance for K_S^0 decays with a charged final state

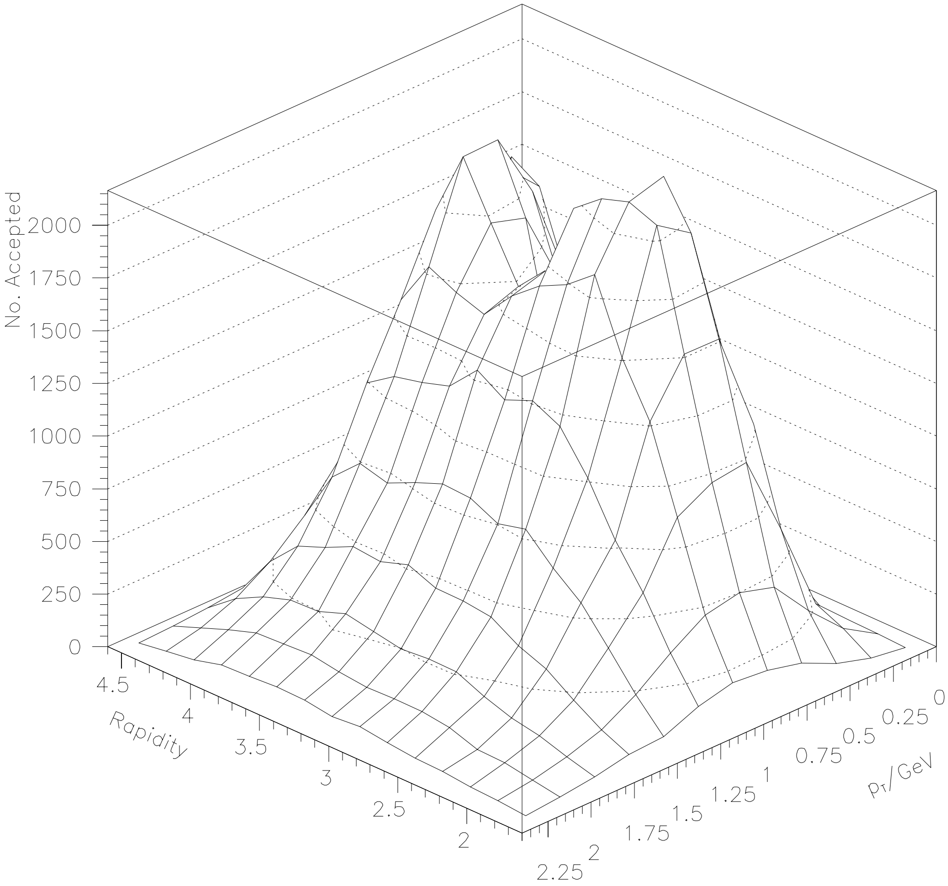

Figure 4.6: The accepted K_S^0 decays from an approximately physical generated $\mathrm{y} - p_t$ distribution. This plot has the axes rotated with respect to the previous plot so that a better view is obtained.

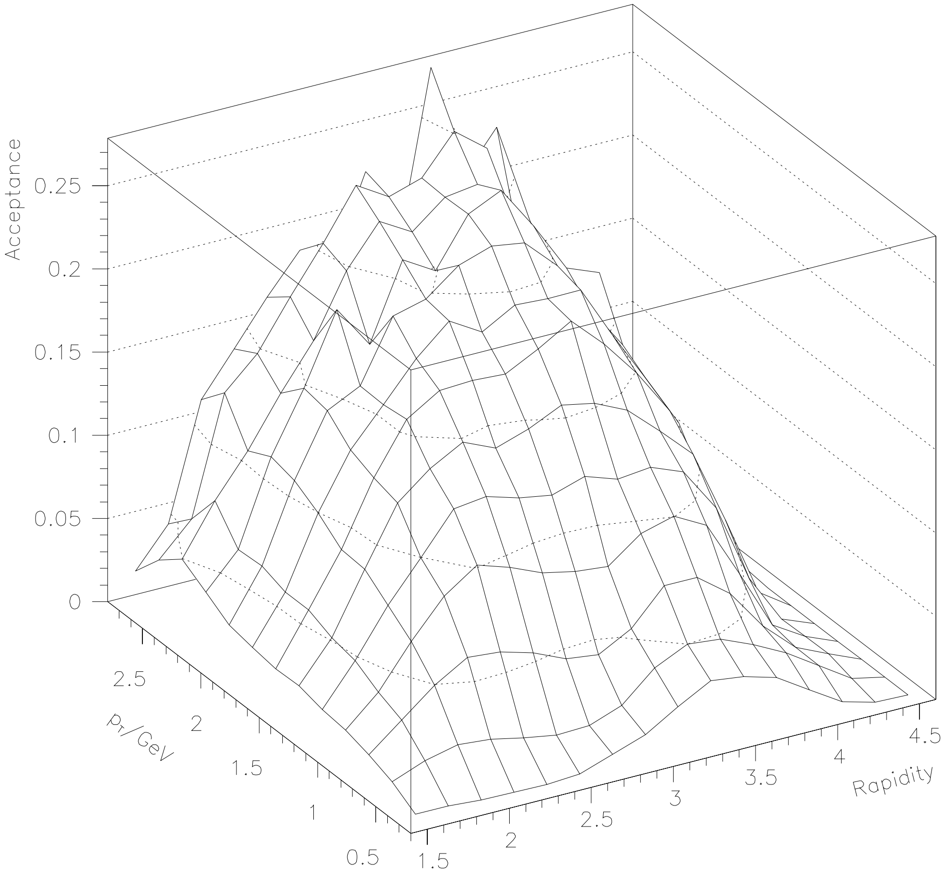

Figure 4.7: The fractional acceptance for Λ decays with a charged final state

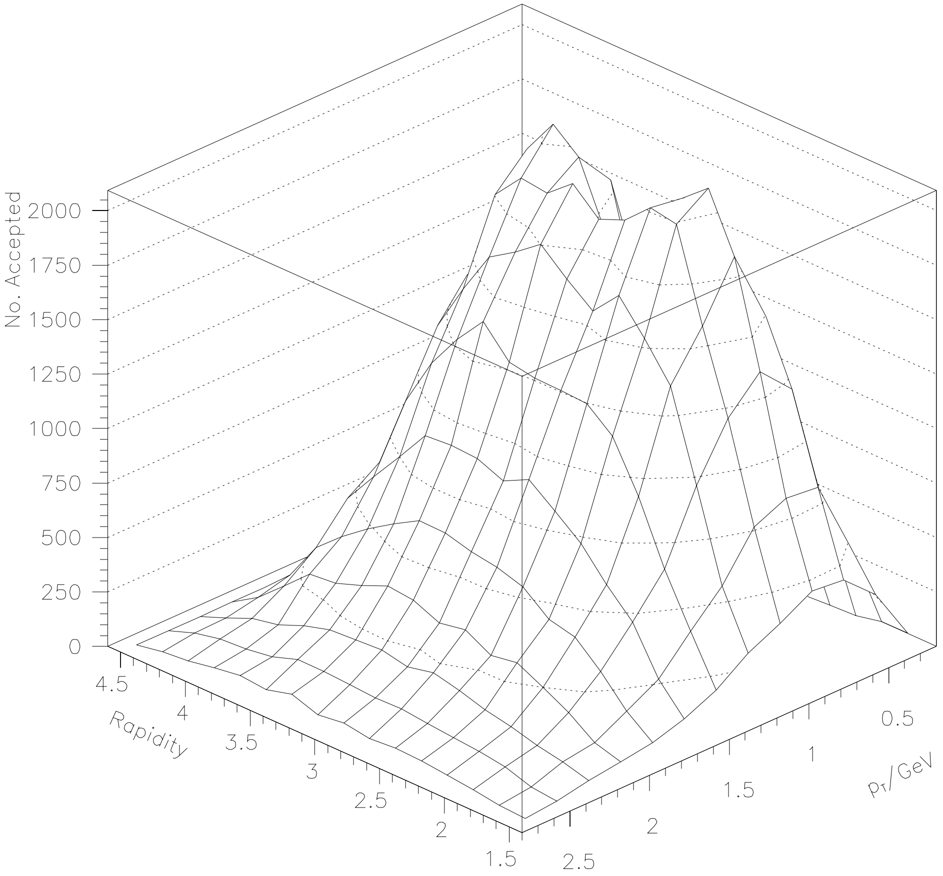

Figure 4.8: The accepted Λ decays from an approximately physical generated $y - p_t$ distribution. The axes are rotated with respect to the previous plot so that a better view is obtained.

by a physical distribution. The particles were generated with a flat rapidity distribution and a p_t distribution satisfying equation 4.4, with an inverse slope parameter of $T = 250$ MeV, as an approximation to the physical distribution. The value of T was chosen as a result of earlier work [31] which found this value. The value chosen does not affect the result of the acceptance calculation as it just controls the number of generated particles appearing in each bin and this number divides out when the ratio is taken.

The acceptance for Λ is shown in figure 4.7 and the distribution of accepted Λ is shown in figure 4.8. The latter figure uses the same approximation to the physical distribution as was used for K_S^0 except that an inverse slope parameter, $T = 280$ MeV was used. The symmetry of the detectors is such that plots of the same quantities for $\overline{\Lambda}$ look very similar.

4.4.3 Efficiency Correction

A correction factor must also be generated so that proper account is taken of those decays which were not reconstructed even though they fall within the cut and detector acceptance. These are decays for which at least one of the daughter tracks was not found or was mis-reconstructed so that the decay vertex could not be found. This correction is termed the reconstruction *efficiency* correction. The correction should by design take account of all the possible sources of inefficiency and it is therefore important to simulate the environment. The chosen method is called *embedding* and it involves implanting MC decays into real events and running the reconstruction code. The advantage of this is that there is no need to simulate the tracking environment from scratch because the real one can be used. The procedure comprises several stages. The MC data associated with accepted particle decays must be filtered off and a simulation performed so that it is converted into mock raw data i.e. ADC counts. This mock raw data must then be mixed in with the raw data from a real event. This step needs to take appropriate account of the saturation effect (see section 3.2) as it is one source of inefficiency. Finally, the new hybrid event is given to the reconstruction chain. This should take account of any inefficiencies in the various programs in the reconstruction chain. After this has been repeated a larger number of times the V0s in the output distribution are compared to the input distribution to find out the probability of their being found and thus the efficiency.

As in the case of the acceptance correction it is anticipated that the efficiency will be a function of both y and p_t. An efficiency correction was therefore generated on a bin-by-bin basis.

4.4.4 Simulation and Embedding Procedures

As described in section 4.4.2 the simulated tracks which cross the sensitive volumes are assigned hits. The GEANT simulation is able to calculate an energy loss associated with each hit and it would be possible to produce simulated raw data from this. However, this would not achieve the desired result because this takes no account of the detector response. It is necessary to produce simulated data with clusters of different size and shape in order to mimic the real data. The detector simulation produces simulated raw data which depend explicitly on the angle with which the track crosses the pad and the drift length which a hit would have.

The simulated raw data are implanted into the actual raw data from an event. Checks are made to ensure that data are not embedded into regions of the TPCs where saturation of the preamps has occurred in that event. Again, this is to ensure that the simulated data are treated in the same way as real data. This process accounts for inefficiencies due to a daughter track not being found because one, or more likely several, of its hits were in a region of the TPC where no hits can be reconstructed in that event. This can result in the track being either too short to pass the minimum number of points cut, by virtue of not having those hits, or not found as a track at all. In either case the decay cannot be reconstructed.

In order to perform these embedding runs the software reconstruction chain was assembled on some of the Nuclear Group computing facilities in Birmingham. The data from several thousand raw events were also copied and brought to Birmingham. The reconstruction chain was run on a computer FARM consisting of ten single processor machines.

For the sake of simplicity only those events in which no candidates, consistent with the particle being embedded, were found are used. An event list is constructed by counting the number of candidates for each event in the mass interval spanning both the peak and background regions of the invariant mass spectra as listed in table 4.2. The event list contains the number of Λ, $\overline{\Lambda}$ and K^0_S in each event. When embedding Λ, only events where the number of real Λ equal zero are used and similarly for $\overline{\Lambda}$ and K^0_S. This enables the assumption to be made that those V0s which are reconstructed correspond to the ones that were embedded because there is no contamination from the real V0s in the events. The fraction of events available for embedding are 51%, 58% and 80% for Λ, K^0_S and $\overline{\Lambda}$ respectively.

Embedded distributions The particles used for embedding are those which are accepted but the definition of what is accepted is extended slightly by the loosening of some cuts. This is to avoid any bias caused by mis-reconstruction. For example, an MC particle decaying at a z position of -345 cm may be reconstructed with a decay vertex of -355 cm and thereby be cut out. However, an MC particle decaying at z=-355 cm would not have the chance to be reconstructed on the allowed side of the cut because it does not fall within the acceptance and would not be embedded. Mis-reconstruction would therefore introduce a bias towards measuring a lower efficiency. The cuts which are opened up in the acceptance calculation and their values are summarized in table 4.3.

Name	effective reconstruction cut	cut for embedding
ϕ angle	$0.2 <\|\phi\|< 2.9$	cut removed
$x_+ - x_-$ VT1	5 cm	3 cm
$x_+ - x_-$ VT2	2 cm	0 cm
minimum z VT1	-555 cm	-535 cm
minimum z VT2	-350 cm	-370 cm

Table 4.3: Cuts modified in selection of candidates for embedding.

The first column lists the cuts applied in the reconstruction and the second the relaxed value. Other cuts which are used in the reconstruction do not need to be relaxed because they do not apply to the MC data anyway. These are the DCA and the V0 impact parameter with the target which are always zero in the MC. A choice must be made as to what region of y $- p_t$ phase space MC particles are generated over so that corrections may be produced. Several factors influence this choice and the final correction procedure will be described in more detail in 4.6. Whatever range is desired for producing the final corrected data, it is necessary to generate and embed particles encompassing this range *and* also include one y and one p_t bin on either side. This is again done to avoid the introduction of a bias due to the MC particles being reconstructed with a different y or p_t. The magnitude of this effect was studied in earlier work [31] and it was found that it was sufficient to use one extra y and p_t bin on either side for bin sizes of 0.2 units of y and 0.2 GeV/c in p_t.

Another property which can be varied is the number of particles which are embedded into each raw event. The safest solution is to embed only one simulated decay per event as this has the least perturbation to the event and therefore the least effect on the environment, which is what causes the inefficiency. However, the embedding process is quite time-consuming, since the whole event has to be reconstructed. Even when nine processors are being used it takes over two days to embed into and process all of the events available for Λ embedding (a total of 5366). It is necessary to have a large amount of reconstructed embedded data, such that the contribution to the statistical error from the embedding is similar to or smaller than that from the real data. If only one particle per event had been embedded it can be estimated that embedding would have taken around three months for Λ only so the safest solution was not a practical one and it was necessary to embed more than one particle per event.

The optimum solution is to embed as many as is possible without, changing the characteristics of the event and causing a change in the efficiency measured. An investigation into finding the optimum number was done by doubling the number embedded and looking for a change in the calculated efficiency. A long study could not be performed due to restrictions on time. A test with different numbers of particles was tried. A population of K_S^0 was generated in the rapidity interval 1.6 to 4.8 and p_t interval 0 to 2.6 GeV/c using an exponential $m-T$ distribution with an inverse slope of 250 MeV. This population has an average acceptance of around 4% so generating 100 particles per event resulted in the mean number of particles being embedded into each event being 4.32 and, as would be expected, generating 200 particles per event results in an average of 8.64 decays being embedded. Thirteen thousand events were processed in the first mode and just under seventeen thousand in the second. The results of an efficiency calculation where the efficiency is calculated in rapidity bins with a cut on p_t is shown in figure 4.9. This shows that there is no observable systematic difference between the efficiency calculated from runs with the different numbers of K_S^0 embedded and the observed differences are within the statistical uncertainty of a few per cent. It was concluded that it is safe to embed around 8 per event and this is why more events were processed in the second mode. For Λ the mean number of particles embedded was

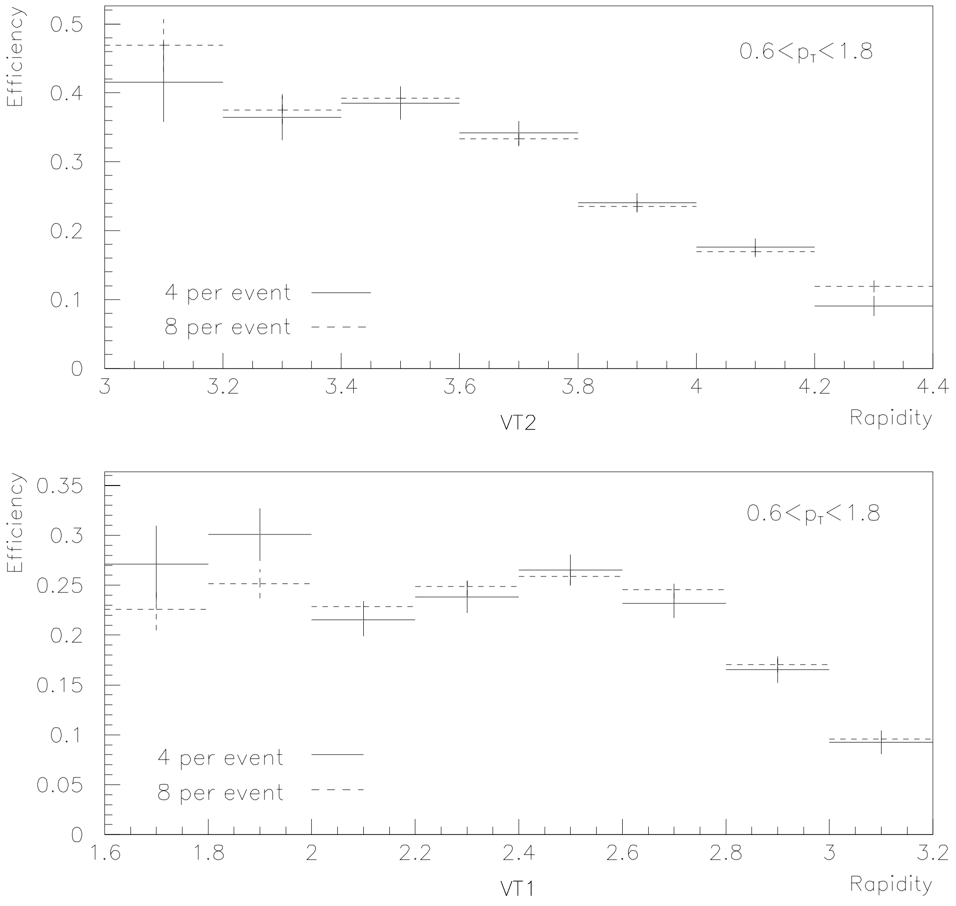

Figure 4.9: The efficiency as a function of rapidity in a p_t window for different mean numbers of K_S^0 embedded per event.

between eight and nine and for $\overline{\Lambda}$ just over ten per event were embedded after initially starting with five and looking for a change in the same way as was done for K_S^0. The calculated efficiencies for K_S^0 fall off as a function of rapidity going towards high rapidity for both VTPCs. This behaviour is observed for Λ and $\overline{\Lambda}$ also. The overall magnitude of the efficiency is rather higher for VT2 than VT1. The efficiency reaches 40% for VT2 but only around 25% in VT1. As a function of p_t, efficiencies rise going from low to high p_t. The efficiency can be plotted as a function of p_t in various rapidity bins for each V0 particle type. Figure 4.10 shows the efficiency for K_S^0 in six rapidity bins of size 0.2 units of y from 3.0 to 4.2. In general the efficiency does not seem to be a strong function of p_t.

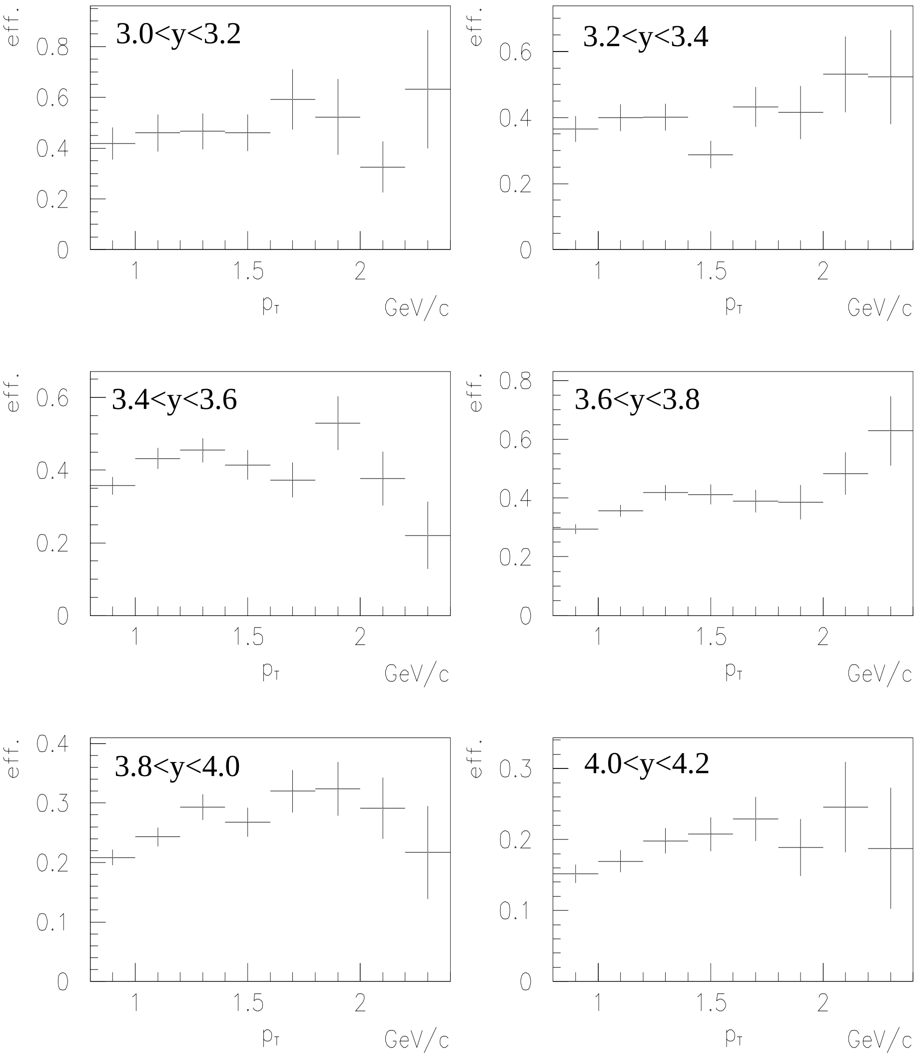

Figure 4.10: The K_S^0 efficiency as a function of p_t in six rapidity bins in the interval $3.0 < \mathbf{y} < 4.2$. The upper left plot is the lowest rapidity bin.

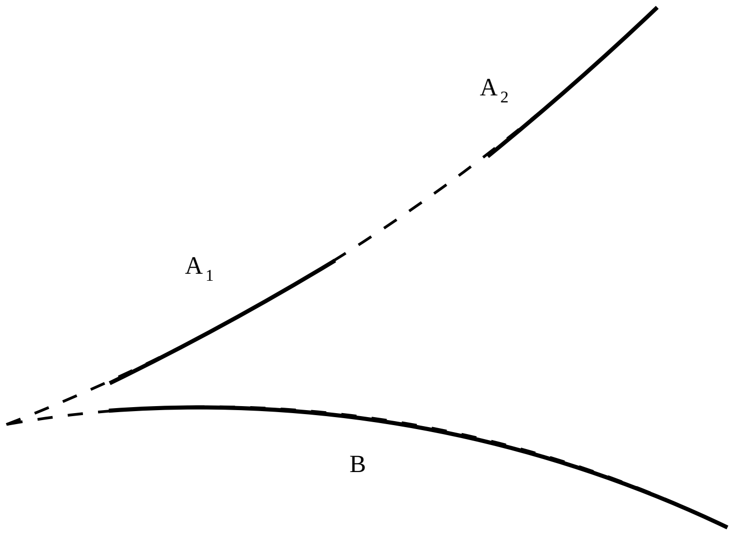

Figure 4.11: Split track, A, causing double counting of V0s.

4.4.5 Double Counting

There exists the possibility of a particular decay being counted twice because one of the daughter tracks is reconstructed in two pieces. This is illustrated in figure 4.11. Here the negative track is reconstructed in one piece, labelled B but the positive track is reconstructed twice (A_1 and A_2). It is thus possible for a V0 candidate to be formed by the track combinations A_1B and A_2B. Since the efficiency calculation is designed to reproduce the conditions in the real data, cases of double counting should be present in both the reconstructed embedded MC data and the real reconstructed data in the same proportion. The efficiency correction would then correctly take account of this. However, if the reason for the track splitting is not known then there is the possibility of the efficiency correction not working as it should. In order to see whether this is potentially important it would be good to have an estimate of the amount of double counting present in the data. This has been done using a relative 4-momenta analysis, as described below. An analysis looking at the frequency of finding N candidates in an event, consistent with being a Λ, and modelling them with a Poisson distribution gave a similar estimate for the double counting but it involves some additional assumptions.

$\mathbf{Q_{inv}}$ analysis The relative 4-momenta of pairs of V0 candidates can be calculated and the resulting distributions examined. The idea is that double counting causes an excess of pairs with low relative 4-momenta compared to a reference distribution of pairs of V0s taken from *different* events. The relative 4-momentum, Q_{inv} is calculated according to equation 4.5.

$$Q^2_{inv} = \Delta E^2 - \Delta p_x^2 - \Delta p_y^2 - \Delta p_z^2 \tag{4.5}$$

In this equation ΔE is the difference in energy and Δp_i is the difference in the p_i component of momentum. The Q_{inv} was calculated for all pairs of candidates in the real data consistent with being a Λ. Cuts were applied limiting the calculation to the area of $y - p_t$ phase space for which the data are corrected. There are a total of around 40000 candidates, of which around 20$\%$ are background. The reference distribution was for pairs with the same cuts. The distributions are shown in figure 4.12.

The peak at low Q_{inv} is clearly visible. By subtracting the mixed event distribution,[1] suitably weighted, the number of excess pairs at low Q_{inv} can be estimated. This is about 1200 which is only 3$\%$ of the total number of Λ candidates. This is not actually the best estimate for double counting but is an upper limit since the excess pairs also include pairs of Λ candidates which share one track derived from the same particle track but use two entirely unrelated other tracks. These pairs are simply a real Λ with a combi-

---

[1] This is similar to the experimental technique for constructing the correlation function which is the first step in extracting the source radii via the HBT effect. The correlation function is constructed by *dividing* the real and mixed event pair distributions after ensuring that there are no tracks counted twice. There were not enough events available to do this for Λ and K^0_S.

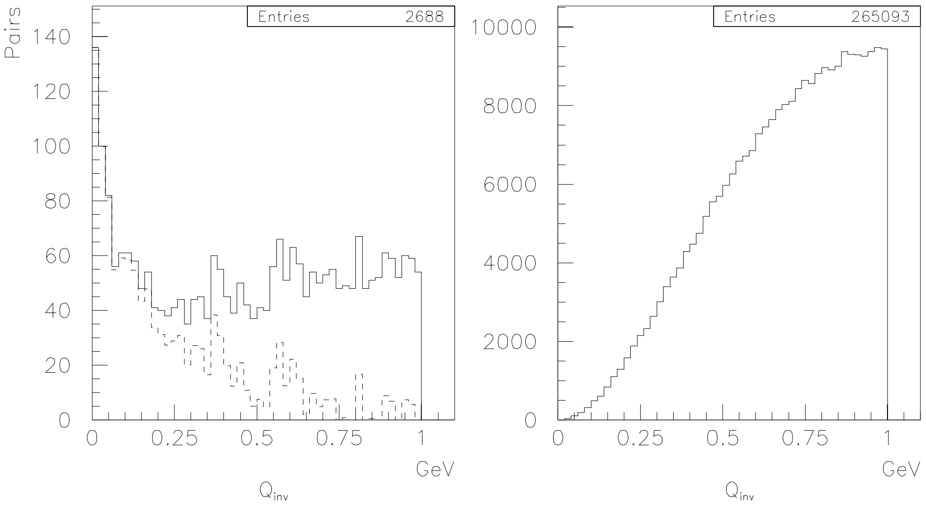

Figure 4.12: The Q_{inv} distributions for real pairs (left) and mixed event pairs (right) with the real pairs remaining (dashed line on left) after subtracting a normalized distribution of mixed pairs.

natorial background candidate. It is not possible to know which is which on an individual basis but further, more detailed, analysis can improve the limit on double counts further. A similar percentage of double counts is observed in the reconstructed MC data so the effect is small and it should anyway be taken care of by the efficiency calculation. For these reasons no explicit correction was introduced to correct for double counting. The exercise was repeated for K_S^0 and similar results were obtained.

4.5 Feeddown Correction

Contained in the data are Λ and $\overline{\Lambda}$ which are non-primary particles. These are the daughter particles from the weak decay of multi-strange baryons. The decays $\Xi^- \rightarrow \Lambda\pi^-$ and $\Xi^0 \rightarrow \Lambda\pi^0$ contribute to this and each has a branching ratio of almost 100%. There is also a contribution from $\Omega^- \rightarrow \Lambda K^-$ which has a 68% branching ratio. The charge conjugate anti-particle decays contribute to the feeddown into $\overline{\Lambda}$. There is no feeddown into K^0_S except from charmed mesons and this is extremely small and so neglected.

An explicit correction is required to subtract these from the data because they should not be part of the final measured distribution. The contribution that they make to the final distributions depends on the geometry of the experiment, so to leave them in would make comparisons difficult. Λ and $\overline{\Lambda}$ are also produced in the decay of Σ baryons but these are either short lived and essentially decay at the target (Σ^0), or have such small branching ratios to Λ that they can be ignored ($\Sigma^{\pm}$). For the decay of Σ producing Λ at the target, all experiments see the same thing so results for Λ production are taken to include these.

The procedure adopted is to generate a y $- p_t$ distribution of Λ from Ξ^- and Ξ^0 decays, the feeddown distribution, and subtract this, suitably weighted, from the y$-p_t$ distribution in the actual data before it is subject to the acceptance and efficiency corrections. To generate the feeddown distribution Ξ^- and Ξ^0 are passed through the simulation chain in the same way that V0s were for the efficiency calculation. Approximations to the physical distributions of Ξ^- and Ξ^0 are required as a start point. Ξ^- have been measured in Pb-Pb collisions [41] so the parameterization was taken from this measurement and a y $- p_t$ distribution generated with a Gaussian rapidity profile of with $\sigma = 1$ unit of rapidity and an inverse slope parameter of 300 MeV. The normalization of 7.5 Ξ^- per event was also taken from [41]. It was further assumed that the Ξ^0 follow this parameterization and normalization. It could be argued that there are fewer Ξ^0 on the grounds that they contain uss quarks as opposed to the dss quark content of Ξ^- due to there being more $d-$quarks from the isospin asymmetry of the initial nuclei but this will be a small effect and is neglected. The Ξ^- and Ξ^0 are decayed by the GEANT program and the accepted Λ from these decays filtered off. These Λ are then embedded into the real data and the reconstructed Λ extracted. The effect of the feeddown correction will be demonstrated in the next section.

4.6 Production of corrected distributions

All of the components now exist for the production of the final corrected y and p_t distributions of Λ, $\overline{\Lambda}$ and K^0_S. A correction factor is calculated for each bin using the acceptance and efficiency corrections and is applied to the background subtracted data in that bin.

4.6.1 Rapidity distributions

A rapidity distribution can be produced by summing the $\mathrm{y} - p_t$ bins within a particular rapidity bin provided that the same p_t range is used for each y bin. This has been done for K^0_S using a common p_t range of $0.8 < p_t < 1.8$ GeV/c in the rapidity interval $1.8 < \mathrm{y} < 4.4$ with the result shown in figure 4.13.

The points derived from data processed as VT1 candidates and that processed as VT2 candidates are shown using different symbols. Near to mid-rapidity there is an overlap of several rapidity bins in the acceptance for each detector. However, this corresponds to the edge of the acceptance where there is the possibility of the corrections being less reliable. The acceptance of VT1 at lower p_t drops off sharply beyond mid-rapidity. The reason for keeping the VT1 and VT2 data separate is to avoid contaminating good data with less reliable data. It is possible to make use of the symmetry of the collision system and reflect the points around the mid-rapidity point at 2.9 units of rapidity. This has been done and these points are denoted by open symbols. The error bars are removed from the open symbols

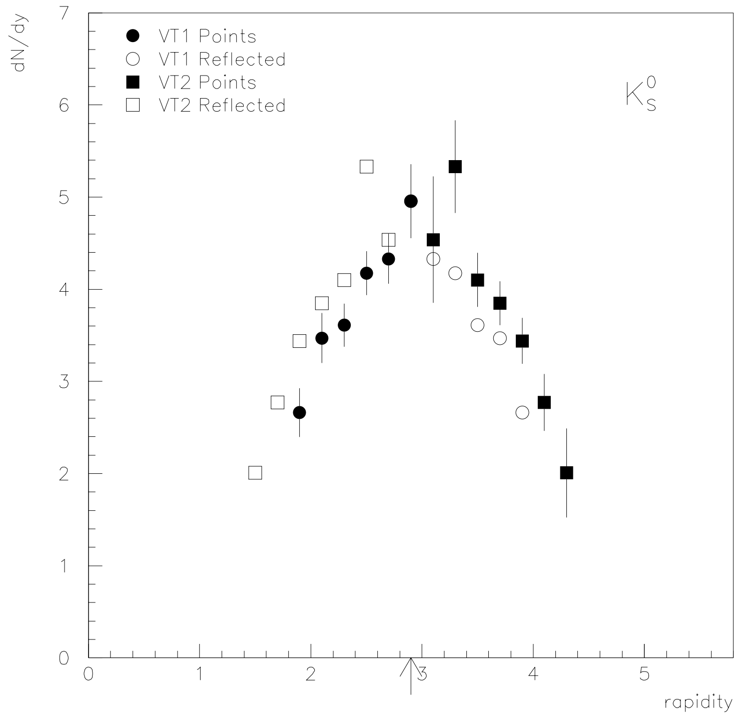

Figure 4.13: Rapidity distribution of K^0_S measured in the p_t range $0.8 < p_t < 1.8$ GeV/c. Measured (filled symbols) and reflected (open symbols) points are shown. The reflection is around mid-rapidity, marked with an arrow.

for clarity. It is fairly obvious that VT1 points lie systematically lower than the VT2 points and reasons for this are explored in the discussion (section 5.2).

The rapidity distribution for Λ in the p_t interval $1.0 < p_t < 2.2$ GeV/c was calculated in the same manner and is shown in figure 4.14. The same convention for labelling the points is used. This distribution does not contain the correction for feeddown from Ξ. Points are shown over the interval $1.8 < \mathbf{y} < 4.2$. For $\overline{\Lambda}$ the procedure is repeated with the same p_t range being summed as for Λ but a reduced rapidity interval of $2.0 < \mathbf{y} < 4.0$ due

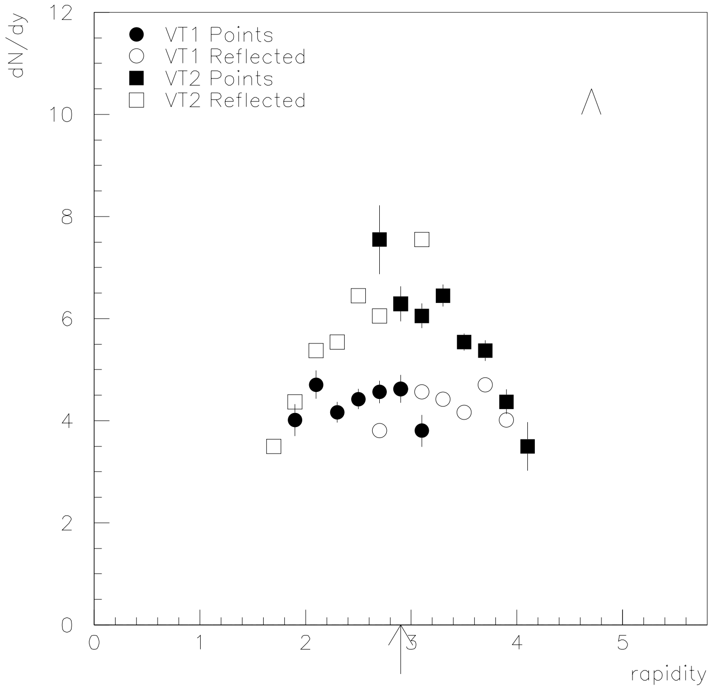

Figure 4.14: Rapidity distribution of Λ measured in the p_t range $1.0 < p_t < 2.2$ GeV/c. Measured (filled symbols) and reflected (open symbols) points are shown. The reflection is around mid-rapidity, marked with an arrow.

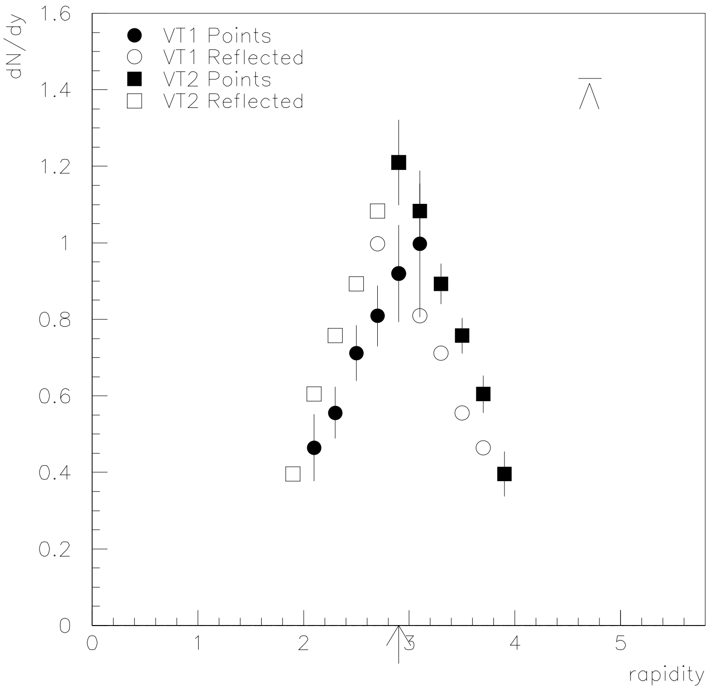

Figure 4.15: Rapidity distribution of $\overline{\Lambda}$ measured in the p_t range $1.0 < p_t < 2.2$ GeV/c. Measured (filled symbols) and reflected (open symbols) points are shown. The reflection is around mid-rapidity, marked with an arrow.

to the smaller number of $\overline{\Lambda}$. This distribution is shown in figure 4.15 and again does not include a feeddown correction.

For the Λ and $\overline{\Lambda}$ distributions an additional cut on the z-position of the decay vertex for VT1 candidates was imposed. This had a value of -500 cm. It was found that there is a source of background which appears to be asymmetric around the mass peak which meant that too many counts were subtracted from under the mass peak. It particularly affects the rapidity distribution around $y = 2.3$ and it may be associated with the ceramic posts at the front of the VTPC1 detector. A tightening of the z-cut seems to improve the situation. The effect on the invariant mass spectrum of $\overline{\Lambda}$, for which the effect is proportionately bigger, is shown in figure 4.16.

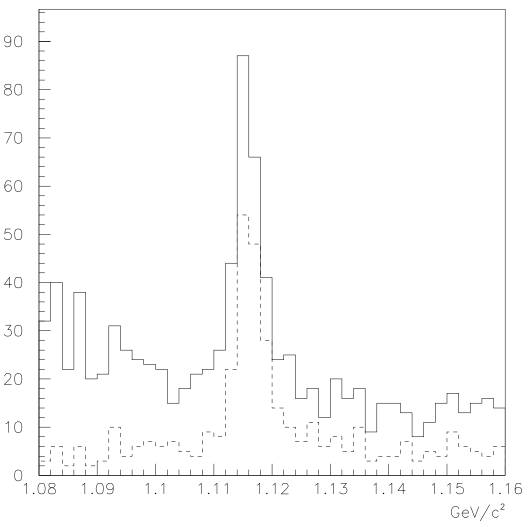

Figure 4.16: Invariant mass spectrum for $\overline{\Lambda}$ in the interval $2.2 < \mathbf{y} < 2.4$ with a z_{vertex} cut at -500 cm (dashed line) and without cut (solid line)

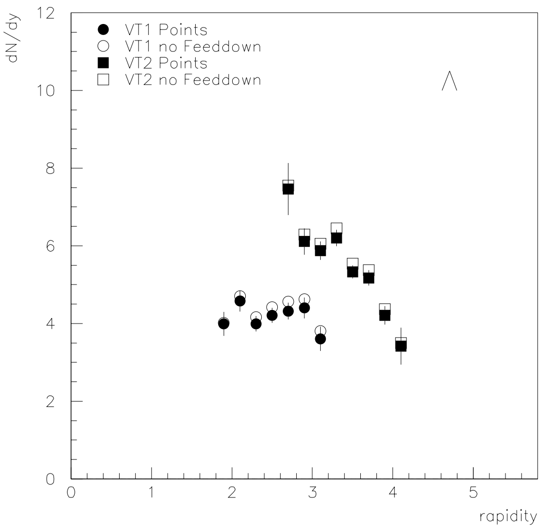

Figure 4.17: The effect of the feeddown correction on the rapidity distribution of Λ in the range $1.0 < p_t < 2.2 GeV/c$

Effect of feeddown correction. The calculated feeddown correction contains the number of Ξ^- and Ξ^0 expected in the data sample in each bin. This is then subtracted from the data before the acceptance and efficiency corrections are applied. A comparison of the Λ rapidity distribution is shown in figure 4.17.

4.6.2 Transverse momentum distributions

The p_t distribution is constructed by plotting the corrected y$-p_t$ bins which lie in the same rapidity bin. Therefore, a p_t distribution can be made for each point in the rapidity distributions shown in figures 4.13 - 4.15. Since there is no longer a need to use the same p_t interval in each rapidity bin, points at a lower p_t may be included for some bins.

The experimental distribution, having been appropriately divided by the bin sizes, corresponds to $\frac{d^2N}{d\mathbf{y}dp_t}$, the double differential cross section. In order to fit the individual p_t spectra in each rapidity bin a functional form for the distribution is required. The starting point is the invariant cross section, which can be written in terms of momentum components $p_{||}$ and p_t, parallel and perpendicular to the longitudinal direction respectively,

$$E\frac{d^3\sigma}{dp^3} = \frac{Ed^2\sigma}{2\pi p_t dp_t dp_{||}} \tag{4.6}$$

This can be written in terms of $\frac{dN}{d\mathbf{y}}$, the multiplicity per unit rapidity giving,

$$E\frac{d^3\sigma}{dp^3} = const.\frac{d^2N}{p_t d\mathbf{y} dp_t} \tag{4.7}$$

where the constant terms have been amalgamated. Integrating using a dynamical model over the longitudinal direction [42] gives,

$$\frac{1}{p_t}\frac{dN}{dp_t} = const.m_t K\left(-\frac{m_t}{T}\right) \tag{4.8}$$

where K is the modified Bessel function. This is then approximated to

$$\frac{dN}{dp_t} = A.p_t \exp -\frac{(p_t^2+m_0^2)^{\frac{1}{2}}}{T} \tag{4.9}$$

where a factor $m_t^{\frac{1}{2}}$ has been neglected in addition to the substitution for K which is valid when $\frac{m_t}{T} \gg 1$. A is simply a multiplicative constant and m_0 is the rest mass of the particle.

Fits were tried using this equation with A and T as the two parameters. This proved to be unsatisfactory as the values of T fluctuate from one rapidity bin to the next. This behaviour is unphysical since, even if T is not constant across the measured rapidity interval it should vary in a smooth fashion. The reason for this behaviour is that the two parameters are highly correlated as can be deduced from the error matrix. The two parameter fit can well describe the p_t distribution but the individual parameters do not seem well constrained. One way around this is to fix the integral of the function to the sum of the data in the measured p_t interval which is done by re-writing the multiplicative constant, A, in terms of this sum. Equation 4.9 can be integrated analytically. The integral between $p_t = p_{t(a)}$ and $p_t = p_{t(b)}$, denoted by N_{ab} is given by,

$$N_{ab} = AT(\exp - \frac{m_{t(a)}}{T}(m_{t(a)} + T) - \exp - \frac{m_{t(b)}}{T}(m_{t(b)} + T)) \qquad (4.10)$$

where ${m_{t(i)}}^2 = {p_{t(i)}}^2 + m_0^2$. Equating N_{ab} with S_{ab}, the sum of the measured data between $p_t = p_{t(a)}$ and $p_t = p_{t(b)}$, allows A to be written in terms of S_{ab} and T only. This is then substituted in to equation 4.9 which is used for a one parameter fit.

Fits to the K_S^0 p_t spectra for each rapidity bin from VT1 are shown in figure 4.18. The fits for the VT2 rapidity points are in figure 4.19. The range over which the fit is performed along with the value of the inverse slope parameter and its error, obtained from the fit are printed on each panel, as are the rapidity bin limits.

The values obtained for the inverse slopes are shown in figure 4.24 where they are plotted against rapidity. In the VT2 bins they are all consistent with a value around 235 MeV and there is no evidence of a systematic trend in the fitted values of T. Those values obtained from the VT1 bins are systematically higher and some are above the range of accepted values from previous measurements as well as being in disagreement with the respective reflected bin from VT2. This points to some kind of systematic problem. To have this effect the problem would have to make the p_t spectra flat so that a higher inverse slope is obtained. For instance, an underestimation of the efficiency at high p_t pushing up these corrected points and the opposite of this, an overestimation of the efficiency going towards lower p_t, would both cause a flattening of the spectra.

The p_t spectra for Λ have also been fitted in the same way. The spectra include the feeddown correction and the VT1 spectra include the additional cut on the z position of the vertex as before. Those derived from the

VT1 data are in figure 4.20 and those from VT2 in figure 4.21. Again, the values extracted from the fit can be seen in figure 4.24. As in the case of K_S^0 the fits in VT2 are consistent with a common temperature, whereas in VT1 there is a larger spread in the values obtained.

Finally, the $\overline{\Lambda}$ plots are shown in figure 4.22 for VT1 and figure 4.23 for VT2. The fits to the $\overline{\Lambda}$ spectra suffer from the smaller number of counts available. Additionally, there may be some kind of systematic problem for the VT1 fits towards mid-rapidity as the fitted value of T obtained does not agree with other measurements. The values obtained from VT2 data are all consistent with a single value.

The overall picture is that, for each particle species separately, the fits to VT2 data provide evidence favouring a single inverse slope parameter which describes the p_t spectra at all rapidities within the range covered by the measurement.

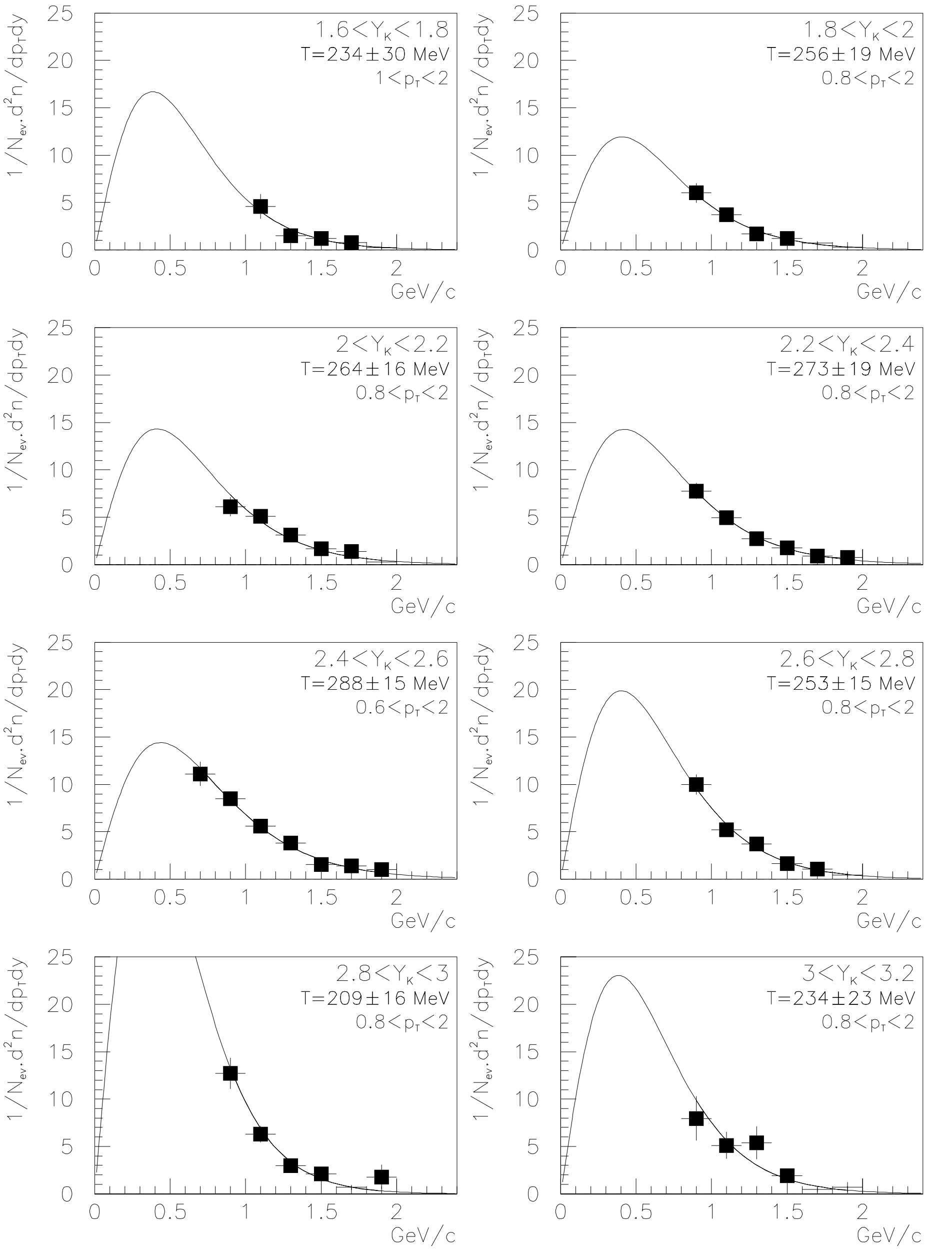

Figure 4.18: K_S^0 p_t spectra in the VT1 rapidity bins

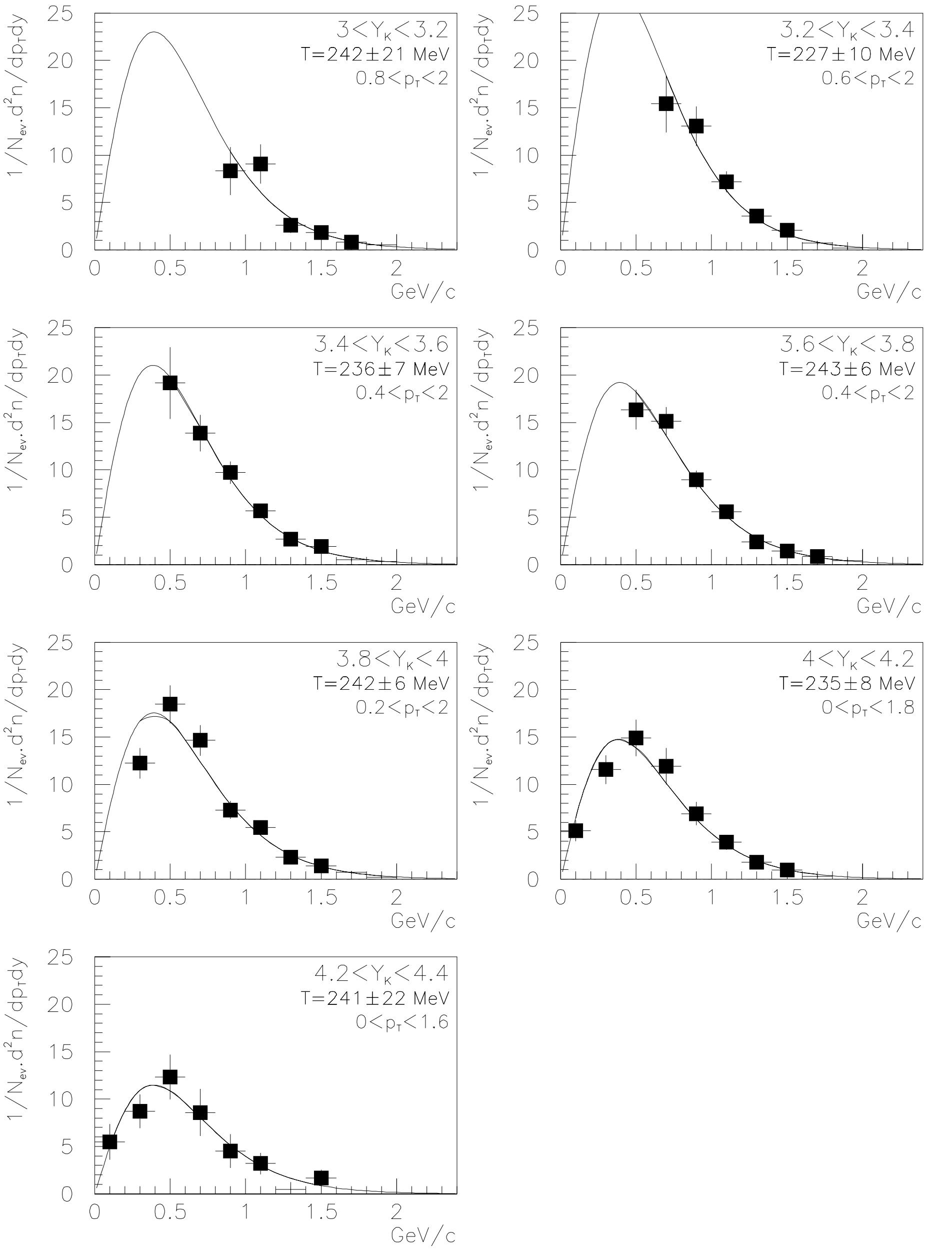

Figure 4.19: K_S^0 p_t spectra in the VT2 rapidity bins

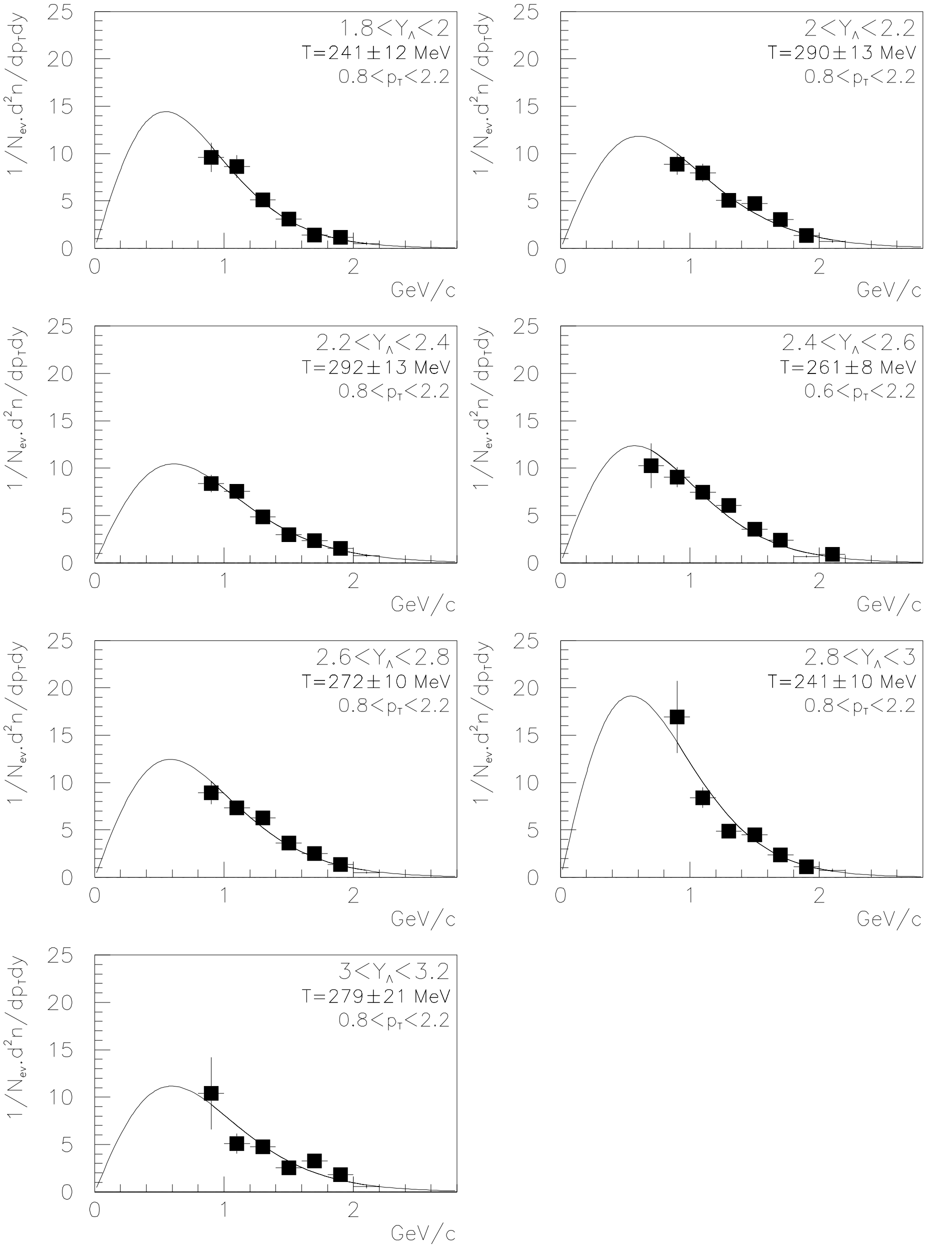

Figure 4.20: Λ p_t spectra in the VT1 rapidity bins

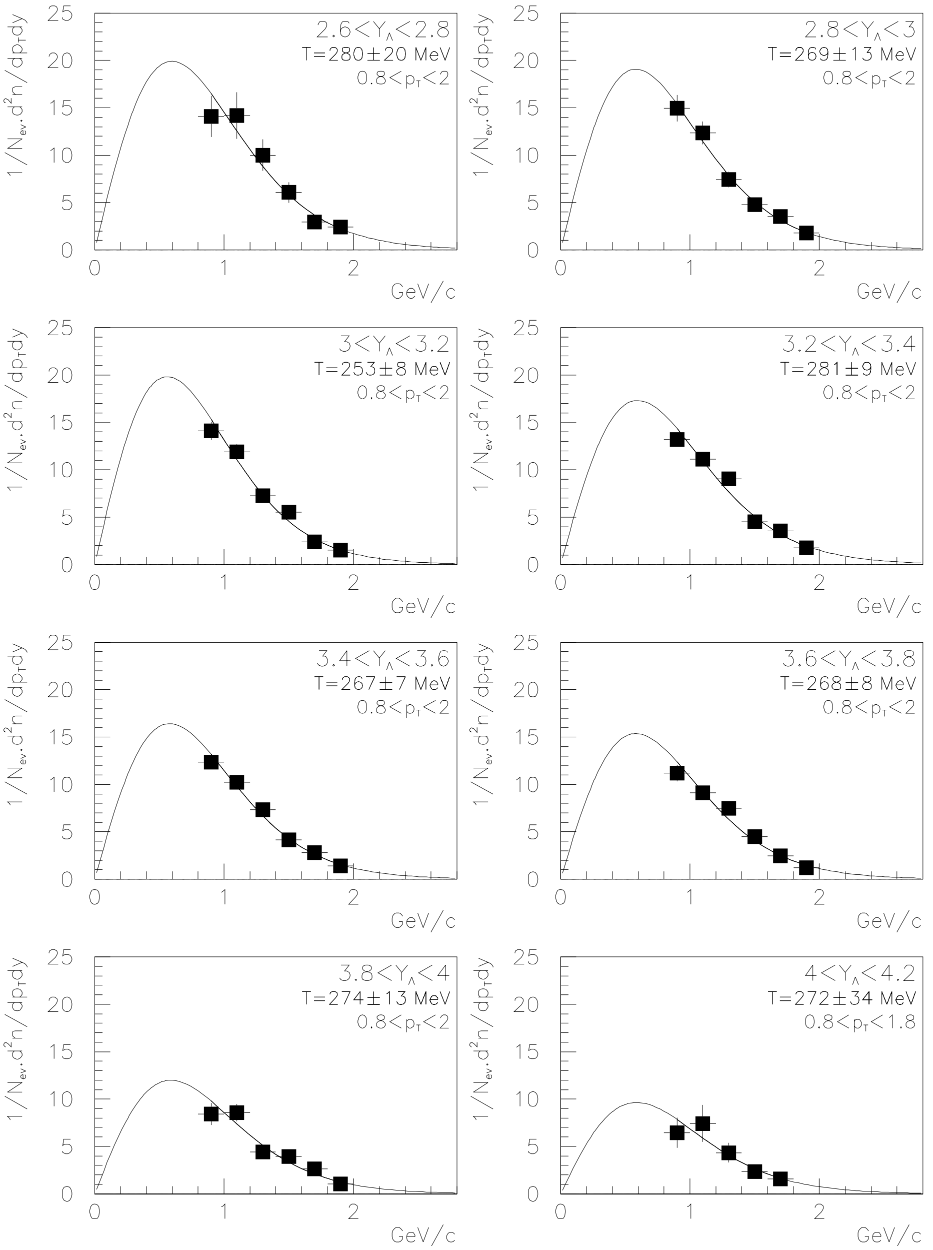

Figure 4.21: Λ p_t spectra in the VT2 rapidity bins

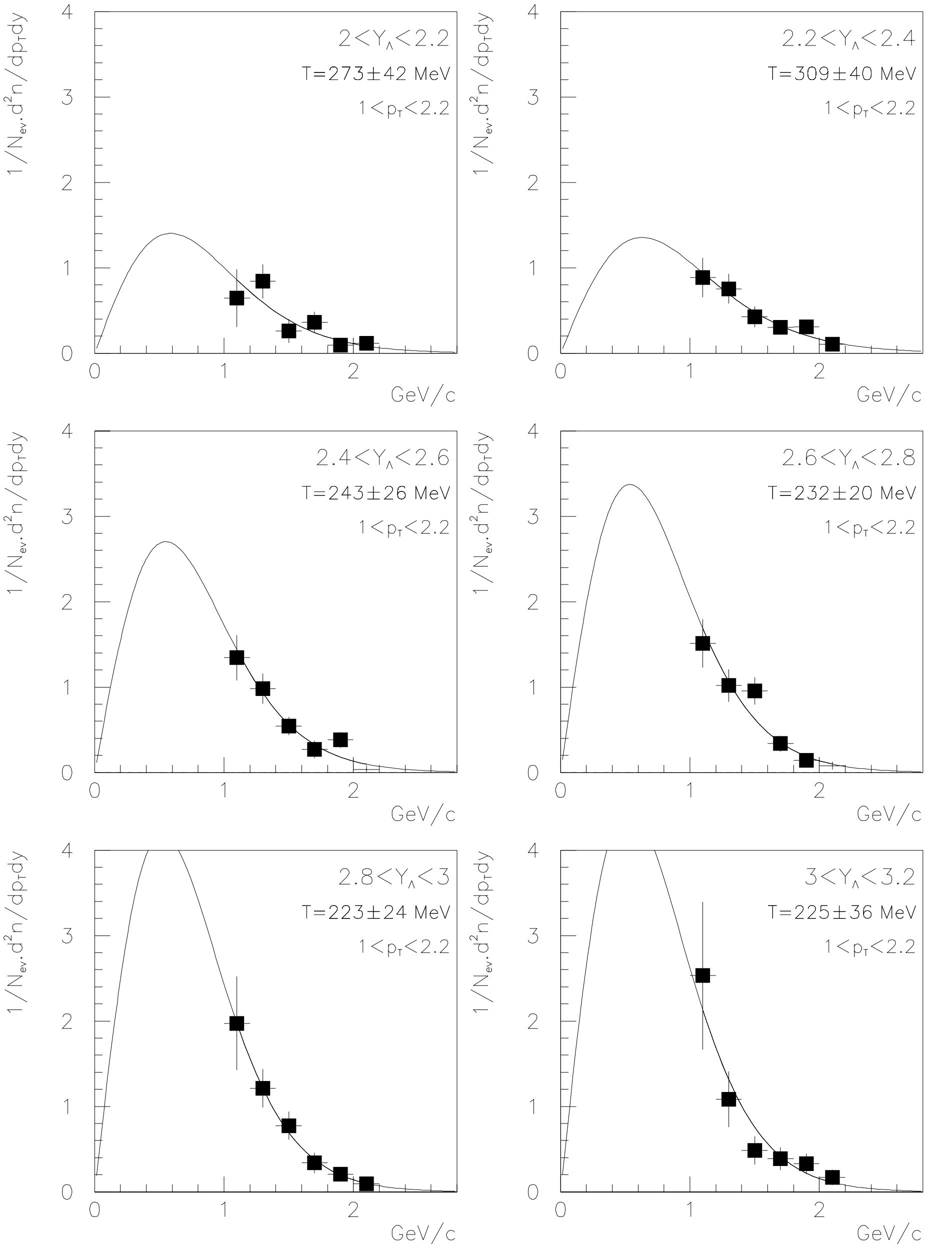

Figure 4.22: $\overline{\Lambda}$ p_t spectra in the VT1 rapidity bins

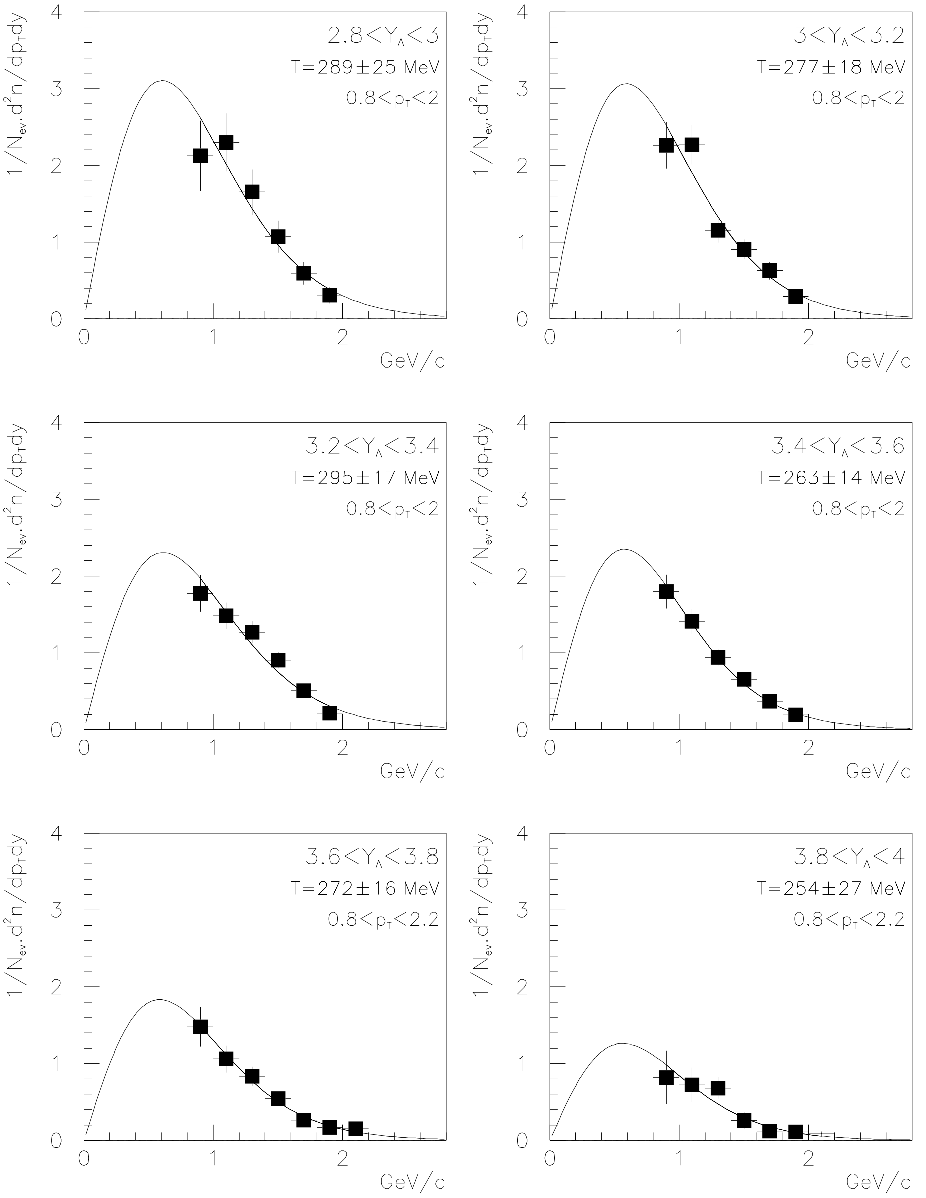

Figure 4.23: $\overline{\Lambda}$ p_t spectra in the VT2 rapidity bins

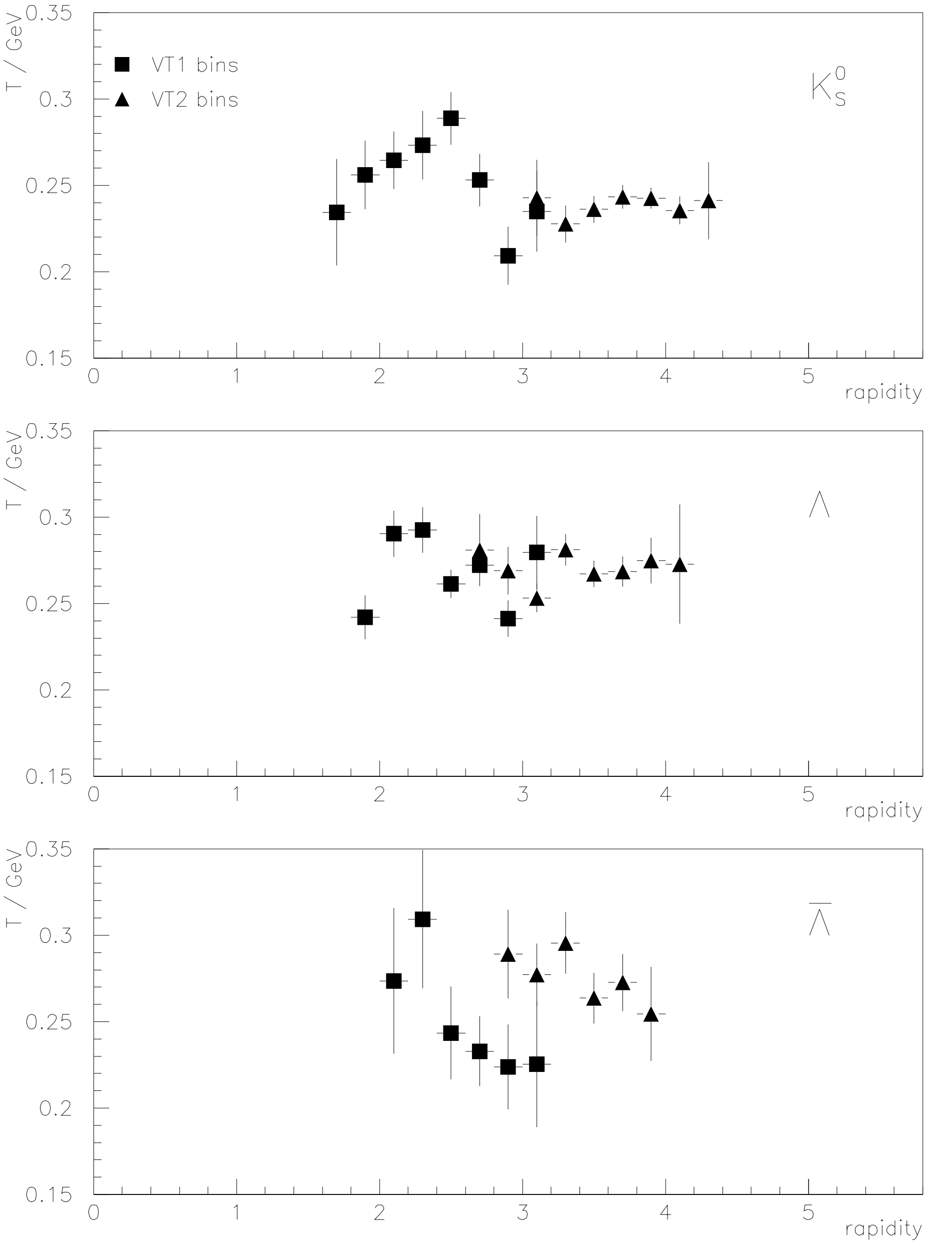

Figure 4.24: The fitted values of the inverse slope, T, obtained in each rapidity bin for K_S^0, Λ and $\overline{\Lambda}$.

4.7 Summary of Corrections

In summary, the data presented are acceptance and efficiency corrected. The acceptance correction factor although large is well known and calculated by standard techniques. The efficiency correction factor is smaller than that for the acceptance but is more vulnerable to systematic effects. The efficiency calculation attempts to include all known effects to minimize this. The contribution from decays which count twice was investigated and found to be negligible. Also, a feeddown correction was calculated and, although it was found to be small, has been applied to the data.

Chapter 5

Discussion and Conclusion

In this chapter the results are extrapolated from the limited region of phase space in which the measurement is made. An assessment is made of the reliability of the results obtained by investigating the systematic errors. The results are then compared with others from the strange particle sector in Pb+Pb at 158 GeV, and also those at other energies and from other systems. Trends in the data are identified and commented upon. To conclude, some of the future directions of the work, within the NA49 experiment and the CERN Heavy-Ion Program and at other facilities, are summarized.

5.1 Extrapolation

The measurements of the production of Λ, $\overline{\Lambda}$ and K^0_S are made in a limited region of phase space and it is necessary to be able to estimate the total number of each species produced in collisions by extrapolating to the full phase space. This allows comparisons with models and other experiments which might make measurements in a different region of $\mathrm{y}-p_t$ phase space. Such extrapolations are necessarily model dependent, so care should be taken with the conclusions drawn from such extrapolated results.

Particle	T (MeV)	y range	p_t range
Λ	274±5	3.2-3.8	0.8-2.0 GeV
$\overline{\Lambda}$	279±10	3.2-3.8	0.8-2.0 GeV
K^0_S	238±5	3.2-3.8	0.6-2.0 GeV

Table 5.1: Fitted inverse slope parameters used for extrapolation to full p_t and the range over which the fit was performed.

5.1.1 Extrapolation in p_t.

Each rapidity point, which represents the number measured in that rapidity bin over a limited range of p_t, can be extrapolated over the full p_t range by assuming a p_t distribution. If the distribution is assumed to be that used to extract the inverse slope parameter in equation 4.9 it can be integrated analytically. The ratio between the integral over the measured and full ranges can be found and used as a scale factor for each rapidity point. In this way the best use can be made of the available data as there is no restriction to using a rectangular area of y$-p_t$ phase space. This has been done by calculating the scale factor for each point but making the assumption that the inverse slope is the same for the p_t distribution in each rapidity bin. The inverse slope used is found by fitting the p_t distribution over a rapidity interval corresponding to three y bins in the middle of the VT2 acceptance in order to get the best possible estimate for T. The values obtained and used are shown in table 5.1. Using this method rapidity distributions are obtained for K^0_S (figure 5.1), Λ (figure 5.2) and $\overline{\Lambda}$ (figure 5.3).

5.1.2 Extrapolation in rapidity.

For the extrapolation from the measured rapidity interval to full rapidity it is less obvious how to proceed. A commonly used method is to fit a Gaussian to the rapidity distribution. For the distributions obtained this may be

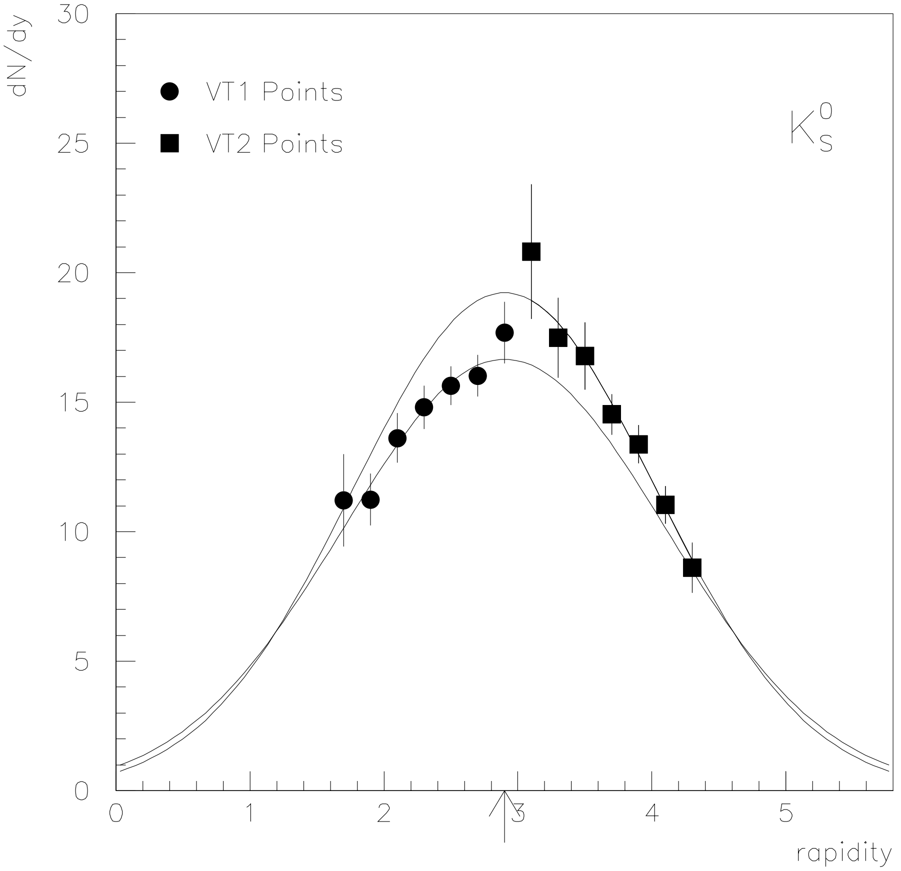

Figure 5.1: Rapidity distribution for K_S^0 extrapolated to full p_t. A Gaussian has been fitted to each set of points.

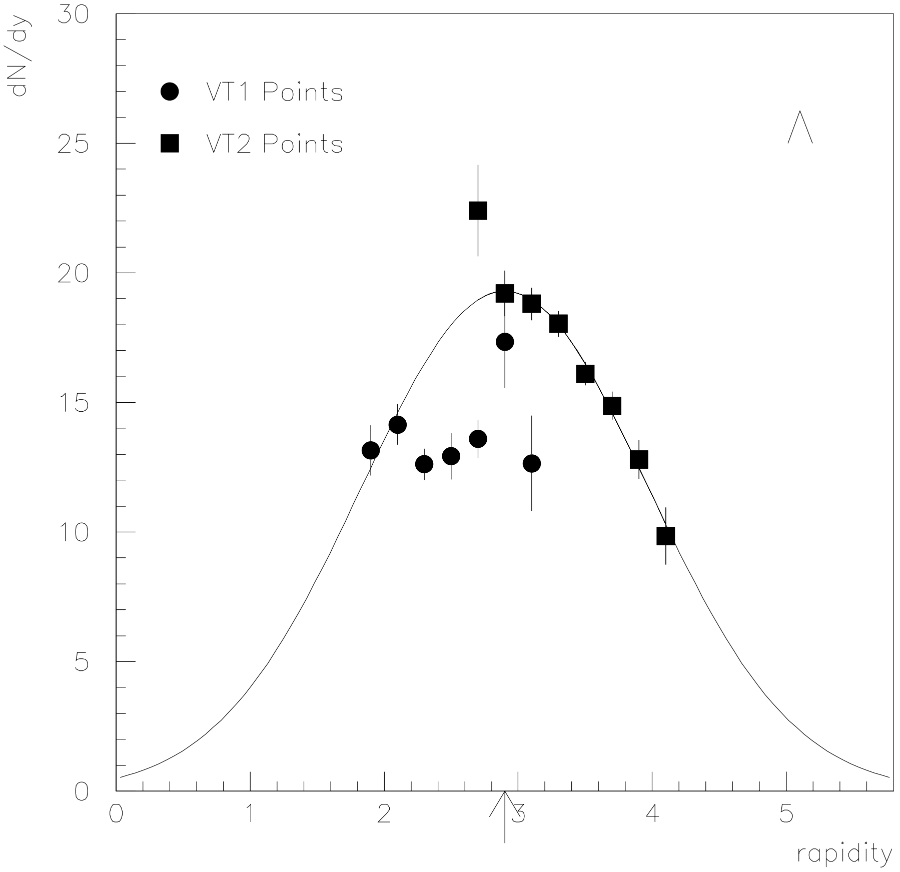

Figure 5.2: Rapidity distribution for Λ extrapolated to full p_t. A Gaussian has been fitted to the VT2 points.

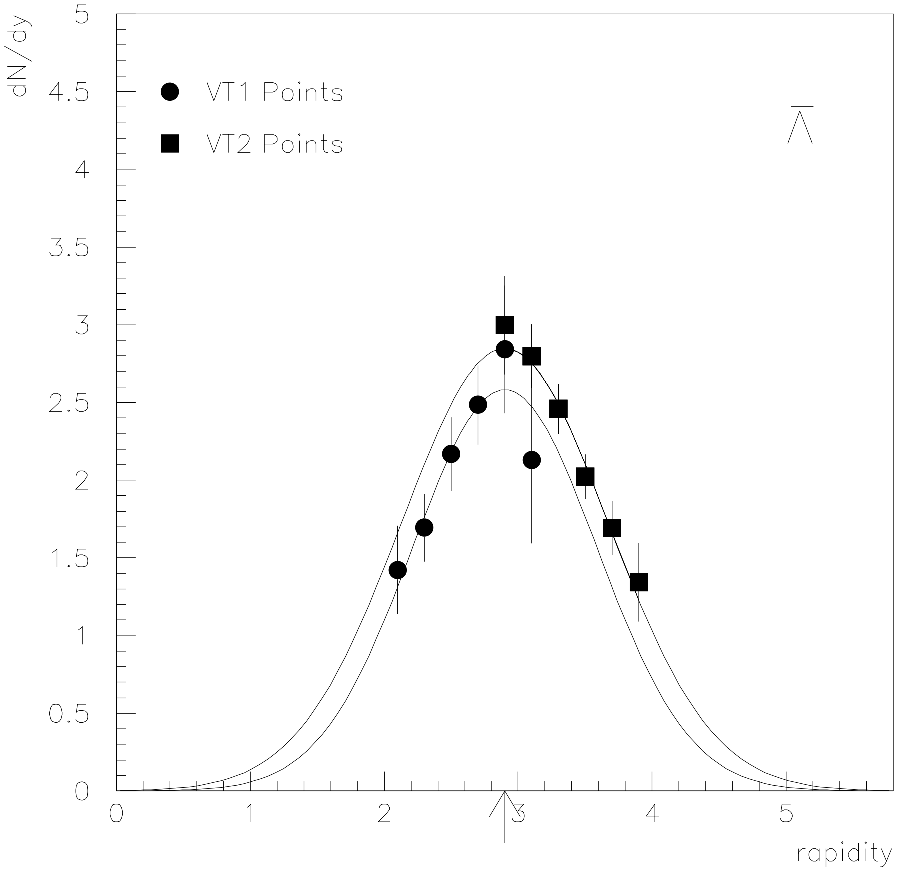

Figure 5.3: Rapidity distribution for $\overline{\Lambda}$ extrapolated to full p_t. A Gaussian has been fitted to both sets of points.

Particle	Detector	σ (units of rapidity)	Peak Value	Yield
K_S^0	VT2	1.13±0.08	19.2±1.0	54±5
K_S^0	VT1	1.21±0.13	16.7±0.6	50±6
Λ	VT2	1.07±0.06	19.3±0.4	52±3
$\overline{\Lambda}$	VT2	0.77±0.07	2.85±0.15	5.5±0.6
$\overline{\Lambda}$	VT1	0.69±0.10	2.58±0.20	4.5±0.8

Table 5.2: Yields of particles obtained by integration of Gaussian fits to the rapidity distributions along with the fit parameters.

appropriate in the cases of K_S^0 and $\overline{\Lambda}$. For Λ this does not seem suitable for two reasons. Only one of the distributions obtained, that from VT2, could be described as peaked. Also, the Λ rapidity distribution might be expected to follow the distribution of the nucleons as it shares a ud quark pair with them. The net proton distribution has been measured [43] and it is a broad distribution which is fairly flat over three units of rapidity with a slight dip at mid-rapidity. This leads to the expectation of a similar distribution for $\Lambda - \overline{\Lambda}$ which would mean that the Λ distribution would have to be approximately flat. This resembles the Λ rapidity distribution obtained from VT1 rather than that obtained from VT2. The Gaussian fits are shown on figures 5.1, 5.2 and 5.3. Where possible the separate fits to VT1 and VT2 points are shown which highlights the systematic difference between them. The numerical results of the fits are summarized in table 5.2. The Gaussian fit to the peaked Λ distribution obtained in VT2 is shown as it appears to be quite a good fit. The reason for the discrepancy between the VT1 and VT2 measurements is not clear. In order to try to reveal the reasons for the difference some systematic studies were undertaken and are described in the next section.

5.2 Systematics

Several consistency checks were performed with the aim of highlighting any systematic problem in either the data or the simulation process. Certain distributions were compared for the real and simulated data to see if they are the same. The most useful of these was the number of points found on tracks. The stability of the final corrected results against various cuts was also tested to check that there was no dependence or bias introduced.

5.2.1 Numbers of points on tracks

A test is performed on the number of points on the tracks in the reconstructed simulated data and the real data, as they ought to be the same. It is important that they are they same because there is a cut made such that daughter tracks must have 20 or more points. The most important requirement is that the proportion failing this cut is the same for real data and reconstructed MC data. However, only those candidates with more than 20 points are found so this cannot easily be checked directly. Instead, the number of points distributions above the cut are compared and it is hypothesized that if they follow one another closely in the region above 20 then they will also follow each other below 20 and hence the proportion passing the cut will be the same in each case.

The number of points on the positive and negative daughters are plotted separately because, in the case of Λ and $\overline{\Lambda}$, they have rather different distributions. The plots are also made separately for VT1 and VT2 candidates. In each plot the real data is represented by a solid line and the reconstructed MC data by a dashed line. The histograms for the real and reconstructed MC data are normalized to an arbitrary number so that the distributions may be compared without the additional complication of having a different number of entries in each. The vertical scale is therefore arbitrary as indicated on the plot. Each distribution is corrected for the contribution from background by plotting the histograms using the cuts on invariant mass, indicated in table 4.2, and subtracting them as appropriate.

The plots in figure 5.4 for K_S^0 in VT2 show quite good agreement between data and MC although the positive tracks have slightly more hits on average in the MC. The agreement for negative daughters is slightly better than for the positive daughters. The VT1 plots for K_S^0 in figure 5.5 show that the simulation appears to produce tracks which are on average slightly longer than those in the real data. This indicates that these tracks are easier to find and consequently the calculated efficiency may be too high. The end result of this is that the final distribution is systematically lower. This is consistent with what is observed for the corrected distributions in figure 4.13 where the VT1 distribution lies below that from VT2.

It may be that there are small discrepancies because the distributions are averaged over y $-p_t$. Track length is a function of these kinematic variables so any differences in the input y $-p_t$ distributions may show up. More importantly, it may be that the simulation does not reproduce all of the details. The simulated clusters being too big or not diffusing in the same way as in the data could lead to more of them being found and so to longer tracks. This kind of problem would be dependent on where the drift length of the tracks in the TPC and would show up as a y-dependence. The VT1 tracks are shorter than the VT2 tracks so the 20 point cut is cutting out a larger fraction of the candidates which means that if this is not simulated correctly it leads to a larger systematic error for VT1 than for VT2. An estimate of the systematic error can be made by finding an approximate shape for each number of points distribution and seeing what level of adjustment is necessary for the means of the distributions to match up. For VT1 this means a reduction in the positive track point positive distribution to 92$\%$ and the negative track distribution to around 94$\%$ which, taken together, would re-

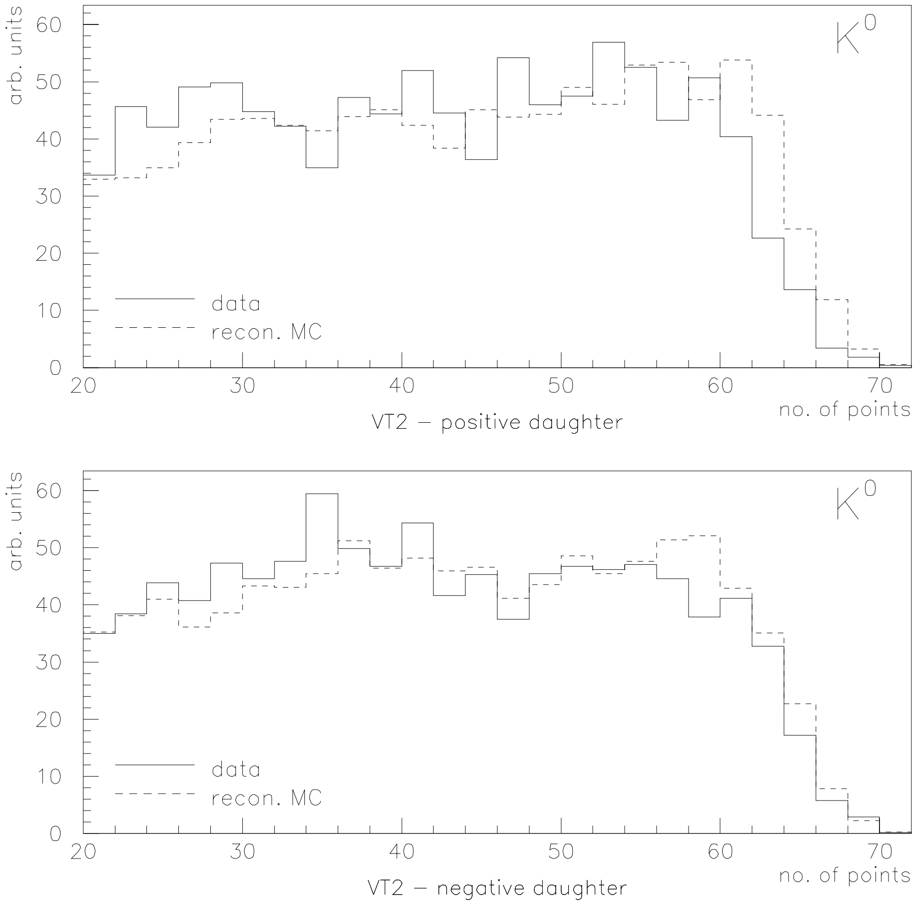

Figure 5.4: The number of points on K_S^0 daughter tracks in VT2 for real and reconstructed MC data.

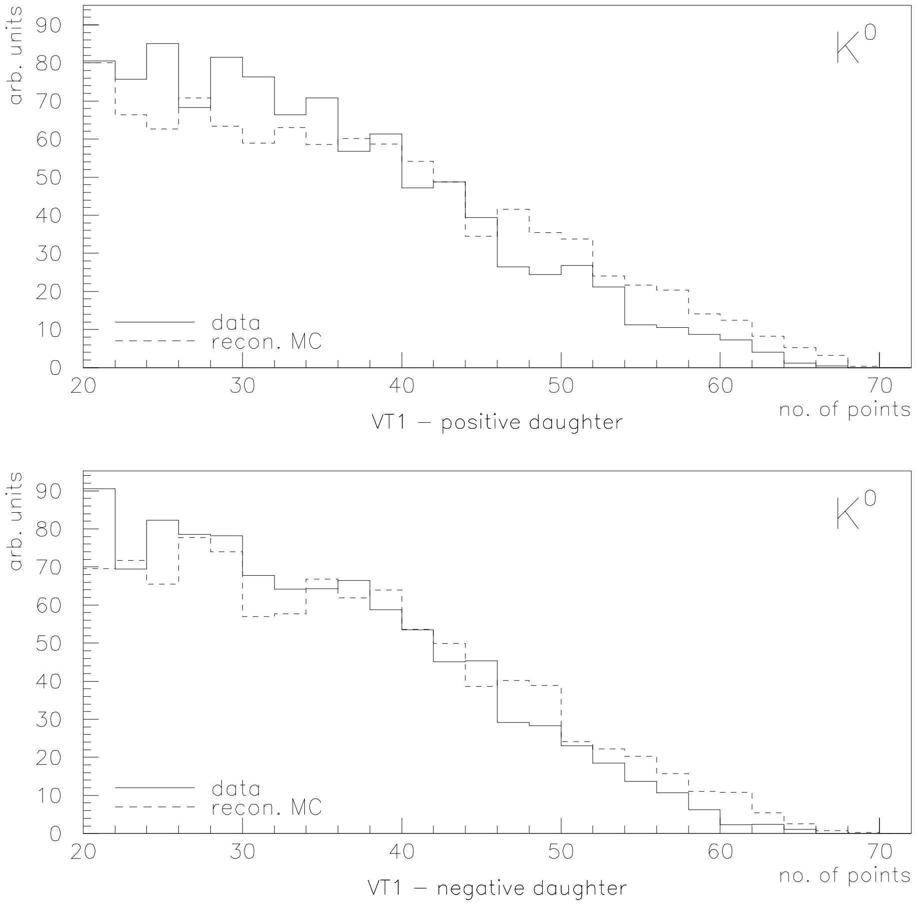

Figure 5.5: The number of points on K_S^0 daughter tracks in VT1 for real and reconstructed MC data.

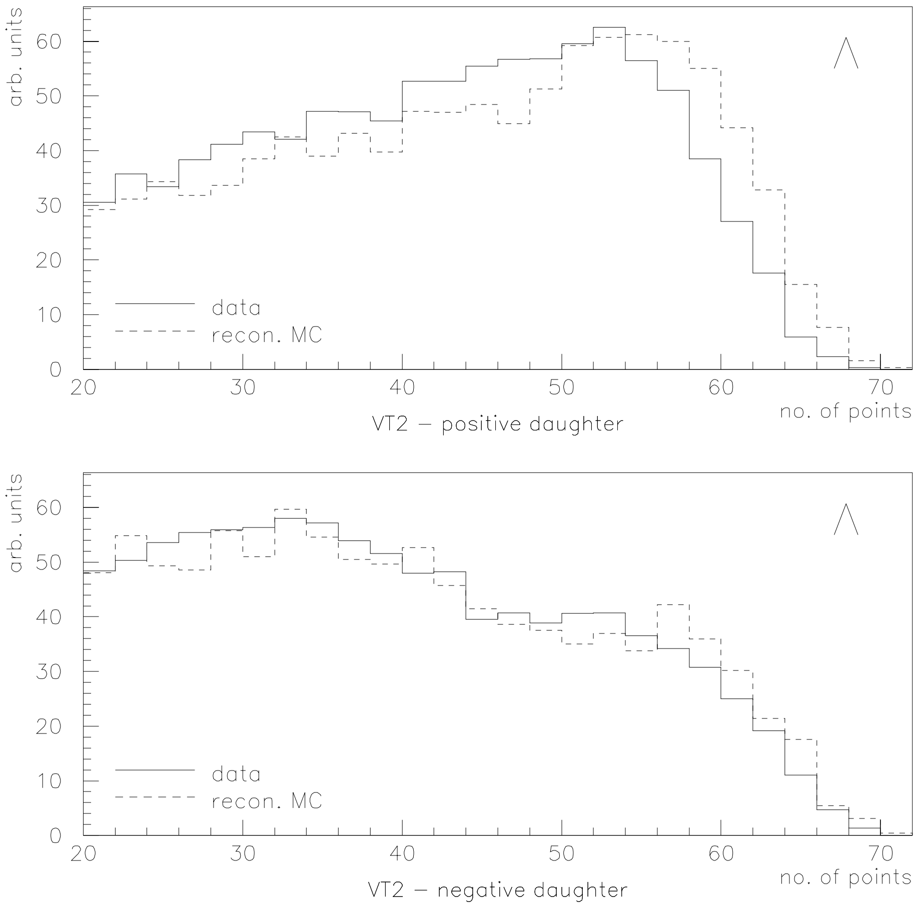

Figure 5.6: The number of points on Λ daughter tracks in VT2 for real and reconstructed MC data.

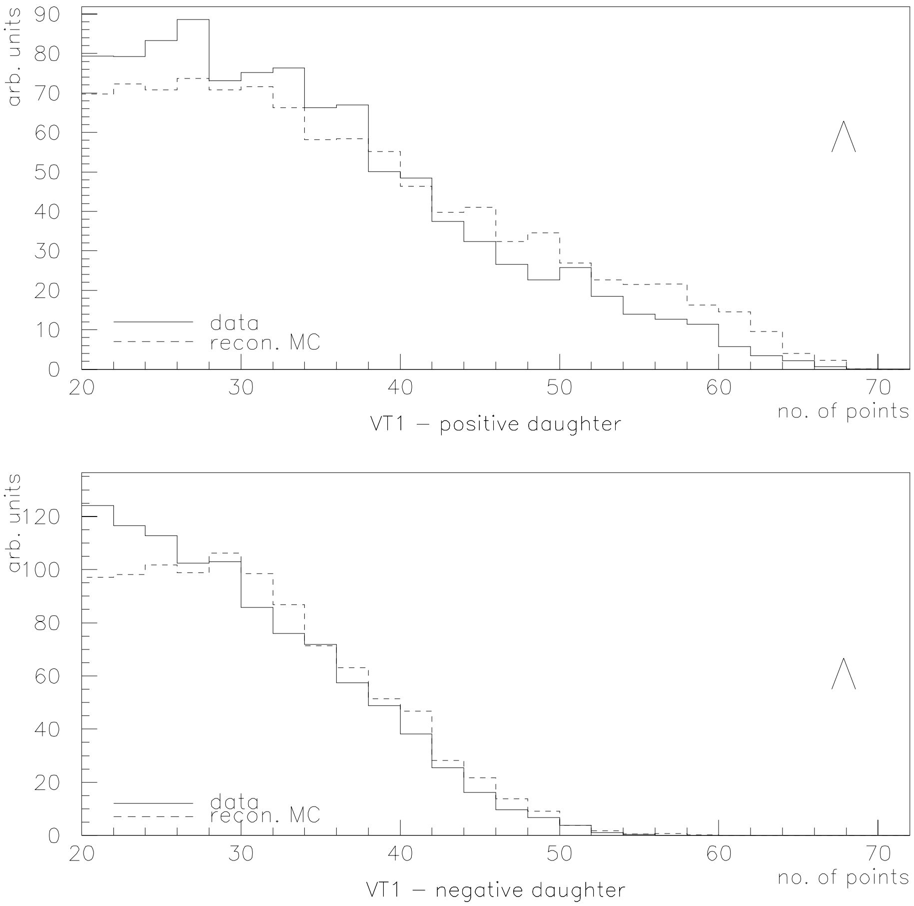

Figure 5.7: The number of points on Λ daughter tracks in VT1 for real and reconstructed MC data.

quire a reduction in the K^0_S found to 86%. There is therefore a likely underestimate in the rapidity distribution of approximately 15% of its current value. The VT2 point distributions are much flatter so the error is less and translates into a 6% underestimate in the rapidity points.

The same plots can be made for Λ and these are shown in figures 5.6 and 5.7. From these distributions it is estimated that the VT1 rapidity distribution should be 15% higher and the VT2 rapidity points increased by 5%. Although it has been possible to make these general estimates for the systematic error introduced by the cut on the number of points it is not possible to produce a correction that can be applied to the rapidity spectra. In general the systematic error will be rapidity dependent and there is an insufficient amount of data to produce such a correction.

5.2.2 Stability against cuts

The stability of the final results against geometric and kinematic cuts was investigated. The result, after corrections for acceptance and efficiency have been applied, ought not to depend on geometric cuts such as the position of the decay vertex nor on kinematic cuts, for example, a cut on Armenteros p_t for K^0_S. Even though the acceptance and efficiency corrections may differ between, say, a cut on the position of the decay vertex of x> 0 and x< 0, this should be reflected in the actual number reconstructed from the data. If the correction is accurate the same final result is obtained. The reason for choosing to look at the x- and y-dependence is that candidates with decay vertices with x< 0 (x> 0) correspond (approximately) to those leaving tracks in the left (right) half of the VTPCs. The two halves have different track densities due to the larger number of protons compared to anti-protons. The study addresses the question of whether the efficiency correction works in the same way in these different conditions. The y-dependence allows one to look at whether the drift of the clusters is well

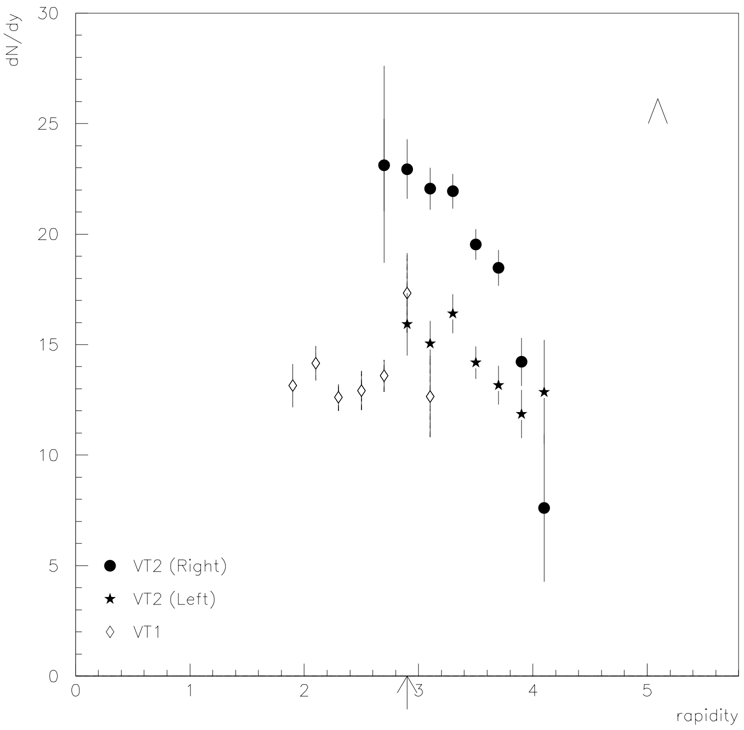

Figure 5.8: Rapidity distributions for Λ, from VT2 data divided into two samples according to whether the x co-ordinate of the decay vertex is greater than or less than zero. VT1 data is also shown for comparison.

simulated in the efficiency calculation since those decays with y< 0 have tracks with longer drift paths in the detector than those with y> 0.

For K_S^0 the differences between the rapidity distributions with x< 0 and x> 0 cuts for VT1 and VT2 lie within the statistical errors on the points except in the outside bins in VT2. The up-down comparison also shows quite good agreement with only a couple of VT1 points having a major discrepancy. In the case of Λ the situation is not as good, the most serious discrepancy is the left-right comparison in VT2 shown in figure 5.8. In some bins the points from the right hand side lie 30$\%$ lower. The right hand side (x<0) is the side with a higher track density which means that there could be dependence of the reliability of the efficiency calculation on track density effects. The distribution obtained from the right hand side of VT2 is rather similar to the full distribution obtained from VT1 which is also shown in figure 5.8. It seems that regions of similarly high track density produce a similar effect on the final rapidity distribution which is what might be expected for a systematic problem in calculating the efficiency correctly.

In summary the results from VT1 and VT2 for K_S^0 and $\overline{\Lambda}$ are in agreement once the estimated systematic error is taken into account. For Λ there is a rough agreement between VT1 and the higher track density side of VT2 which may be due to further systematic problems in calculating the efficiency correction. Alternatively the result from the side of VT2 with lower density may be wrong although this conclusion would be difficult to justify. It seems most likely that the more peaked Λ distribution from this side is the correct one. The systematic problem with the Λ rapidity spectra appears not to affect the spectra for K_S^0 and $\overline{\Lambda}$ to the same degree because their daughter tracks populate the TPCs differently, with less weight attached to the areas of high track density.

5.3 Comparisons

The results for rapidity, $\frac{dN}{d\mathbf{y}}$ at central rapidity and also the shapes and widths of the distributions, are compared to previous results. Comparisons are also made for the extracted inverse slopes.

5.3.1 Other analyses from Pb+Pb at 158 GeV

Preliminary analyses from a limited set NA49 data have been published previously in conference proceedings [18] [44] and theses [36] [31]. Additionally, the WA97 Collaboration have published data for Λ, $\overline{\Lambda}$ and K^0_S [48]. Turning first to the preliminary NA49 analyses, a problem with the efficiency calculation has been discovered which means that the high values of $\frac{dN}{dy}$ reported for Λ, $\overline{\Lambda}$ and K^0_S in these analyses are systematically too high. An analysis undertaken within NA49 which uses MTPC data with a modified target position [45] found a rather lower $\frac{dN}{dy}$ for K^0_S in broad agreement with the analysis presented here. The inverse slopes found previously also agree within the statistical errors (which were large), although since these had systematic problems no great significance ought to be attached to this agreement. The data for K^0_S can also be compared to that for charged kaons. Figure 5.9 shows the K^0_S data from the present analysis plotted with the data from the MTPC analysis. The dashed curve is the yield of K^+ and K^- averaged. This data comes from $\frac{dE}{dx}$ measurements [46] and has a systematic error of 20$\%$. All the data agree within these errors although clearly the agreement could be better. Rather different estimates of the $\frac{K}{\pi}$ ratio would result from using only K^0_S or only the charged kaons. Calculating the $\frac{K}{\pi}$ ratio as described in section 1.6.2 results in a value of 0.135 ± 0.025 which is similar to the same ratio measured in S-induced reactions.

The WA97 collaboration report slopes of 232±9 MeV for K^0_S in agreement with the result in this work. For Λ and $\overline{\Lambda}$ they report 289±8 MeV and 287±13 MeV respectively. Thus, the slope found for Λ in this analysis does not quite agree within the statistical errors. The values of T found fit the hypothesis of a transverse flow modifying the observed temperature in a mass-dependent way. The observed value of T is given by,

$$T = T_{fo} + m\beta^2 \tag{5.1}$$

where T_{fo} is the true freeze-out temperature, m is the mass of the particle and $\beta = \frac{v}{c}$, the flow velocity. A variety of hadronic species ranging from pions to deuterons have been found to have inverse slopes consistent with this scheme [49]. WA97 have also recently produced preliminary rapidity

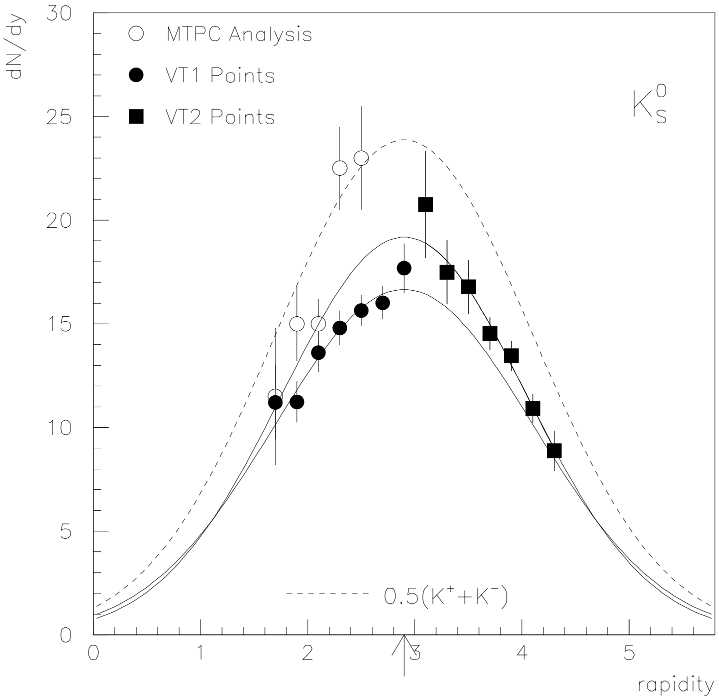

Figure 5.9: Rapidity distributions for K^0_S, from VT1, VT2 and MTPC analyses and for charged kaons, averaged.

distributions for Λ, $\overline{\Lambda}$ and K^0_S [47]. All of the distributions are almost flat in the small interval over which they are measured, generally within half a unit of rapidity either side of mid-rapidity. The $\frac{dN}{d\mathbf{y}}$ for K^0_S is 21, for Λ it is approximately 14 and for $\overline{\Lambda}$ it is around 2. Thus, the K^0_S distribution agrees with this data only at the mid-rapidity point. The VT1 Λ distribution is very similar to the WA97 one but the VT2 one lies above it. The $\overline{\Lambda}$ distribution peaks above the WA97 for both VT1 and VT2 and drops below it so that in fact the average yield in the rapidity window is about the same for both measurements. It must be noted that a flat rapidity distribution is rather unexpected, especially considering the K^0_S and comparing it to all of the measurements of kaon production from the NA49 experiment in figure

5.9.

The $\frac{\overline{\Lambda}}{\Lambda}$ ratio obtained is 0.148±0.008 if evaluated at mid-rapidity and 0.105±0.013 if the integrated yields are used, and the Gaussian distribution of Λ found in VT2 is assumed to be the correct one. This confirms the result of WA97 which finds a $\frac{\overline{\Lambda}}{\Lambda}$ ratio of 0.133±0.007 for a rapidity window centred on mid-rapidity one unit of rapidity wide. These results are therefore in very good agreement with each other.

5.3.2 Other energies and systems

A large set of data exist for S+S and S+Heavy-Nucleus collisions (S+Pb, S+W, S+Au) at 200 GeV per nucleon beam energy. It is less complicated to compare to the symmetric S+S collisions. Results for production of Λ, $\overline{\Lambda}$ and K_S^0 have been published by the NA35 and WA94 collaborations [50] [51]. Comparisons with lighter systems need to be scaled and a simple scaling by the number of participants going from S+S to Pb+Pb would imply multiplying by a factor 6.5. It should be noted that both the Pb and S data correspond to central triggers. The scaled yields of K_S^0, Λ and $\overline{\Lambda}$ are shown in table 5.3. The yields of K_S^0 and Λ agree within the errors quoted although there is of course a large systematic uncertainty attached to the extrapolation of the measured yield. The $\overline{\Lambda}$ yield in Pb+Pb falls well below that scaled up from S+S. It seems that a simple scaling from S+S collisions is not an appropriate description for all three species. The $\frac{\overline{\Lambda}}{\Lambda}$ ratio in S+S is 0.22±0.01 as found by WA94. NA35 found a higher ratio but this was not corrected for the effects of feeddown from cascade decays. It is interesting to note that the same ratio has been measured in the intermediate S+Heavy-Nucleus collisions . For S+W a value for the ratio of 0.196±0.011 was obtained by the WA85 collaboration [53], which is as one would expect between the values obtained in S+S and Pb+Pb collisions. However, for the similar S+Pb system a value of 0.117±0.011 was recorded by the NA36 ex-

Particle	Experimental	Scaled S+S	RQMD
K_S^0	54±5	68±11	77.3 ± 0.4
Λ	52±3	61.1±6.5	53.5 ± 0.4
$\overline{\Lambda}$	5.5±0.6	14.3±2.6	4.19 ± 0.10

Table 5.3: Yields of particles extrapolated to full phase space compared to scaled S+S and RQMD yields (see text). Experimental yields are those from the VT2 measurement.

periment [52]. The origin of the disagreement between these is probably due to the only partially overlapping y and p_t intervals in which the ratio is evaluated and to differences between the triggers for the two experiments. The NA36 value is from the region slightly further away from mid-rapidity which would tend to favour a lower value of the ratio when the Λ rapidity distribution is broader than that for $\overline{\Lambda}$. The end result is that the trend in the $\frac{\overline{\Lambda}}{\Lambda}$ ratio is not as clear as it might otherwise be.

5.3.3 Comparison to model predictions

One of the more successful microscopic models in use for simulating heavy-ion collisions is RQMD [54]. This model includes collective interactions in the pre-equilibrium quark matter and a hadronic resonance gas stage and thus goes beyond a plain superposition of nucleon-nucleon collisions but does not introduce a QGP phase. Data from the model were published [55] as part of a study of the effect of trying to extract thermal parameters from particle distributions measured in a limited region of phase space. The yield over the full phase space for each particle is shown in table 5.3. The Λ yield is the sum of Λ and Σ^0 from RQMD in order to correspond to the experimental situation where these two particles are indistinguishable and the same procedure was used for $\overline{\Lambda}$. The statistical errors on the results from RQMD are not those given in reference [55] as these were assigned so as to look like typical experimental errors. Instead, the statistical errors have been calculated using the yields and the fact that 400 RQMD events were simulated. The agreement for Λ is good and there is reasonable agreement for $\overline{\Lambda}$. However, the agreement between the experimental data and the model for Λ may not be significant, given the systematic uncertainty in extrapolating the measured Λ rapidity distribution. The experimental data for the K^0_S yield is 30$\%$ less than that predicted by the model. Overall though the model agrees better than a simple scaling from S+S collisions as there are no discrepancies on the order of a factor of two.

5.4 Future Directions

In order to get absolutely final corrected results from the NA49 data some improvements to the efficiency calculation are probably required for the VT1 data. Hopefully this would lead to a better agreement between the results derived from candidates found in the two detectors and give extra confidence to the results presented here. Such improvements ought to be possible by further tuning of the simulation. The measurement of singly strange particles is an important step in measuring multiply strange baryons as they form part of the decay chain of these particles and are also required in calculating ratios such as $\frac{\Lambda}{\Xi^-}$. This analysis is currently underway within the NA49 experiment and it will complement the findings of WA97 [48] by providing a larger acceptance measurement.

The NA49 experiment has also collected data from collisions over a range of impact parameters and analysis of these, once the simulation is stable, will allow comparisons to be made with the small collision systems previously studied in S-induced reactions. This dependence on impact parameter and hence the system size is also being studied by the NA57 experiment [56]. Later this year data will be taken using a 40 GeV beam which will allow part of the gap between AGS and existing CERN-SPS data to be filled. This year also sees the start-up of the RHIC at BNL. Experiments here will look at strange particle production in collisions with $\sqrt{s}$ an order of magnitude higher than at the SPS. This wide ranging program will allow the various dependencies on energy and system size to be identified.

5.5 Summary

Data for the production of Λ, $\overline{\Lambda}$ and K^0_S in Pb+Pb collisions have been presented. This includes rapidity distributions, which are consistent with a Gaussian shape for $\overline{\Lambda}$ and K^0_S, and p_t distributions which follow exponential distributions with inverse slopes of 237±5 MeV, 274±5 MeV and 279±10 MeV for K^0_S, Λ and $\overline{\Lambda}$ respectively. A reasonable overall agreement with several other measurements that are available is achieved. Results fit well to the trends in inverse slope, $\frac{K}{\pi}$ ratio and $\frac{\overline{\Lambda}}{\Lambda}$ ratio from other experimental data. This suggests that the dominant production mechanisms in S+S collisions also dominate in Pb+Pb collisions as there is no dramatic change in the strangeness enhancement factor in moving to this large system. If a QGP is formed then it is most probably formed in all collisions at SPS energies. The alternative may be that a QGP will dramatically manifest itself in collisions at the top RHIC energy. The effects seen at SPS energies could be collective effects of lesser magnitude due to the more complex nature of nuclear collisions where there is an overlap between independent nucleon-nucleon collisions. It will still be important to understand the nature of these effects in this case.

Appendix A

Kinematic Variables

It is usual to classify the particles produced in high-energy collisions using the kinematic variables rapidity, y and transverse momentum, p_t. Rapidity is a measure of the momentum in the longitudinal direction and it is defined as,

$$\mathrm{y} = \frac{1}{2} \ln \frac{E + p_L}{E - p_L} \tag{A.1}$$

where E is the energy and p_L is the momentum in the longitudinal direction. The transverse momentum is simply defined as,

$$p_t = \sqrt{\mathbf{p}^2 - p_z^2} \tag{A.2}$$

where p is the momentum vector and p_z is the component of momentum in the beam direction. The advantage of using these variables is that p_t is Lorentz invariant and y is only modified by an additive constant when a Lorentz transformation is performed so that comparisons between different frames, for example the centre of momentum and laboratory frames, are trivial and leave the shape of distributions unchanged. The rapidity variable has a dependence on mass, via the dependence on E. For p$\gg$m the rapidity is well approximated by the mass independent variable pseudo-rapidity, η, given by'

$$\eta = -\ln\tan\frac{\theta}{2} \tag{A.3}$$

where θ is the angle of the particle relative to the beam axis. In order to compare the p_t distributions among particles of different masses a further variable is defined, the transverse mass, m_t, given by,

$$m_t = \sqrt{p_t^2 + m_0^2} \tag{A.4}$$

where m_0 is the rest mass.

Bibliography

[1] A Chodos *et al.* 1974 *Phys. Rev.* **D 9** p 3471

[2] C DeTar 1995 *Quark Gluon Plasma* **2** ed. R C Hwa (World Scientific)

[3] M Stephanov, K Rajagopal & E Shuryak 1998 *Phys. Rev. Lett.* **81** p 4816

[4] J D Bjorken 1983 *Phys. Rev.* **D 27** p 140

[5] T Alber *et al.* 1995 *Phys .Rev. Lett.* **75** p 3814

[6] U Heinz 1999 *J. Phys. G: Nucl. Part. Phys.* **25** p 263

[7] F Becattini 1997 *J. Phys. G: Nucl. Part. Phys.* **23** p 1933
F Becattini & U Heinz 1997 *Z. Phys.* **C 76** p 269
F Becattini 1996 *Z. Phys.* **C 69** p 485

[8] J Letessier & J Rafelski 1999 *J. Phys. G: Nucl. Part. Phys.* **25** p 295
J Rafelski & J Letessier 1999 Hadrons from Pb-Pb colisions at 158A GeV *Pre-print* nucl-th / 9903018

[9] J Cleymans & K Redlich 1998 *Phys. Rev. Lett.* **81** p 5284

[10] J Cleymans 1998 *Proc. 3rd Int. Conf. on "Physics and Astrophysics of Quark-Gluon Plasma" (Jaipur, India, March 1997)* ed B Sinha *et al.* (New Delhi: Narosa) (*Pre-print* nucl-th / 9704046)

[11] R Albrecht *et al.* (WA80 Collaboration) 1996 *Phys. Rev. Lett.* **76** p 3506

[12] R Baur *et al.* (NA45 Collaboration) 1996 *Z. Phys.* **C 71** p 571

[13] J Rafelski & B Muller 1982 *Phys. Rev. Lett.* **48** p 1066
P Koch, B Muller & J Rafelski 1985 *Phys. Rep.* **142** p 167

[14] T Altherr & D Seibert 1994 *Phys. Rev.* **C 49** p 1684
N Bilic, J Cleymans, I Dadic & D Hislop 1995 *Phys. Rev.* **C 52** p 401

[15] H Sorge, M Berenguer, H Stocker & W Greiner 1992 *Phys. Lett.* **B 289** p 6

[16] K Werner & J Aichelin 1993 *Phys. Lett.* **B 308** p 372

[17] M Gazdzicki & D Röhrich 1996 *Z. Phys.* **C 71** p 55

[18] C Bormann *et al.* (NA49 Collaboration) 1997 *J. Phys. G: Nucl. Part. Phys.* **23** p 1817

[19] T Matsui & H Satz 1986 *Phys. Lett.* **B 178** p 416

[20] M C Abreu *et al.* (NA38 Collaboration) 1996 *Nucl. Phys.* **A 610** p 404

[21] M C Abreu *et al.* (NA50 Collaboration) 1997 *Phys. Lett.* **B 410** p 337

[22] M C Abreu *et al.* (NA50 Collaboration) 1999 *Phys. Lett.* **B 450** p 456

[23] D E Kahana & S H Kahana 1999 *Phys. Rev.* **C 59** p 1651

[24] H Appelshauser *et al.* (NA49 Collaboration) 1999 Event-by-event fluctuations of average transverse momentum in central Pb+Pb collisions at 158 GeV per nucleon, to be published in *Phys. Lett.* **B** (*Pre-print* hep-ex/9904014)

[25] G Roland (NA49 Collaboration) *et al.* 1998 *Nucl. Phys.* **A 638** p 91

[26] K Werner 1988 *Phys. Lett.* **B 208** p 520

[27] S Afanasiev *et al.* (NA49 Collaboration) 1999 The NA49 Large Acceptance Hadron Detector, to be published in *Nucl. Instr. and Meth.* **A** (*Preprint* CERN-EP / 99-001)

[28] C DeMarzo *et al.* 1983 *Nucl. Instr. and Meth.* **A 217** p 405

[29] A Kuhmichel (NA49 Collaboration) 1995 *Nucl. Instr. and Meth.* **A 360** p 52

[30] F Bergsma *TOSCA code,* CERN.

[31] T A Yates 1998 *PhD Thesis* University of Birmingham

[32] T Trainor *A Comparison of 1D×1D and 2D Cluster Finders for the NA49 Time Projection Chambers* University of Washington Nuclear Physics Laboratory Internal Note.

[33] K Kleinknecht 1986 *Detectors for particle radiation* Cambridge University Press

[34] H Grote 1987 *Rep. on Prog. in Phys.* **50** p 473

[35] D Evans 1992 *PhD Thesis* University of Birmingham

[36] H L Caines 1996 *PhD Thesis* University of Birmingham

[37] W H Press, B P Flannery, S A Teukolsky, W T Vetterling 1989 *Numerical Recipes (FORTRAN Version)* Cambridge University Press

[38] J Podolanski & R Armenteros 1954 *Phil. Mag.* **45** p 13

[39] Particle Data Group 1998 *Eur. Phys. J.* **C 3** p 1

[40] GEANT Detector Description and Simulation Tool 1993 *CERN Program Library Long Writeup*

[41] H Appelshauser *et al.* (NA49 Collaboration) 1998 *Phys. Lett.* **B 444** p 523

[42] R Hagedorn 1983 *Riv, Nuovo Cimento* **6** p 1

[43] H Appelshauser *et al.* (NA49 Collaboration) 1999 *Phys. Rev. Lett.* **82** p 2471

[44] P Jones *et al.* (NA49 Collaboration) 1996 *Nucl. Phys.* **A 610** p 188

[45] S Margetis (NA49 Collaboration) 1996 *Heavy Ion Physics* **4** p 63

[46] F Sikler (NA49 Collaboration) 1999 Hadron Production in nuclear collisions from NA49 experiment at 158 GeV / c.A, to be published in *Nucl. Phys.* **A**

[47] F Antinori (WA97 Collaboration) 1999 Production of Strange and Multistrange Hadrons in Nucleus-Nucleus Collisions at the SPS, to be published in *Nucl. Phys.* **A**

[48] E Andersen *et al.* (WA97 Collaboration) 1999 *Phys. Lett.* **B 449** p 401

[49] I Bearden *et al.* (NA44 Collaboration) 1997 *Phys. Rev. Lett.* **78** p 2080
N Xu *et al.* (NA44 Collaboration) 1996 *Nucl. Phys.* **A 610** p 175

[50] T Alber *et al.* (NA35 Collaboration) 1994 *Z. Phys.* **C 64** P 195

[51] S Abatzis *et al.* (WA94 Collaboration) 1995 *Phys. Lett.* **B 354** p 178

[52] E Andersen *et al.* (NA36 Collaboration) 1994 *Phys. Lett.* **B 327** p 433

[53] S Abatzis *et al.* (WA85 Collaboration) 1995 *Phys. Lett.* **B 359** p 382

[54] H Sorge 1995 *Phys. Rev.* **C 52** p 3291

[55] J Sollfrank, U Heinz, H Sorge & N Xu *Phys. Rev.* **C 59** p 1637

[56] V Manzari *et al.* (NA57 Collaboration) 1999 *J. Phys. G: Nucl. Part. Phys* **25** p 473